STUDY OF THE SURFACE MODIFIED $Co_{0.5}Zn_{0.5}Fe_2O_4$ NANOENSEMBELS FOR BIOMEDICAL APPLICATION

M.Phil. Thesis

BY

SUMAN HALDER

DEPARTMENT OF PHYSICS
KHULNA UNIVERSITY OF ENGINEERING & TECHNOLOGY
KHULNA - 9203, BANGLADESH

OCTOBER- 2017

STUDY OF THE SURFACE MODIFIED $Co_{0.5}Zn_{0.5}Fe_2O_4$ NANOENSEMBELS FOR BIOMEDICAL APPLICATION

BY

SUMAN HALDER
ROLL NO: 1555505
SESSION: JANUARY-2015

A THESIS SUBMITED TO THE DEPARTMENT OF PHYSICS,
KHULNA UNIVERSITY OF ENGINEERING & TECHNOLOGY,
KHULNA - 9203 IN PARTIAL FULFILMENT OF THE
REQUIRMENT FOR THE DEGREE OF MASTER OF PHELOSOPHY

DEPARTMENT OF PHYSICS
KHULNA UNIVERSITY OF ENGINEERING & TECHNOLOGY
KHULNA - 9203, BANGLADESH

OCTOBER- 2017

TO

MY ALL TEACHERS

DECLARATION

This is to certify that the thesis work entitled as **“Study of the Surface Modified $Co_{0.5}Zn_{0.5}Fe_2O_4$ Nanoensebbles for Biomedical Application”** has been carried out in partial fulfillment of the requirement for M. Phil. degree in the Department of Physics, Khulna University of Engineering & Technology, Khulna-9203, Bangladesh. The above research work or any part of this work has not been submitted to anywhere for the award of any degree or diploma. No other person’s work has been used without due acknowledgement.

1. **Supervisor** **Candidate**

....

Prof. Dr. Shibendra Shekher Sikder Suman Halder

2. **Joint-supervisor**

....

(Dr. Sheikh Manjura Hoque)

Acknowledgements

I esteem it a great privilege to express my deep sense of gratitude and indebtedness to my supervisor Professor Dr. Shibendra Shekher Sikder, Head, Department of Physics, Khulna University of Engineering & Technology, Khulna and my joint supervisor Dr. Shakhe Manjura Hoque, Head and Chief Scientific Officer, Materials Science Division, Atomic Energy Centre, Dhaka (AECD) for their impeccable guidance and great assiduity in my thesis work. This thesis wouldn't have been completed in time without their help.

My thanks due to Dr. Dilip Kumar Saha, Chairman, Atomic Energy Centre, Dhaka, for his kind permission to use the laboratory of Materials Science Division, AECD. I wish to thanks all the scientist of Materials Science Division, especially to Dr. Nazrul Islam Khan, Mr. Fazul Kamal, Dr. Harinarayan Das for their support and scientific discussion to do this research work.

I am very much thankful to Mrs. Samia Islam Liba and Mis. Arijun Nahar Irin, Scientific Officer, Materials Science Division, AECD, for their active support during the experiment.

I would like to express my gratitude to Professor Dr. Md. Mahbub Alam, Department of Physics, Khulna University of Engineering & Technology, for his co-operation and inspiration during this work. My thanks are also for Dr. Abdullah Ileas Akter, Dr, Joly Sultana, Professor, Md. Kamrul Hasan Reza, Associate Professor, Md. Asaduzzaman, Mr. Sujit Kumar Shil, Mr. Alamgir Hossain, Assistant Professor and Mr. Sumon Dev Nath, Mr. Probal Roy & Mr. Saifullah, Lecturer, KUET, for their support during this work.

I am deeply grateful to Dr. Abdul Gafur, Director, DMTBI, BCSIR, Dhaka for his generous help during XRD measurement and analysis.

I would like to extend my gratitude towards Mr. Khairul Islam and Mrs. Shamima Akter, Ph.D. student, Materials Science Division, AECD for their contribution to this work.

My special thanks to all the staff members of Materials Science Division, AECD, particularly Mrs. Alhamra Parveen, Mrs. Anjuman Ara Begum, Mr. Kamrul Islam, Mr. Anowar Hossain, Mr. Nurul Islam, Mrs. Nazmunnahar Begum, Mrs. Zarna

Begum and Mr. Kaiyoum for their help during the preparation of the sample and experimental measurements.

I also wish to thank to authority of Khulna University of Engineering & Technology for providing me with the necessary permission and financial assistance for conducting their thesis work.

The present paradise of my work has essentially been built on the support and encouragement of my family members, acknowledging them beyond the scope of my words.

Suman Halder

ABSTRACT

Single domain magnetic nanomaterials with appropriate size and properties are interest for verity of biomedical and electrical applications such as magnetic hyperthermia, drug delivery, magnetic resonance imaging contrast enhancement, high-frequency electronics and high-density magnetic storage device. The superparamagnetic nanoparticles have their unique property, which can be manipulated and heated by an external ac magnetic field in order to destroy the cancer cells. In order to address this induction heating of MNPs (hyperthermia effect), we have prepared and characterized $Co_{0.5}Zn_{0.5}Fe_2O_4$ nano ensembles throughout this research work.

This research work deals with the synthesis of $Co_{0.5}Zn_{0.5}Fe_2O_4$ magnetic nanoparticles have been prepared using chemical co-precipitation methods. In order to investigate the annealing effects on their various physical properties, the prepared sample have been annealed at 200^0C, 400^0C, 600^0C, 800^0C and 1000^0C and then compared with the as-prepared sample. The XRD pattern of the as-dried and annealed samples exhibit single phase spinel structure with clear diffraction pattern. Enhancement in crystallite size from 7nn to 25nm is observed with the increase in annealing temperature from 200^0C to 1000^0C respectively. VSM study reviled that as-prepared and annealed samples showed superparamegnetic behavior, which was further confirmed by the Mossbauer Spectroscopy. The saturation magnetization values of $Co_{0.5}Zn_{0.5}Fe_2O_4$ increased with the increase in annealing temperature, which confirmed that samples possess size and morphology dependent magnetic properties. Mossbauer spectra observed central doublet nature up to annealed sample 600^0C and there is no hyperfine magnetic field is confirmed superparamagnetic behavior. The hydrodynamic diameter and the polydispersity index (PDI) were analyzed by DLS system at 37^0C and found to be between 173 nm and 231nm where PI is overall less than 0.3. For the hyperthermia study the result of induction heating measurements showed that the temperature raised by the 6mg/ml and 4mg/ml were 46^0C and 43^0C respectively. It has been seen that the rise in temperature due to the induction heating depends on the particle size and concentration of the nanoparticle. Finally, when

coated with chitosan, these nanoparticle show a great ability to response to external field also suitability for biomedical application especially on hyperthermia therapy.

CONTENTS

CHAPTER-I

INTRODUCTION

CHAPTER-II

FORMALISM OF NANOMAGNETISM

CHAPTER-III

MATERIALS PROCESSING AND THEORY OF EXPERIMENTATION

CHAPTER-IV

RESULTS AND DISCUSSION

CHAPTER-V

CONCLUSIONS

List of Figures

List of Tables Page No

List of Symbols

XRD = X-Ray Diffraction
VSM = Vibrating Sample Magnetometer
T_m = Melting temperature
K_1 = Anisotropy constant
H_c = Coercive force
μ = Permeability
μ_m = Maximum permeability
μ_i = Initial permeability
μ' = Real part of the complex permeability
μ'' = imaginary part of the complex permeability
D_g = Grain size
B = Magnetic induction
H = Magnetic field
a_0 = Lattice parameter
Tan δ = loss factor or loss tangent.
M_s = Saturation magnetization
T_c = Curie temperature
λ = Wave length of the X-ray
[hkl] = Index of the peak
I = X-ray beam of intensity
SPM = Superparamagnetic
Θ = Weiss constant
M = Magnetization
MNPs = Magnetic Nanoparticles
DLS = Dynamic Light Scattering

INTRODUCTION

1.1 Nanoscience & Nanotechnology

Nanoscience is one of the most exciting topics in the history of scientific research. The history of nanotechnology began from the prehistoric period when human beings used naturally occurred nanoscale materials for their cave painting, but the terms nanotechnology was first introduced by the ancient Egyptians more than 3000 years ago, though they had no idea about the underlying principle of nanoscience. They had only idea to make a specific blend of wet sand which could worked truly well to lubricate the ground where they pulled tremendous pieces of limestone to fabricate the pyramids. After thirty years, nanoscience and nanotechnology has, to a certain extent, come full circles.

Nanoscience is the study of the properties of matter at the nanoscale, in particular, it focused on the unique, size-dependent properties of the solid-state materials. The nanoscience is a subject which is cross disciplinary, meaning scientists from all discipline including chemistry, physics, biology, medicine, computing, materials science and engineering are studying it and using it to better understand our world. New method of synthesis and new approach of characterization are needed to make and explore nanomaterials [1.1]. The role of nanotechnology was given its due recognized its potential for a plethora of applications. At the beginning of the twentieth century when scientists felt that atoms were mere abstract entities used for the purpose of calculations, it was Albert Einstein who explained the “jittery dance of microscopic particles- Brownian motion” and provided the view point that the mathematical description of Brownian motion is the evidence for the true existence of atom [1.2]

On the other hands, nanotechnology is the applications of nanoscience. To elaborate, nanotechnology is the design, production and application of structures, devices and systems at nanoscale. In other words, nanotechnology is the ability to manipulate a single nanoscale object. It is the presence of the word “single” that makes all the difference. The thought and concept underlying beforehand nanotechnology started with a talk entitled “There’s Plenty of Room at the Bottom” by physicist Richard Feynman at an American

Physical Society meeting at the California Institute of Technology on December 29, 1959, long before the term nanotechnology was used. Feynman mentioned about miniaturization by evaporation and rearrangement of atoms manipulation of systems for data storage down to the scale of a single atom. After long time of Feynman's lecture, Professor Norio Taniguchi introduced the term nanotechnology in his explorations of ultra-precision machining. He also expressed the necessary for better microscopes systems. The first recognized article on molecular nanotechnology published and with the advent of technique such as Scanning Tunneling Microscope (STM) in 1981 and Atomic Force Microscope (AFM), visualization of nano world become reality, which gave a pace to development of modern nanotechnology.

It is most important question that how small is nanoscale small? There is no universal definition so far for nanoregime. The word "nanometer" defines a length unit of $1nm= 10^{-9}m=10A^0$. To have a clear idea of how large or tiny 1nm is, take an example of individual atom that are up to a few Angstroms, or up to a few 10th of nanometer, in diameter. Biomedical cells, such as the red blood cells, have diameter in the range up to 1000nm. A length of 1nm can accommodate 10 hydrogen atoms laid side by side, a strand of DNA is 2.5 nm in diameter, while a red blood cell is about 1,000 nm wide. On a comparative scale, if a marble were a nanometer, then one meter would be the size of the Earth. So nano is super, super tiny. In general, material systems with possible size 1-100nm range by virtue of possessing large surface to volume ratio come within the periphery of nanomaterial or nanosystems or nanometric system or nanostructural systems.

The advancement of technology are interested things as they provides much comfort for human being with their aura of risk. Decades of research and development in nanoscience and nanotechnology have provided both expected and unexpected benefits for mankind. Nanotechnology is helping to improve products across a range of areas, including food safety, medicine and health care, energy, transportation, communications, environmental protection and manufacturing. It is being used in the automotive, electronics and computing industries, and in household products, textiles, cosmetics—the list goes on.

Nanotechnology also creates the so-called mechanical surgeons that could treated to trouble spots inside the body. Biocompatible nanoparticles can be loaded with an optical imaging agent and drug using a polymer. The entire entity migrates to the trouble spot in human body and release of the drug allows real time monitoring of the drug delivery by optical imaging [1.3]

Magnetic nanoparticle (MNPs) have gained a lot of attention in biomedical application due to their biocompatibility, easy surface modification, large magnetic anisotropy, constant and saturation magnetization. Therapeutic agent are attached to or encapsulate within MNPs. MNPs tend to agglomerated because of their large surface energy and strong magnetic interactions. In recent years, there has been intense research interest in the fabrications of core-shell particles with suitable properties for various applications in materials science [1.4]. The properties of the core-shell can be significantly changed by the shell surrounding. The Fe_3O_4 nanoparticles can be synthesized by co-precipitation route [1.5-1.7]. As MNPs are used in wide variety of biomedical applications, their toxicity should be taken into account. The toxicity depends on the various factors such as size of the particle, chemical composition and coated materials [1.8-1.9]. To remove the toxicity and make biocompatible a biological or molecular coating or layer should be attached to the MNPs. The examples of the biocompatible materials may be includes antibodies, biopolymer like Collagen, chitosan or monolayer of small molecules. So more research is needed to find more non-toxic efficient agents, which should not be deleterious to our benign tissues. As a promising candidate for biomedical applications we would study thoroughly the superparamegnetic nanoferrite with biocompatible coating of chitosan for hyperthermia protocol of cancer therapy.

1.2 Fundamental Concepts of Magnetic nanomaterials

Nano materials have their ability to travels to trouble cell inside the body and have potential applications in drug delivery, MRI and diagnostic. MNPs are used for in vitro gene transformations in which DNA is attached to it and the magnetic increases particle internalization and gene expression. MNPs were applied in different research field sensor development, storage device etc. [1.10]

In 1930 William Fuller Brown and Louis Neel first described the fundamental concepts of single domain particles and it accelerated the research of magnetic nanoparticles. Nanomaterials encompass all nanoscale materials or materials that contain at least one nanoscale structure, either on their surfaces or internally. MNPs can be inorganic, organic or biological. Nanomaterials such as nanoplates, nanoparticles, nanowires and nanotubes can be engineered in labs. Nanomaterials can also occur in nature—naturally occurring nanoparticles include smoke, sea spray and volcanic ash, as well as minerals, soils, salt particles and biogenic particles. Nanoparticles, nanowires, nanotubes and nanoplates are all types of nanomaterials, distinguished by their individual shapes and dimensions. What these materials have in common is that they have one or more dimension at the nanoscale.

- Zero-dimensional nanomaterials: Zero-D nano system are nanocluster, nanoparticles, annocubes. In terms of physics a Zero-D nanomaterials are known as "quantum dots" where the quantum confinement occurs along all 3-D.
- One-dimensional nanomaterials: 1-D were nanotubes, nanorod and nanofibers, here the radius is in the nanoscle regime.
- Two-dimensional nanomaterials:In 2-D nanoforms one of the 3-D is within the length scale 1-100nm. This leads to the quantum confinement along one of the dimension. 2-D nanoparticles include nanofilms, nanolayers and nanocoatings.
- Three-dimensional nanomaterials: Bulk nanomaterials are materials that are not confined to the nanoscale in any dimension. These materials are thus characterized by having three arbitrarily dimensions above 100 nm. With respect to the presence of features at the nanoscale, 3-D nanomaterials can contain dispersions of nanoparticles, bundles of nanowires, and nanotubes as well as multinanolayers.

Currently several research group are engaged in investigations of metal oxide nanoparticle because of their technological applications in magnetic and microwave devices, magnetic recording media, etc. Several types of nanomaterials such as metal (Fe, Co, Ni), metallic alloys (Fe-Co), and metallic oxides ($MgFe_2O_4$, Cu Fe_2O_4, and Zn Fe_2O_4) are under recent research activity, while metal nanoparticles have stability problems in atmospheric condition. However, metal oxides are stable under ambient condition. For example, the well-known iron oxide Ferro fluid becomes undesirable because of their iron atoms are poorly distinguishable from those of hemoglobin [1.11]. A conceivable solution is to use mixed-ferrites using highly magnetic materials such as Cobalt and Nickel. Those ferrites have attracted special attention because of their easy synthesis, physical and chemical stability and suitable magnetic properties.

Though this mixed ferrites have large magnetic anisotropy and saturation magnetization but they are toxic; hence they are of little interest [1.12]. The substitution of Co^{+2}/ Ni^{+2} ions by Zn^{+2} allows variations of properties that can be tuned to specific application in addition to it the toxicity could be removed [1.13].

1.3 Prospect of magnetic nanomaterial in biomedical applications

The magnetic nanoparticles have a wide range of applications like industry, Jet painting, magnetic data storage devices, as an electrode in batteries, sewage treatment plant and biomedical applications. MNPs have gained a lot of attention in biomedical application for their biocompatibility and their surface can be easily modified. In addition, magnetic anisotropy constant and saturation magnetization of MNPs are made them easy access to biomedical applications. There are a huge number of areas in biomedical application to which MNPs can be applied include magnetic separation of labelled cells and other biological entities; drug, gene and radionuclide delivery; artificial hyperthermia treatment of tumor and cancer cell and contrast enhancement in magnetic resonance imaging (MRI). In one of the clinical trials of MNPs have already been tested [1.14]. Here, doxorubicin linked to magnetic carriers was delivered using concurrent MRI, and the particles were targeted to the tumor site. The result showed that the particles/drug complex was well focused to the tumor sites with between 64% and 91% of the tumor volume affected by the drug. The short description of various applications of MNPs are given below.

1.3.1 Magnetic Separation of Labelled Cell

Magnetic separation is in essence separating specific biological entities from their native environment and studying or manipulating in a better controlled environment. Magnetic separation using biocompatible nanoparticles is one way to achieve this. It can be achieved in two step, involving (a) the tagging or labelling of the desired biological entity with magnetic material, and (b) the separating out of these tagged entities via a fluid-based magnetic separation device. The separator device can be deigned several way, from quite simple to rather complex to separate the magnetically tagged material from its surrounding [1.15]. Magnetic separation has been successfully applied to many aspects of biomedical and biological research and has proven to be a highly sensitive technique for the selection of rare tumour cells from blood, and is especially well suited to the separation of low numbers of target cells [1.16], which led to the enhanced detection of malarial parasites in blood samples either by utilizing the magnetic properties of the parasite [1.17] or through labelling the red blood cells with an immunospecific magnetic fluid [1.18]. It has been used as a pre-processing technology for polymerase chain reactions, through which the DNA of a sample is amplified and identified [1.119]. Cell counting techniques have also been developed. One method estimates the location and number of cells tagged by measuring the magnetic moment of the microsphere tags [1.20], while another uses a giant magnetoresistive sensor to measure the location of microspheres attached to a surface layered with a bound analyte [1.21]. In another application, magnetic separation has been used in combined with optical sensing to perform the test regarding the presence or concentration of certain substances. The magnetic separation technique guarantees an efficient tagging and high enough concentration of substance, while optical sensing can then use a fluorescent tag to detect the substance.

1.3.2 Targeted Drug delivery

Drug delivery by using magnetic nanoparticles is another advancement of nanotechnology. Magnetic drug delivery system works on the delivery of magnetic nanoparticles loaded with drug to the infected area of the body under the influence of the external magnetic field. However, development of the delivery system mandates that the nanoparticles behave magnetic only under the influence of external magnetic field and are rendered inactive once the external magnetic fields is removed. Furthermore, such magnetic properties are usually acquired by very small nanoparticles within the size range of less than 10nm, due to the presence of single domain state.

The therapeutic drugs are administered intravenously leading to general systemic distribution, resulting in deleterious side-effects as the drug attacks normal, healthy cells in addition to the target tumor cells. For example, the side effects of anti-inflammatory drugs on patients who have chronic arthritis can lead to the discontinuation of their use. The drug can be attached to the magnetic particle and then a magnetic force can change the path of the tagged particles. Once at the correct place, the drug can be released from its carrier either via enzy matic activity or physiological changes (pH, osmolality, temperature) [1.22]. As for the tagging process, coating is required. These coatings can be of organic or inorganic origin. During their journey the coating protects the magnetic nanoparticles or microspheres and once at their target, it can serve as an attachment point to the targeted entity. In general, there are two types of structural configurations: (i) a magnetic particle core (usually magnetite, Fe_2O_4, or maghemite, γ- Fe_2O_3) coated with a biocompatible polymer or (ii) a porous biocompatible polymer in which magnetic nanoparticles are precipitated inside the pores [1.23]. The advantages of targeted drug delivery seem numerous: Most drugs are non-specific, i.e. they get distributed over the whole body as soon as they get administered intravenously. Targeted delivery can ensure that only specific areas get influenced by the (otherwise harmful) drugs and as little as possible of the drug needs to be administered. This method seems especially applicable, when the drug is very damaging to healthy tissue. Fields of application are Chemotherapy, radionuclide therapy and gene therapy. While having proven to be very successful in animal tests, there were not many studies with humans as test subjects. And while being very promising for the future, a couple of problems should not be neglected [1.24-1.25]:

- Embolization of blood vessels due to too high concentration of the magnetic carriers.
- Larger distances to cover in humans compared with animals.
- As soon as the drug is released, it cannot be influenced any longer by magnetic field gradients.
- The magnetic carriers itself may have unwanted side effects.

1.3.3 Magnetic Resonance Imaging

An important field of potential application of magnetic nanoparticles is magnetic resonance imaging (MRI) contrast enhancement [1.26]. In the recent years, ferrite nanoparticles have emerged as an MRI contrast agents among the several areas in the field of biomedical applications. Contrast agents within a physiological system function through a mechanism called relaxation. Then a relaxation phenomenon taken place where this protons to their original state from the perturbed state. Two independent processes, called longitudinal relaxation (T_1-recovery) and a transverse relaxation (T_2-decay), can be monitored to generate as MRI image. In recent research on the use of ferrite nanoparticles in T_2 contrast agent has shown a great potential application on MRI [1.27-1.28]. Nano particles attached to the cell or cell component can shorten both the transverse and the longitudinal relaxation time. Due to the fact that different tissues take up the nanoparticles differently an enhancement between the different tissues is achieved and the contrast between them are higher.

Hydrogen protons of water molecules undergo relaxation after the excitation of protons with an external magnetic field. Under the application of high DC magnetic field, spins of the proton magnetic moments precess about the direction of the magnetic field at Larmor frequency. When an AC exciting field of Larmor frequency is applied on the precessing moment of the proton, the moments are perturbed. The moments return to their thermodynamic equilibrium through couple of relaxation processes. These are spin–lattice, T_1 relaxation in which energy is transferred from the spin to its surrounding environment, i.e., spin-lattice T_1 and spin–spin, T_2 relaxation in which relaxation is achieved through de-phasing of magnetic moment. In this process, contrast agents themselves do not generate any signals, yet they contribute to create local field inhomogeneity, which arise from the susceptibility difference of different elements in the proximity of the particles within a voxel because of the difference in the uptake of different elements in the body. This shortens T_2 relaxation time because of the creation of greater local field homogeneity in the presence of the contrast agent and thus provides an opportunity to acquire T_2 weighted image. Cancer treatment has received greater benefits from MRI technique and MNPs have been extensively developed to improve the detection, diagnosis and therapeutic management of solid tumors. Next generation of active targeting based on nanoparticles has a potential to offer significant improved tumor detection and localization by exploiting the unique molecular signatures of these diseases [1.29]. Other applications of MNPs enhanced MRI are in the field of cardiovascular medicine including myocardial injury, atherosclerosis and other vascular diseases [1.30].

1.3.4 Nano Magnetism in Therapeutic Hyperthermia

One of the most important application of magnetic nanoparticles is hyperthermia which the idea that a localized rise in temperature can be used to destroy the tumor and cancer cell without harming the benignant tissue under the exposure of rf current which excites superparamagnetic ferrite nanoparticles absorbed in the diseased cells by Brownian and Neel relaxation [1.31]. Hyperthermia raise the temperature of a region of the body affected by tumor or other growths. The reason is based on a direct cell-killing effect at a temperature about 42^0C. Hyperthermia can be used in the following two ways:

(i) Very high temperature can be used to destroy a small area of cell such as a tumor. This is often called local hyperthermia or thermal ablation.
(ii) The temperature of the part of the body can be raised to a higher than normal level. It is not high enough to kill the cells directly but this can allow other types of cancer treatment like radiation therapy, immunotherapy or chemotherapy to work better. This is known as regional hyperthermia or whole body hyperthermia.

The magnetic particles first have to be brought to the target area, where they can be caused to heat up by an AC magnetic field of sufficient strength and frequency. The heat should exceed the threshold of 42^0C and last for about 30 minutes in order to properly destroy the tumor. During magnetic hyperthermia (MH) therapy, MNPs dissipate applied magnetics energy into heat mainly via relaxation loss process [1.32]. In addition to the field parameters, specific loss power (SLP) heat generated per unit mass of MNPs dissipation are strongly depends on the particle size, size distribution, anisotropy constant, saturation magnetization and surface modification [1.27, 1.33]. This kind of treatment with rats were successful and quit promising but so far it could not be applied to human fully and commercially due to our larger size and lack of efficient agent. So more research are needed to find more non-toxic efficient agent which would not be harmful to our benignant tissue.

Current research trends in nanotechnology are reviewed here with special emphasis on biomedical applications. One thing that almost all of these applications have in common, however, is that they are not yet market-based technologies. The exceptions are magnetic separation via cell and protein labelling, which is found in most biomedical and biochemistry laboratories today, and MRI contrast enhancement using encapsulated SPM nanoparticles, which is available in most hospital scanning facilities. Drug delivery via coating of nanoparticles is currently undergoing preliminary human trials, after successful tests in animals, with promising results, but it will be some time before it will be clinically available; and hyperthermia treatment of tumours is not yet accessible in humans, despite having been proven to be effective in animals. This highlights the fact that there is a significant step between a proven hypothetical process that has been tested under controlled laboratory conditions, and a close-to-market technology which can cope with the added complexity of in-service use. This is especially so if the goal is to transfer a procedure that has largely been the subject of in vitro or animalin vivo testing into a humanin vivotherapy. Research in the field of nanomedicine is quite promising and is expected to revolutionise the disease diagnosis and therapy in the near future.

1.4 Reason for selecting $Co_{0.5}Zn_{0.5}Fe_2O_4$

Nanoparticles are small size and have physical resemblance to molecules as proteins. Hence, they are used in the broad range of applications. The biocompatibility and toxicity less nanoparticle is needed for the safe use inside the body. Some of the recent works refers to the understanding of the biocompatibility and toxicity of nanoparticles [1.34]. For biomedical uses, the application of particles that present superparamagnetic behavior at room temperature is preferred. Furthermore, applications in therapy and biology and medical diagnosis require the magnetic particles to be stable in water at PH 7 and in a physiological environment. Among magnetic materials, magnetic ceramics have received special attention due to chemical stability, as well as high electrical resistivity. One of the most important magnetic ceramics is spinel. The most important spinels from the magnetic point of view are oxides 2, 3 or MFe_2O_4 [1.35-1.36]. Among spinel ferrites, $CoFe_2O_4$ has considerably been appealing because of its large magnetic multi-axial anisotropy, moderate saturation magnetization, high Curie temperature and remarkable chemical stability [1.37-1.39]. Cobalt ferrites nanoparticles are suitable for the isolation and purification of genomic DNA, the separation of PCR (polymerase chain reaction) ready DNA [1.40-1.41] and especially in hyperthermia treatment [1.42-1.43]. The introduction of the third metal ion modifies the distribution of ions in the spinel structure. Variation in the concentration of the third metal ion like Zn in Co ferrite can easily alter the distribution of Fe3þ ion. Zinc-substituted mixed ferrites (Co–Zn) are chosen due to their high sensitivity of magnetization to temperature for some applications like self-controlled hyperthermia [1.44-1.45]. For *in vivo* biomedical applications, magnetic nanoparticles must be made of a non-toxic and non-immunogenic material, with particle sizes small enough to remain in the circulation after injection and to pass through the capillary systems of organs and tissues, avoiding vessel embolism. They must also have a high magnetization so that their movement in the blood can be controlled with a magnetic field and so that they can be immobilized close to the targeted pathologic tissue. As MNPs have been used for wide variety of biomedical application, their toxicity should be investigated in detail. As a promising candidate for biomedical applications we would study thoroughly the superparamagnetic nanoferrite with biocompatible coating of chitosan for hyperthermia protocol of cancer and its toxic effects on human body. Highly magnetic materials such as cobalt and nickel are toxic so if Co is replace by Zn, toxicity should be removed.

1.5 Review of Earlier Research Work

The biomedical applications imposes some special requirements. For examples, the well-known iron oxide Fero-fluid becomes undesirable because of their iron atom are poorly distinguishable from those of hemoglobin [1.46]. A conceivable solution is to use mixed ferrite using highly magnetic materials such as Cobalt and Nickel. Those ferrite have attract a special attention because of their easy synthesis and suitable magnetic properties. Though, this mixed ferrite have laser magnetic anisotropy and saturation magnetization but they are toxic. Hence, they are of little interest [1.47]. The substitution of Co^{2+}/Ni^{2+} ions by Zn^{2+} allows variation of properties that can be tuned to specific application in addition to it the toxicity could be removed [1.48]

Nouri *et al.* [1.49] synthesized $Co_{0.6}Zn_{0.4}Fe_2O_4$ by using chemical co-precipitation method and coated by chitosan. The crystal size of the nanoparticle was calculated from XRD patterns from (311) plane using Debye-Scherrer's equation and found to be 17.8 nm and the size of core shell of the nanoparticles was confirmed in the range 15-25nm by TEM micrographs. The formation of spinal structure was confirmed by FTIR peaks related to tetrahedral and octahedral vibrations. By VSM analysis they showed saturation magnetization of about 53.24 emu/g and residual field of about 14.76 Oe for the nanoparticles which is the best superparamegnetic behavior.

Abdulaziz *et al.* [1.50] prepared $Co_{(1-x)}Zn_xFe_2O_4$ (x = 0-0.5) nanocrystalline powder by co-precipitation method. The powder sample was characterized by VSM and XRD. The cubic spinal structure of the nanopowder was confirmed by XRD analysis. The VSM study revealed that with the increase of Zn content saturation magnetization increase. The coercive field of the samples varies linearly from 1137.77 Oe to 33.31 Oe as the Co^{2+} content decrease form the B-site. It has been seen that x = 0.5 in $Co_{(1-x)}Zn_xFe_2O_4$ is an optimum composition with superior magnetostrictive properties for many applications.

Vinuthana *et al.* [1.51] used citrate precursor method to synthesis $Co_{(1-x)}Zn_xFe_2O_4$ and characterized by using XRD, TGA, IR, XPS. The study presented that the effect of Zn concentration on the structural properties and it was found that with the concentration of Zn crystalline size and lattice constant are increased. They reported that unite cell parameter increase linearly with the increase of concentration of Zn. Fourier transformed infrared (FT-IR) spectra of Zn^{+2} ions substituted in Co-Zn spinal ferrite nano-particles have been analyzed in frequency range of 4000 - 400cm^{-1} and found two absorption bond in the range of 600 - 400cm^{-1}.

Daryoush *et al.* [1.52] investigated cytotoxicity effect of nanoparticle for human health. For this purpose they characterized Co-Zn Ferrite nanoparticle using TEM, FTIR and atomic absorption spectrometer (AAS) in following, cytotoxicity was investigated on human prostate cancer cell lines. The results showed that the average size of bare and coated nanoparticles was about 16 and 40 nm. The FTIR spectra results showed the presence of DMSA cover on the surface of nanoparticles. Furthermore, in vitro MTT assay CZF-MNPs @ DMSA at high concentrations (1.2 and 1.5 mM Fe) study results showed that they have some cytotoxicity on HPCs (PC3 and DU145).

Sharifi *et al.* [1.53] presented a systematic investigation on the structural and magnetic properties of $Co_{(1-x)}Zn_xFe_2O_4$ (0.5< x <0.75) nanoparticles which were synthesized by co-precipitation method. They showed by XRD analysis that the production of single cubic face with particle size 6-10nm. The FTIR measurement between 4000-400 cm^{-1} confirmed the intrinsic cation vibrations of spinal structure. It was found that the saturation magnetization and coercivity decrease with the increase of Zn concentration. Furthermore $Co_{0.3}Zn_{0.7}Fe_2O_4$ exhibited super-paramagnetic behavior and the Curie point of 790^0C.

Hochepied *et al.* [1.54] prepared Cobalt Zinc Ferrite ($Co_{0.73y}Zn_{0.73(1-y)}$ Fe_2O_4) nanoparticle in order to investigate their magnetic properties. The saturation magnetization changed with increasing y due to the various occupancies of cations in tetrahedral and octahedral sites and/or to an increase in the disorder of the ferrimagnetic structure. The cobalt content and particle size effects on the coercive field were studied. The increase in the ratio between remanent and saturation magnetizations indicates that, with increasing y, a transition takes place from uniaxial to cubic anisotropy At zero cobalt, this curve is characterized by a well-defined peak that disappears progressively with increasing y. The fit of the zero FC ~ZFC curve indicates an unrealistically high simulated saturation magnetization, consistent with a drastic field-dependent behavior of the ZFC-FC curves.

Lopez *et al.* [1.55] were prepared magnetic $Co_{(1-x)}Zn_xFe_2O_4$ ($x = 0.25, 0.5, 0.75$) ferrite nanoparticles via co-precipitation method from aqueous salt solutions in an alkaline medium. (TEM) studies permitted determining nanoparticle size; grain size of nanoparticle conglomerates was established via Atomic Force Microscopy. XRD pattern showed that the most intense peak corresponds to (311) crystallographic orientation of the spinal phase after that the mean crystal size was determined which complied with TEM result and FTIR Spectroscopy confirmed the presence of the bonds associated to the spinel structures; particularly for ferrites. At room temperature VSM study reviled the super-paramegnetic behavior of the nanoparticle.

Mamani *et al.* [1.56] used chemical co-precipitation method to synthesis Cobalt Zinc Ferrite nanoparticle and coated with lauric acid and dispersed in aqueous medium containing surfactant that yielded a stable colloidal suspension. Therefore magnetic nanoparticles were characterized in terms of their morphology by means of TEM, DLS, and XRD was used to characterize structural properties and pattern showed the presence of peaks corresponding to the spinel phase of magnetite (Fe_3O_4). The relaxivities r_2 and r_2 values were determined from the transverse relaxation times T_2 and T_2 at 3T. They performed magnetic characterization using SQUID and FMR and found super paramagnetic behavior of the nanoparticles. DSE studies showed exothermic events associated with the oxidation of magnetite to maghemite.

Nadeem *et al.* [1.57] prepared $Co_{(1-x)}Zn_xFe_2O_4$ (x = 0, 0.2, 0.3, 0.4, 0.5, and 1) nanoparticles using Sol-gel method and coated with 30% wet silica which prevent nanoparticles form agglomeration. Cubic spinal structure and crystal size 75 nm was confirmed by XRD analysis. Fourier transform infrared (FTIR) spectroscopy confirmed the formation of spinel ferrite and SiO_2. From the SEM image it has been found that nanoparticles were almost spherical and non-agglomerated. It is also found that the structural and magnetic property of the nanoparticles were strongly depends on the concentration of the Zn.

Veverka *et al.* [1.58] synthesized $Co_{(1-x)}Zn_xFe_2O_4$ nanoparticles of single spinal phase by co-precipitation method. Magnetic studies carried out in the range of 4.5 – 550K revealed gradual transition from ferrimagnetic to superparamagnetic to paramagnetic behavior depending on the composition and particle size. Particular importance can be ascribed to the composition of x = 0.6 where the observed transition temperature to the paramagnetic state at 310 – 334 K suggests applicability of this material for magnetic fluid hyperthermia in a self-controlled regime.

Akmal *et al.* [1.59] were prepared $Co_{(1-x)}Zn_xFe_2O_4$ co-precipitation method where NaOH use as a precipitating agent at 900^0C. The prepared ferrites were characterized using X-ray diffraction (XRD) and particle size was investigated by sheerer formula. The prepared Co-ferrites were found to be magnetized and particle size was ranged from 22 - 53 nm. The maximum spontaneous magnetization and minimum particle size was obtained at x = 0.25 when metal ion was in beaker. By reversing the solutions, the ferrites changed from spiral to inverse spiral with decreased particle size. It is found that ferrite properties were dependent to the co-precipitation condition such as concentration of metal ion and solution interchangeability.

Yadav *et al.* [1.60] were achieved $Co_{(1-x)}Zn_xFe_2O_4$ (x = 0, and 0.5) spinel ferrite nanoparticles at 800^0C by starch-assisted sol–gel auto combustion method and reduced particle size by ball-milled for 2 hours. FE-SEM was used to confirm formation of spherical nanoparticle and it was found that with ball-milling particle size decreased. An X-ray photoelectron spectroscopy (XPS) result indicated that Co^{2+}, Zn^{2+} and Fe^{2+} exist in tetrahedral and octahedral site. The change in saturation magnetization and coercivity with decrease of the nano crystalline and the distribution of the spinal ferrite cation were observed.

Ritu *et al.* [1.61] were prepared $Co_{(1-x)}Zn_xFe_2O_4$ (x = 0.1, 0.2, 0.4) by solution combertion method. They used XRD to determine the average crystallite sizes of the prepared sample which was consistent with the particle size obtained from TEM image. Fourier transform confirm the spinal phase structure of Cobalt Zinc Ferrite. Mössbauer spectra indicate that sample with 40% zinc concentration exhibits the collective magnetic excitations.

Sohorab *et al.* [1.62] reported the characterization of Co-Zn Ferrite. They observed the morphology of the nanoparticle by TEM and found the average particle size were about 16-40nm. The structural and crystal phase of CZF-MNPs was determined by X-ray diffraction (XRD) and the results confirmed the single phase spinel ferrite formation and the average of crystallite sizes was calculated about 13 nm using Scherrer.s formula from the broadening of the most intense peak (311). Magnetization measurement of the samples were performed up to maximum field 9000 Oe at room temperature by Alternating Gradient Field Magnetometer (AGFM) and showed the saturation magnetization was less than the bare sample. The FTIR result further confirmed Co-Zn phase.

Sonali *et al.* [1.63] prepared Zinc substituted Co ferrite nanoparticle $Co_{(1-x)}Zn_xFe_2O_4$ (x = 0, 0.2, 0.4, 0.8, and 1) via sol-gel route and investigated the effect of zinc concentration on saturation magnetization and lattice parameter. They found that the unit cell parameter ‘a’ increases linearly with increasing concentration of zinc due to larger ionic radii of Zn^{2+} ion. It was found that this substitution allows tunable changes in the magnetic properties of cobalt ferrite. But interestingly, saturation magnetization first increases upto x = 0.4 and then decreases for higher Zn substitution, thus tunable changes in magnetic properties of cobalt ferrite are possible. Source of such behaviour could be the variation of exchange interaction between the tetrahedral and the octahedral sites.

Sundararajan *et al.* [1.64] synthesized Co substitute Zn ferrite by microwave combustion method. They used Vibrating sample magnetometry at room temperature recorded to study the magnetic behavior of the samples. X-ray analysis confirmed the formation of zinc ferrite normal spinal-type structure with an average crystalline size in the range 25.69-35.68 nm. It is seen that lattice parameter decrease as cobalt fraction was increased. The SEM image showed nanoparticle are agglomerated. It has been found that the estimated band gap decrees with an increase of cobalt content. A gradual increase in the coercivity and saturation magnetization (Ms) were noted at relatively higher cobalt doping fractions.

Ding *et al.* [1.65] synthesized $Co_{0.6}Zn_{0.4}Fe_2O_4$ ferrite nanoparticles are successfully by four different hydrothermal routs. XRD pattern reveled that monophasic formation and good crystalline nature of as-synthesized samples. It was pointed out that the use of NaBH4 and a colloid mill can help to reduce the particle size and improve magnetic properties of the samples, which was proved by SEM images. It demonstrated that by changing raw material and mixing method during hydrothermal process, the structure, particle size, morphology and magnetic properties of the ferrite nanoparticles are controllable. This paper implies that the selection of a suitable hydrothermal route is very important to synthesize high-performance ferrite nanoparticles.

From the above mentioned previous research work it has been observed that researcher synthesized Co-Zn ferrite using different method. Analyzing different method of synthesis it is observed that chemical coprecepation method is one of the best method for nanoparticle synthesis. For analyzing the crystal structure XRD is used by all the researcher and VSM and Mossberg spectroscopy is used for determining the magnetic behavior. It has been found from the paper review, researcher were engaged mostly synthesis and characterization technique, but more research is needed in applications.

1.6 Objective of the Research Work

The objective of this research is to develop and characterized nanosize zinc doped cobalt ferrite nanoparticle and coated it by biocompatible material to exploit their pronounced ability to absorb the energy of the low frequency fields which is suitable for magnetic particle hyperthermia. Among various methods for synthesis of magnetic nanoparticle, co-precipitation process has several advantages over other methods including good homogeneity, low cost, high purity of product and not requiring organic solvent. So the cobalt zinc ferrite nanoensemble will be prepared chemical co-precipitation method where the PH of the solution will be kept controlled in the range 11-13. After that solvent will allowed to precipitate. Finally after washing the sample it will be annealed at 80^0C for 72 hours to get the final product. The outline of methodology might be enlisted below:

(i) Superparamagnetic nanaoparticle of $Co_{0.5}Zn_{0.5}Fe_2O_4$ have been synthesize by chemical co-precipitation method and annelid it at different temperature. After that the prepared ensemble will be coated by biocompatible coating.

(ii) The as-dried sample have been treated thermally at various temperature from 200^0C up to 1000^0C to study on the crystalline size evaluation.

(iii) XRD characterization have been done to know about the crystal structure and crystallinity.

(iv) Hydrodynamic size distribution of the sample will be investigate by dynamic light scattering (DLS).

(v) The VSM characterization have been performed to study the magnetic behavior of the synthesis nanomaterials along with all the characterization like saturation magnetization and coercivity.

(vi) Mossbauer studies have been performed to analysis the cation distribution. We will also measure the Isomer shift, Quadruple splitting and hyperfine field splitting.

(vii) The induction heating properties of the sample will be investigated by the magnetic hyperthermia setup and from here specific loss factor would be investigated.

1.6 Overview of the Research Work

This thesis deals with development of MNPs for biomedical application especially on hyperthermia study. Then some possible strategies are proposal and the most valuable ones are chosen in order to guide the work and after following this guideline scientific data are collected and result are discussed in order to check whether they fulfil the expected objectives and requirements. This thesis confined into five chapter which are follows.

In **chapter 1** includes the introduction of Co-Zn ferrites and organization of thesis. This chapter incorporates information to understand the aims and objectives of this investigation and also reviews of recent reports by other investigations with which these result can compared.

In **chapter 2** an introduction to general properties of the magnetic particles together with some theoretical background related to the present work have been discussed. Also a brief discussion of the various experimental techniques used to prepare the sample will be addressed.

In **chapter 3**, various experimental techniques used to characterization are briefly explained along with the description of the sample preparation.

C**hapter 4,** presents the structural and magnetic properties of the sample. The hydrodynamic diameter of the chitosan coated sample also have been described. Finally we report how the sample of different concentration response with external magnetic field and present the main findings of the result discussed step by step.

Finally in **Chapter 5**, an overall conclusion with the suggestions for the further research on this field will be given.

References are added at the end of all chapters.

FORMALISM OF NANOMAGNETISM

2.1 Introduction to Magnetism

The story of magnetism begins 2500 years ago with a material called magnetite (Fe_3O_4), which is the first magnetic material known to man. After a long time passed, the first scientific study of magnetism was made by the English scientist William Gilbert, who published his classic book 'On the magnet' in 1600BC. But the modern theory of magnetism, which is commonly well known as Maxwell's electromagnetic theory, here he showed that, electricity and magnetism are unified. He rewrite four common theory as

$$\nabla.\boldsymbol{E} = \frac{\rho}{\varepsilon_0} \tag{2.1}$$

$$\nabla.\boldsymbol{B} = 0 \tag{2.2}$$

$$\nabla \times \boldsymbol{E} = -\frac{\partial \boldsymbol{B}}{\partial t} \tag{2.3}$$

$$\nabla \times \boldsymbol{B} = \mu_0 \boldsymbol{J} + \mu_0 \varepsilon_0 \frac{\partial \boldsymbol{E}}{\partial t} \tag{2.4}$$

Here, equation (2.1) is known as Gauss's law, which told that how the electric field **E** diverges from the charge density ρ. ϵ is the permittivity of free space. Equation (2.2) is Gauss's law for magnetism, where **B** is the magnetic induction, which assumes no magnetic monopoles. Equation (2.3) represents how change in magnetic field produce electric field. However, a group of researcher [2.1] reported that magnetic monopole is possible and this lead to modify the equations (2.2) and (2.3) for describing magnetic monopole. The equation (2.4) is the modified form of Ampere's law which describing how a space varying magnetic field produce electric field. Where J is the current density and μ_0 is the magnetic permeability in space.

To describe magnetization it is need to define magnetic moment μ, which can be define through a current I around a small area dS as

$$d\mu = IdS \tag{2.5}$$

The origin of the magnetic moments that is the reason for magnetization of a magnetic material can either be the orbital motion or the spin motion of the electrons. The magnetization M is the result from the response to the external magnetic field and a unbalanced magnetic dipole moments due to the intrinsic properties of the materials itself. If N is the total number and V is the volume then magnetization M is the total magnetic moment per unit volume:

$$\boldsymbol{M} = \mu \frac{N}{V} \tag{2.6}$$

When a material is placed in an external magnetic field M, the induced magnetization is created which represents is by

$$\boldsymbol{M} = \chi \boldsymbol{H} \tag{2.7}$$

Where the proportionality constant χ is called the magnetic susceptibility of the material

$$\boldsymbol{\chi} = \frac{\mu}{\mu_0} - 1 \tag{2.8}$$

The equation (2.7) only veiled for magnetically anisotropic materials, this means the magnetic materials have no preference directions for its magnetic moment. However, the real crystals real crystals are anisotropic, which is when the magnetic moment of the material depends on the direction within the structure of the material, and it will self-align along an energetically favorable direction called an easy axis. Most common types of anisotropies are: the magneto-crystalline anisotropy where the crystallographic directions define the easy axes, and the shape anisotropy, important in non-spherical small particles where the easy axis is an axis along longest dimension. The response of a material to an external magnetic field H is called the magnetic induction B

$$\boldsymbol{B} = \mu(\boldsymbol{H} + \boldsymbol{M}) = \mu_0(\,1 + \chi)\boldsymbol{H} = \mu_0 \varepsilon_0 \boldsymbol{H} \tag{2.9}$$

The Bohr-van Leeuwen theorem [2.2] shows that when calculating an average of the magnetic moment, the partial derivative of the classical partition function Z with respect to magnitude of the magnetic induction B arises,

$$\langle \boldsymbol{\mu} \rangle = \frac{KT}{Z} . \frac{\partial Z}{\partial B} \tag{2.10}$$

and since the partition function does not depend on the magnetic induction, the classical calculation of the average magnetic moment will always give zero. Therefore the classical mechanics and statistical mechanics solely cannot account for magnetism in solids, because magnetism is a quantum mechanical effect.

2.1.1 Force on Magnetic nanoparticles

To understand how a magnetic field may be used to manipulate MNPs, we need to recall some elements of vector field theory. This is not always institutive and the reader is directed to recent reviews for further details [2.3-2.5]. It is also important to recognize that the magnetic field quadrant is required to exert a force at a distance; a uniform field given rise to the torque, but no translational actions. Start from the definition of the magnetic force acting on the point like magnetic pole m

$$F_m = (m. \nabla) B \tag{2.11}$$

Which can be geometrically interpreted a differentiation with respect to the direction of m. For example, if m= (0, 0, m_z) then $m. \nabla = m_z (\frac{\partial}{\partial x})$ and a force will be experienced on the dipole provided there is a field gradient in B in the Z-direction. In the case of MNPs suspended in the weakly DM medium such as water, the total moment on the particle can be written $= V_m M$, where V_m is the volume of the particle and M is the volumetric magnetization, which in turn is given by $M = \Delta X H$, where $\Delta X = X_m - X_n$is effective susceptibility of the particle relative to the water. We can approximate the overall response of the particle in plain water system by $B = \mu_0 H$ so that the equation (2.11) becomes

$$F_m = \frac{V_m \Delta\chi}{\mu_0}(B.\nabla)B \qquad (2.12)$$

Furthermore, provided there is no time varying electric fields or current in the medium, we can apply the Maxwell equation $\nabla \times B = 0$ to the following mathematical identity.

$$\nabla(B.B) = 2B \times (\nabla \times B) + 2(B.\nabla).B = 2(B.\nabla)B \qquad (2.13)$$

To obtain more intuitive form of equation (2.12)

$$F_m = V_m \Delta\chi \nabla(\frac{B^2}{2\mu_0}) = V_m \Delta\chi \nabla(\frac{1}{2}B.H) \qquad (2.14)$$

In which the magnetic force is related to the differential of the magneto static field energy density $\frac{1}{2}B.H$, Those if $\Delta\chi > 0$ the magnetic force acts in the direction on the steepest ascent of the energy density scalar field. This explain why, for example, when iron filings are brought near the pole of a permanent bar magnet, they are attracted towards that pole. It is also the basis for the biomedical application of magnetic separation and drug delivery.

2.2 Types of Magnetism

The behavior of the magnetic materials can be classified into five category as diamagnetism, paramagnetic, ferromagnetism, anti-ferromagnetism and ferrimagnetism. The magnetic susceptibility for the diamagnetism are negative but in the case of paramagnetic and anti- ferromagnetism materials is weak which unlikely use in magnetic applications are. From figure 2.1 it is found that the ferromagnetic materials have parallel alignment, which resulting in strong spontaneous magnetization below the Curie temperature. But over the Curie temperature ferromagnetic materials become paramagnetic. [2.6] Anti-ferromagnetism and ferrimagnetism have their similar alignment of magnetic moment which align in the opposite directions, but in the case of ferrimegnetic materials the opposite moments are unequal which produce a net magnetism. Ferrimagnetic materials like ferromagnetic become paramagnetic at or above the Curie temperature.

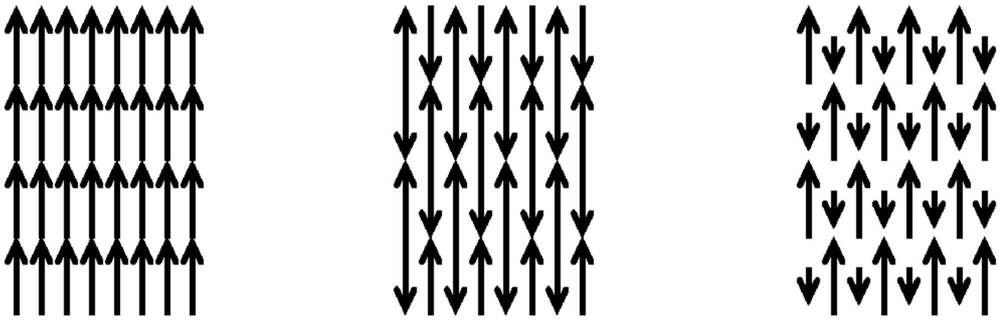

Figure 2.1: Magnetic arrangements of ferromagnetic, anti-ferromagnetic and ferrimagnetic materials

2.3 Hysteresis loop

For unmagnetized bulk material, there is a zero magnetic moment. It can be predicted that there will be an infinite number of degree of magnetization between unmagnetized and saturation magnetization condition. When the materials is subjected to an external magnetic field, these extreme situation corresponds respectively to random orientation of domain complete alignment is one direction with the elimination of the domain walls. If we start with the applied magnetic field, the bulk material will be progressively magnetized by the domain dynamics. The magnetization of the sample will follow the path as shown in the dotted line in the figure 2.2. Firstly, the lower section, is in the initial susceptibility region and characterized by reversible domain wall movement and rotation.

The shape of the hysteresis cure is the important factor for discussing magnetic materials. When a magnetic materials is magnetized in one direction in influence of external magnetic field, it will track back to zero after the applied magnetic field is keep away. In addition, if an opposite magnetic filled is applied to this materials, its magnetization will trace out a loop is known as hysteresis loop [2.7]. In figure 2.2 shows the B-H curve which following the path of a-b-c-d-e-f-a as the alternating magnetic is applied.

i. Point ‘a’: If the magnetizing field is applied in the positive direction then the value of magnetic flux density B will increase as shown in the curve and become nearly constant at the point ‘a’, where the magnetic domain are same in order, hence the materials reach is saturation value. Here, in the case of an additional increase in magnetizing force, there will be only a little increase in the magnetic field.

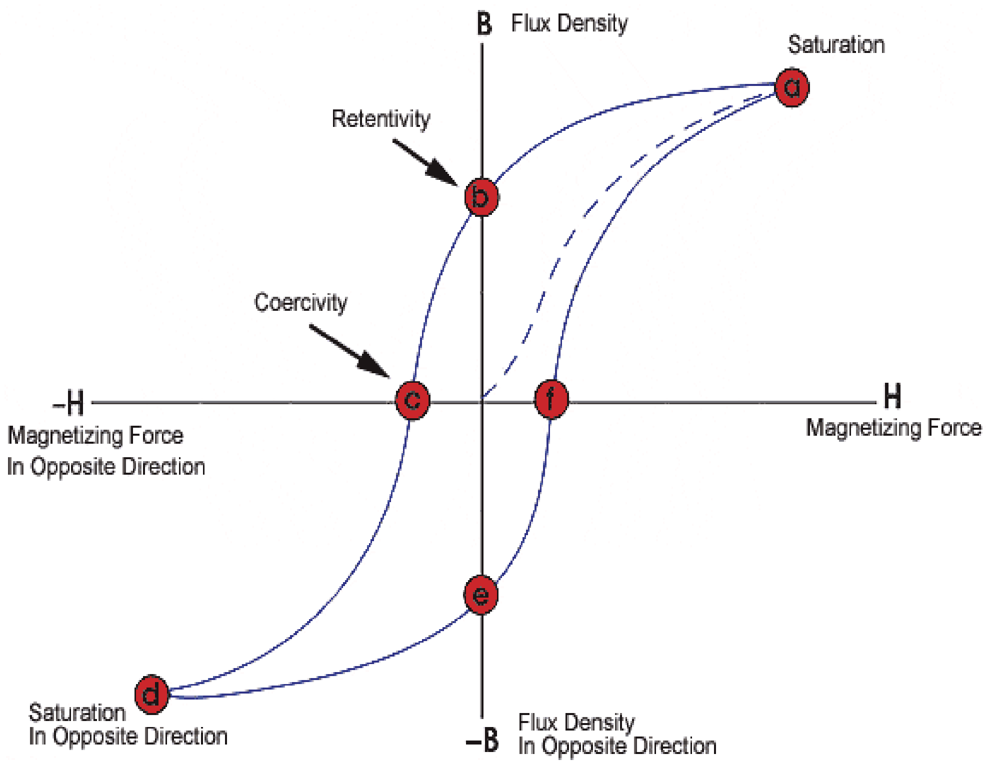

Figure 2.2: Hysteresis loop

ii. Point ‘b’: Now if the magnetizing force is reduced to zero, B transform from point ‘a’ to the point ‘b’, there is still some magnetic flux kept by the material. This point is also at where one should look for retentivity on the graph, showing and indicates the level of magnetism retained in the material.

iii. Point ‘c’: At this point, the magnetizing force is reversed leading to a decrease in flux down to zero. This is also the coercivity point which is parallel to the point ‘b’.

iv. Point ‘d’: Here, there is a negatively increase in the magnetizing force and hence, the material again reaches the maximum saturation in magnetization in opposite direction.

v. Point ‘e’: H is decreased down to zero at this point. The magnetism retained in the material at this stage is also equal to one at the point b with the opposite direction.

The shape and size of the hysteresis loop heavily depends on the magnetic properties of magnetic materials. For particular application need particular magnetic materials. By using the hysteresis loop, one can get some specific information about magnetic properties of materials, such as retentivity, coercive force, residual magnetism, permeability and reluctance. The retentivity and residual magnetism are interrelated by the way that the first one is the concept standing for the ability of the materials to keep a certain amount of field though the magnetic field is removed, but in the case of latter one is the flux density retaining in the materials in null magnetic force. This two are same in the saturation point.

2.3.1 M-H Curve

Figure 2.3 shown that a schematic diagram of the M-H curve of four different types of magnetic materials. Most materials display little magnetism, and even then only in the presence of an applied field: these are classified as paramagnetic materials for which χ fall in the range 10^{-6} to 10^{-1} or diamagnetic, with χ in the range 10^{-6} to 10^{-3}. However, some materials exhibit ordered magnetic state and are magnetic even without an external field; these are classified as ferromagnetic, ferrimegnetic, and antiferromagnetic materials. Where the prefix refers to the nature of the coupling interaction between the electrons within the materials [2.8]. This coupling can give rise to larger spontaneous magnetization: in ferromagnetic materials M is typically 10^{4} larger than would appear otherwise. The susceptibility in order materials depends not just on temperature but also on H, which give rise to the characteristic sigmoidal shape of the M-H curve, with M approaching a saturation value at large values of H. Furthermore, in ferromagnetic and ferrimagnetic materials one often sees hysteresis which is an irreversibility in the magnetization process that is related to the pinning of magnetic domain walls at impurities or grain boundaries within the materials, as well as to intrinsic effect such as the magnetic anisotropy of the crystallite lattice. This give rise to open M-H curves, called hysteresis loop. The shape of these loops are determined in part by particle size: in large particles there is a multiple domain ground state which leads to a narrow hysterias loop since a fake relatively lattice field energy to make the domain walls move; while in smaller particles there is a single domain ground state which leads to a broad hysterias loop. At even smaller size of the order of tens of nm or less. One can see the superparamagnetic, where the magnetic moment of the particle as a whole is free to fluctuate in response to thermal energy, while the individual atomic moments maintain their order state relative to other. This leads to the an hysteretic; but still sigmoidal M-H curve shown in the figure 2.3.

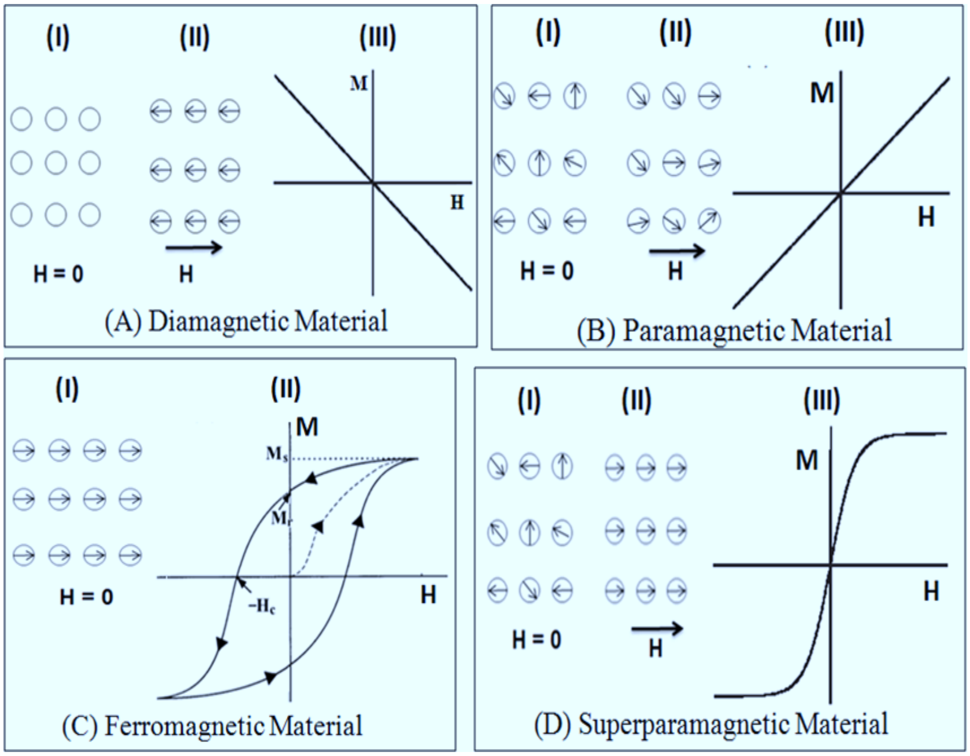

Figure 2.3: Graphical presentation of interaction of the magnetic moment M with external field H and M-H curve for (A) Diamagnetic, (B) paramagnetic, (C) ferromagnetic and (D) superparamagnetic materials

In figure 2.3 shows in ferromagnetic materials, in absence of external magnetic field magnetic moment M aligned parallel. So for that hysteresis loop is observe with remenence and coercivity. On the other hand, superparamagnetic materials shows the similar pattern but with the absence of hysteresis loop, remanence and coercivity. For the biomedical application especially on hyperthermia therapy need superparamagnetic material. Those materials shows some special properties of hysteresis loop like zero retentivity and zero coercivity. The M-H curve for the ferromagnetic and Superparamagnetic nanoparticle is represents below. There are a large number of iron oxide compounds like γ- Fe_2O_3, γ- Fe_2O_4 shows super paramagnetic behavior.

2.4 Magnetic nanoparticles and Single Domain Particles: Superparamegnetism

The nanoscale magnetic materials has gain a lots attention to the researcher over the last decade not only for the business and technological reasons, but also fundamental research point of view. For finding biomedical application like improving the quality of magnetic resonance imaging (MRI), hyperthermia treatment for malignant cells, site-specific drug delivery etc. nanoscale magnetic materials are used since over the last decade. [2.9]

Pierre Weiss *at. al* [2.10], first explain the behavior of the hysteresis of ferromagnetic bulk materials by using the concept of domains. Ferromagnetic materials are consist of domains, which are separated by domains wall. This domain wall try to minimize the net energy of the system. The magnetostatic energy and domain wall energy increase proportionally to the volume and surface respectively. When the particle size lower than the critical size, surface area is increased as well the domain energy so it became unfavorable for creating domains. In this situation, single uniform domain is formed and system behave as a small permanent magnet. The size of the single- domain particle depends on the material and contributions from different anisotropy energy terms. The critical radius below which a particle acts as a single domain particle e is given by [2.11]

$$\boldsymbol{r_c} = 9\frac{(AK_u)^2}{\mu_0 {M_s}^2} \tag{2.15}$$

Where A define as exchange constant, Ku is the uniaxial anisotropy constant, μ_0 is constant of permeability, and Ms is the saturation magnetization. The typical value for the critical radious depends on the materials. Depending on the size and material, the magnetic moments of single domain particles can be 102-105 μB where μB is the Bohr magneton [2.12]

Different model for describing the magnetization of single domain particles developed by different scientist. Stoner and Wohlfarth are two of those, assumed non-interacting particles with uniaxial anisotropy in which spins are parallel and rotate at union. Furthermore, at any finite temperature, the thermal activation can overcome the anisotropy energy barrier leading to switching of the particle moment. This relaxation process was first proposed by Neel in 1949 and further developed by the Brown [2.13-2.14]. This function is commonly used to fit experimental magnetization curve of nanoparticles and to determine the size of the crystal and its specific magnetization. The characteristics features of superparamagnetic nanoparticles are their response to the magnetic field, where there are no remenent magnetization and very high field of saturation magnetization [2.15].

A typical feature of superparamegnetic nanoparticles is the Neel relaxation time τ_N, that is the time constant. It can be expressed as:

$$\tau_N = \tau_0 (\frac{KV}{K_B T}) \tag{2.16}$$

Where $\tau_0$the pre-exponential factor is called characteristic relaxation time, $K_B$is the Boltzmann constant and T is absolute temperature. This time is characteristic time for the internal relaxation of magnetization of nanoparticles. According to the equation (2.16), the volume of nanoparticles and the temperature are two critical parametric affection to the Neel relaxation time and therefore the superparamegnetic or thermally blocked behavior of the system.

2.5 Superparamegnetism and its limit

Superparmagnetism is a form of magnetism which is exhibit by ferromagnetic and ferrimagnetic single domain nanoparticles of size is less than 100nm. The state of superparamagnetism means to how the average magnetization of the nanoparticles average to zero when the external field is removed in addition Neel relaxation time is less than the measurement time for the magnetization. But when the magnetic field is applied, the nanoparticles behave as paramagnets with high susceptibility. The magnetization of the single domain nanoparticles lie parallel or antiparallel to a particular direction known as easy axis.

Consider a group of uniaxial, single-domain particles. Each particle have an anisotropy energy density $E = KVSin^2\theta$, where θ is the angle between the direction of magnetization and the easy axis, K is the energy density of anisotropy and V is the volume of the particle. At H=0, the two minima $\theta = 0$ and $\theta = \pi$ are separated by the energy barrier $\Delta E = KV$ corresponds to the magnetization parallel or antiparallel to the easy axis which shown in figure 2.3. Neel stead in his model that, KV become small if the single domain particles become small. Result is the energy fluctuation can overcome the anisotropy energy and spontaneously reverse the magnetization of a particle from one easy direction to other, though there is no applied magnetic field.

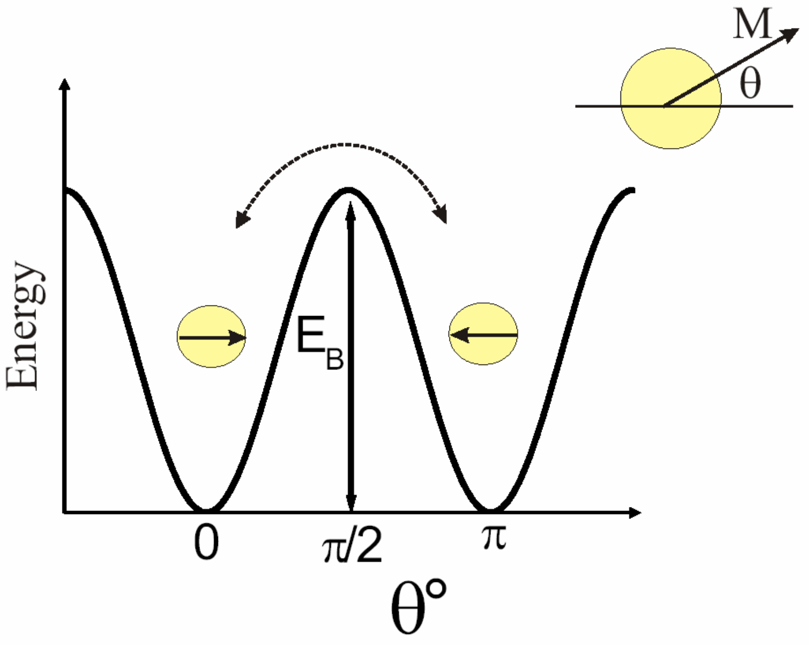

Figure 2.4: Schematic diagram of the energy of the single domain particles with unixial anisotropy as a function of magnetization direction.

If $KV \gg K_BT$ then the moment of the magnetic nanoparticle cannot switch spontaneously and the system behave like a permanent ferromagnetic. But in the case of $KV{\sim}K_BT$ or less the spontaneous became ‘superspins’ and this state is known as superparamagnetic nanoparticle. The thermally agitated fluctuations of the superspin-direction take for the characteristic relaxation time $\tau = (2\pi f)^{-1}$, where f is the frequency of the magnetic field. The quantitative representation for the relaxation time, that is the time constant of the return to equilibrium of the magnetization after excitation, is given by Neel-Brown model as shown in the equation (2.16). There is a size limit that divides the internal relaxation occurring in single domains in two different time regimes, slow and fast relaxation compared to a characteristic measurement of time of the method used to investigate the magnetic behavior of the system. But in presence of magnetic field in the equation (2.16) become:

$$\tau_N = \tau_0 \left(\frac{\Delta E(H,\theta)}{K_B T}\right) \qquad (2.17)$$

Where $\Delta\mathrm{E}(H,\theta)$ is the field dependent energy barrier which can express as

$$\Delta E(H,\theta) = \Delta E_0 (1 - \frac{H}{H_w})^k \qquad (2.18)$$

At the high temperature the magnetic moments fluctuate rapidly but this fluctuations slow down as the sample is cooled and the system appears static. At this static point τ_N become much longer than the experimental measurement time, τ_m this particle is said to be blocked. And this characteristic temperature is known as blocking temperature T_B. A blocking volume V_B and a blocking temperature T_B can be defined in order to distinguish the superpara magnetic single domains from the thermally blocked ones

$$V_B = \frac{K_B T}{K} \ln(\frac{teyp}{\tau_0}) \qquad (2.19)$$

and

$$T_B = \frac{KV}{K_B In\left(\frac{t_m}{\tau_0}\right)} \qquad (2.20)$$

It is important to notice that the blocking limit is dependent of the experiment time, and it is possible to obtain different values of V_B and T_B for different techniques. For instance, vibrating sample magnetometer (VSM) has a characteristic measurement time of 10s, while superconducting quantum interference device (SQUID) has a measuring time of 10^{-2} s and Mössbauer spectroscopy 10^{-8} s [2.16].

For biomedical application, nanoparticles should be coated by biocompatible materials like chitosan, PEG etc. In that case nanoparticle are remain suspended in liquid. When nanoparticles are suspended in liquid, their motion in the liquid which known Brownian motion need to be considerate. There are two types of Brownian motion, translational motion and rotational motion. The translational motion can be determined by dynamic light scattering (DLS) or by using Stocks-Einstein equation [2.17]:

$$\tau_L = \frac{3\pi\eta D_H}{K_B T q^2} \tag{2.21}$$

Where, η is the viscosity of the liquid, D_H the hydrodynamic diameter of the particle and q is the light scattering wave number. The rotational motion can be described by a characteristic rotational diffusion time, according to:

$$\tau_B = \frac{\pi\eta D_H^3}{2K_B T} \tag{2.22}$$

It is possible to determine the rotational Brownian relaxation of magnetic nanoparticles through magnetic measurements of the frequency dependent complex susceptibility [2.22].

A typical ferrofluid has a wide range of distribution of particle size. Neel and Brownian motion occur in parallel, so that the effective relaxation time is given by:

$$\frac{1}{\tau_{eff}} = \frac{1}{\tau_N} + \frac{1}{\tau_B} \tag{2.23}$$

Both the Neel and the Brownian relaxation processes are contributing to the effect of time, while the translation motion time is neglected because it does not affect magnetic measurement. Figure 2.5 represent the different time constant related to the different relaxation mechanism for nanoparticle in suspension as s function of their radius.

It is clear from the above equation that the effective relaxation time is dominated by the shorter of the two component, while the translational motion time is negate because it has no effect in magnetic measurement. Figure 2.4 shows the Neel and Brownian contributions to the relaxation time of a spherical magnetic nanoparticle. There are two ways to measure the relaxation phenomena: either in the time domain or in the frequency domain. By measuring the complex susceptibility it is therefore possible to determine the Brownian relaxation time and the mean hydrodynamic volume of the nanoparticles. The coercivity is an important parameter in magnetic properties. Low coersivity is a feature for soft magnetic materials, while larger coercivity is required for the hard. Furthermore the coercivity shows the strong dependence on the particle size. From the figure the coercivity reaches a maximum value when the particle size become single domain below the critical diameter (approximately 200 nm).

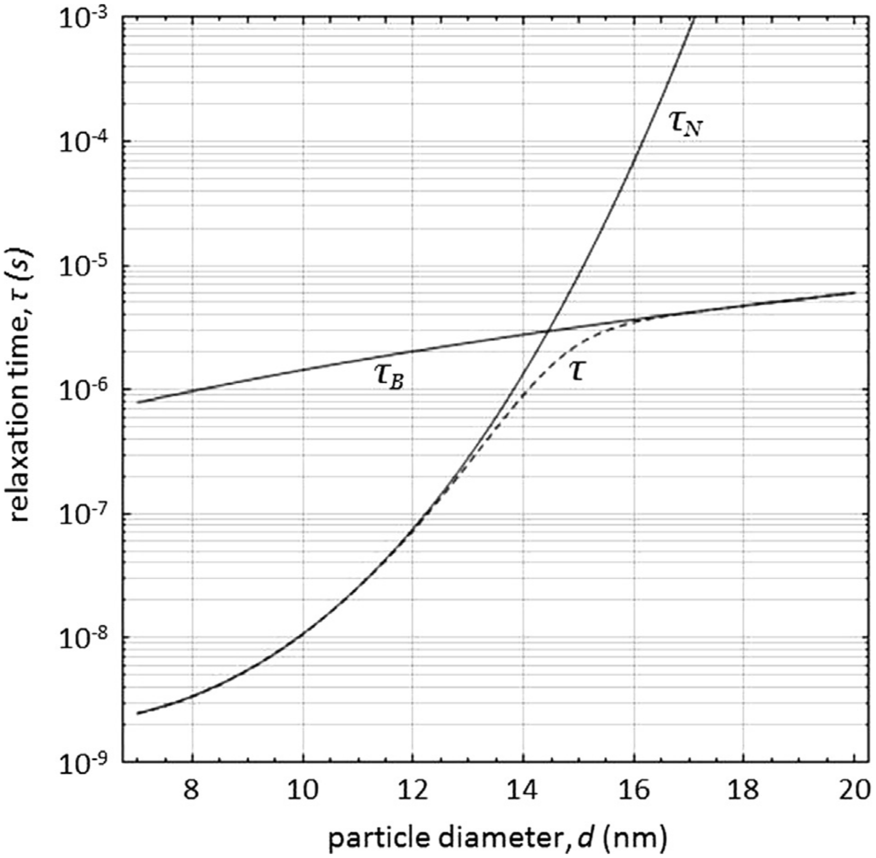

F**igure 2.5:** Time constant vs particles size for magnetite particles

In the PSD position the coercivity decreases for the smaller particle size due to the randomizing effect of thermal energy. Below the critical diameter the coercivity of the particle is zero due to the thermal effect, here particle shows superparamagnetic behavior. The property of superparamagnetism is achievable at room temperature in nanoparticle systems with diameters in the range of 10 to 100 nm, for relaxation times on the order of milliseconds. This is highly attainable in laboratory settings and the ability to produce a system with zero coercivity has many possible applications. However, in some cases the superparamagnetic limit represents a difficulty, as in making hard drives. As the size of a bit stored on the surface of a magnetic material gets smaller, the superparamagnetic limit is approached. If the bit has no coercivity, then its direction of magnetization flips randomly and with no external energy input. This makes it unsuitable for data storage.

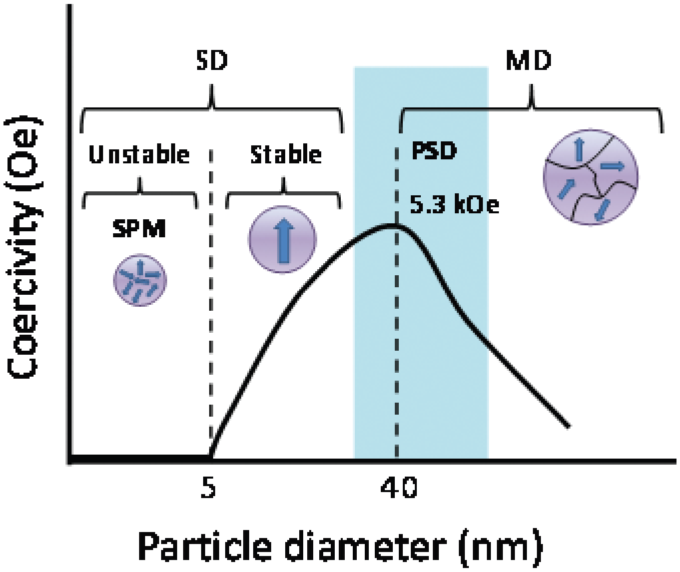

Figure 2.6: particle size Vs coercivity showing onset of superparamagnetism

2.6 Size effect on the Surface to Volume Ration

Surface area to the volume ratio in nanoparticles have a tremendous effects on the properties of the nanoparticles. The surface area is the measure of how much exposed area of a solid object has. The balk materials have the lesser surface area than the nanoparticle have, though their volume is same. The surface area to volume ratio increases with the decreases of the particle size, more specially the radius of the nanosphere. The reason behind that is as the particle size decreases, a greater number of atoms are found at the surface. For instance, a particle of size 4 nm has 50% of its atoms on its surface, at 12 nm 20% and 36 nm has 5% of its atoms on its surface.

Nanoscale material have their much greater surface area compare to the bulk materials, which can lead better change their properties. The greater surface area leads greater chemical reactivity and physical strength. At the nanoscale level the quantum effect of the particles appear more importantly, leading to better optical, electrical and magnetic behavior. For example, at the nano-scale, properties like electrical conductivity and mechanical strength are not the same as they are at the bulk size [2.19]. As the surface area increases, chemical sensors from nanoparticles and nanowires enhanced the sensitivity and sensor selectivity. The energy band structure and charge carrier density in the materials can be modified quite differently from their bulk and in turn will modify the electronic and optical properties of the materials.

As a great deal of interesting and relevant physics occurs at surface level, greatly increasing surface area can produce some very interesting results. For example, it is because of this disproportionate change between surface area and volume that living cells are limited in size. Consider that the volume of the cell represents the amount of products or actions that the cell can create or accomplish. The surface area is the “wall” or “doorway” for nutrients to enter the cell and products or waste to be removed from the cell. As the cell gets larger, the volume increases as a cube of the diameter. For example, the amount of nutrients or products that the cell can produce increases by that amount. Yet the surface area only increases as the square of that amount; hence, we get to a point where the cell needs more nutrients to feed the internal processes that the available surface area can allow in.

2.7 Synthesis of Nanomaterials

The man in his quest for knowledge has been conceiving and developing physical world and its components in bigger than the biggest and smaller than the smallest dimensions of mass, length and time. Though the smallest entity with individual characteristic features that was established happened to be an atom of an element but realization of the single atom in physical form and serving mankind remained a dream till recently. It is achieved through the development of nanocrystaline materials, discovery of concept of quantum confined atom and synthesis of doped nanocrystaline materials. Investigation of growth mechanism of nanoparticles is present large scientific and practical interest.

The synthesis of nanoparticles can be divided into two categories: the bottom-up and the top-down approaches. The top-down method is seen as the physical approach, which involves breaking down bulk material into nanoparticles through techniques such as acid-etching, ball-milling, and laser ablation. Conversely, the bottom-up method relies on chemical nucleation to form nanoparticles from molecular precursors. Electrochemical methods, sonolysis, thermal decomposition, and co-precipitations all fall into this category. In the bottom-up approach, nucleation and crystal growth stage of the nanoparticle formation can be carefully manipulated. So for that, it is possible to reduce polydispersity (degree of size differ with respect to each other) in the final product, while it is not possible for top-down approaches. For synthesis nanoparticle it should be considerate that the reaction condition and rate would be same otherwise the broadening of the particle size distribution will be occurred. The mechanism for monodisperse particle nucleation and growth was laid down by Viktor K. LaMer in 1950 to describe the nucleation and growth of sulphur sols, [2.20- 2.21] and is still used as the standard model today, although different to transition metal nanoparticle syntheses. [2.22].

According to the LaMer model, three stage are involved to synthesis monodisperse particle. From the figure 2.7, the first stage involve the increase of the nanoparticle monomer concentration to supersaturation. The nucleation only be occurred when the nucleation energy barrier is overcome the condition of supersaturation, which shows in figure 2.7 in stage (II). After satisfying the nucleation condition, bonds are formed among the nanoparticles monomers. Finally as the bonds formed the concentration of the monomer decreased and nanoparticle grow. In order to get a monodisperse product, it is important that nucleation in a single events, for growing in a single rate. After monomer are consumed, the model enters its final stage, crystal growth (Stage III). Crystal growth is diffusion controlled, with rates of growth determined by the rate of monomers diffusing to the nanoparticle surface.

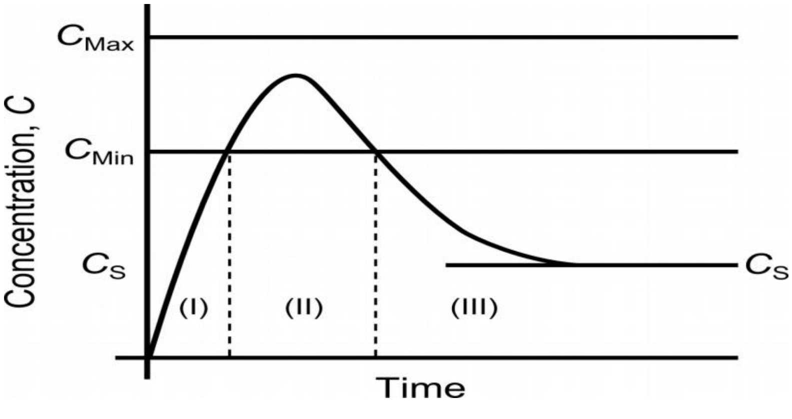

Figure 2.7: The LaMer model of nanoparticle nucleation and growth separated into three distinct phases

2.8 Controlled Synthesis: Theory of Nucleation and Crystal Growth

The common feature of the solution based approaches is the precipitation of solid product from the homogeneous solutions. Precipitation of solid particles is a dynamic process involving three stage: Nucleation, growth and coarsening/aggregation [2.24]. The LaMer model proposed a diagram showing the variation of the solute concentration in time where three regions, corresponding to the prenucleation, nucleation and growth processes, can be easily identified figure 2.7 [2.24-2.25]

When the concentration of a solute in a solvent exceeds its equilibrium solubility or temperature decreases below the phase transformation point, a new phase appears. Let us consider the case homogeneous nucleation of a solid phase from a supersaturated solution as an example. A solution with solute exceeding the solubility or supersaturated possesses a high Gibbs free energy; the overall energy of the system would be reduced by segregating solute from the solution. This reduction of Gibbs free energy is the driving force for both nucleation and growth. The change of Gibbs free energy per unit volume of the solid phase, ΔG_v, is dependent on the concentration of the solute:

$$\Delta G_v = -\frac{KT}{\Omega ln\frac{C}{C_0}} = -\frac{KT}{\Omega \ln(1+\sigma)} \tag{2.24}$$

Where C is the concentration of the solute, C_0 is the concentration of equilibrium, Ω is the atomic volume and finally σ is the supersaturation represented by $\frac{(C-C0)}{C0}$. Without supersaturation (i.e., σ = 0), ΔG_v is zero, and no nucleation would occur. When C > Co, ΔG_v is negative and nucleation occurs spontaneously. Assuming a spherical nucleus with a radius of r is formed, the change of Gibbs free energy or volume energy, $\Delta \mu_v$, can be described by:

$$\Delta \mu_v = \frac{4}{3}\pi r^3 \Delta G_v \tag{2.25}$$

However, this energy reduction is counter balanced by the introduction of surface energy, which accompanied with the formation of new phase.

This results in an increase in the surface energy, $\Delta\mu_s$, of the system:

$$\Delta\mu_s = 4\pi r^2\gamma \tag{2.26}$$

Where γ is the surface energy per unit area. The total change of chemical potential for the formation of the nucleus, ΔG, is given by:

$$\Delta G = \Delta\mu_v + \Delta\mu_s = \frac{4}{3}\pi r^3\Delta G_v + 4\pi r^2\gamma \tag{2.27}$$

In the synthesis and preparation of nanoparticles or quantum dots by nucleation from supersaturation solution or vapor, this critical size represents the limit how small nanoparticles can be synthesized. To reduce the critical size and free energy, one need to increase the change of Gibbs free energy, ΔG_v, and reduce the surface energy of the new phase, γ. This equation assumes a spherical nanoparticle of radius "r" and surface energy per unit area "γ". If a plot of Gibbs free energy "ΔG" against particle radius, a maximum is achieved at a critical nanoparticle radius, "r_c". This leads to an important consequence; nanoparticle nuclei larger in size than "r_c" will grow whereas nuclei smaller than "r_c" will dissolve back into solution.

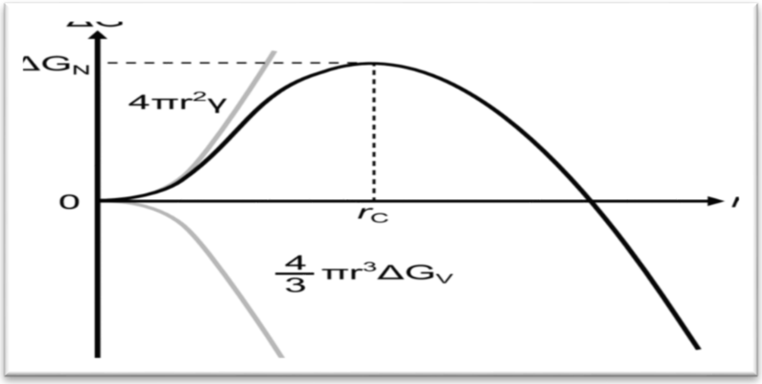

Figure 2.8: Plot of Free energy against nanoparticle nucleus radius showing the maximum at the critical radius and free energy maximum

The crystal growth is the last stage of the LaMer model. Nuclei larger than the critical radius "r_c" grow until all monomers have been consumed, *via* an intermediate state.

This process is temperature dependent, with high temperatures yielding fast crystal growth. Kinetically, crystal growth is a slow process when compared to nucleation and proceeds for homogeneous and uniform particle size increases at relatively low temperatures.[2.26] Crystal growth is diffusion controlled, with monomers diffusing from bulk solution to an interfacial layer close to the surface of the nanocrystal ("flux", "I_{diff}") which can be modelled using Fick's law. From the Stokes-Einstein-Debye equation

$$I_{diff} = 4\pi\sigma^2 J = 4\pi\sigma^2 D\frac{d[C]}{d\sigma} \tag{2.28}$$

At the pure reaction limit, monomers will diffuse to the surface and react according to the reactivity and concentration of adsorbates in solution, so "$[C_i]$= $[C_d]$". However, instances of crystal growth almost always occur in between these imposed limits. The instantaneous size-dependent growth rate is given in equation:

$$\frac{dr}{dt} = DV_m(\frac{[C_b] - [C_\infty]e^{\frac{2rV}{rRT}}}{\left(r + \frac{D}{K_r}\right)}) \tag{2.29}$$

This equation takes into account surface and volume terms with respect to diffusion of monomers to and from the surface. It also shows the temperature dependence of the rate of crystal growth meaning faster growth will occur at higher temperatures.

2.9 Preparation of Nanoparticle by Physical Approach

Preparation of nanomaterial is an important part of nanotechnology. Synthesis of nanomaterial with specific properties has attracted a huge attention to the researcher. The MNPs can be made to reasonably respond to a time varying magnetic field, with advantageous result related to the transfer of energy from the exciting field to the nanoparticle. For example, the particle can be made to heat up, which lead to their use as hyperthermia agents, delivering thermal energy to the targeted bodies, such as tumor. Most important physical approaches include evaporation-condensation and laser ablation. Various metal nanoparticles such as silver, gold, lead sulfide, cadmium sulfide, and fullerene have previously been synthesized using the evaporation-condensation method. The absence of solvent contamination in the prepared thin films and the uniformity of nanoparticles distribution are the advantages of physical approaches in comparison with chemical processes. Although they are simple, inexpensive and easily scalable, physical methods present limited control over the morphology and /or chemical composition of the final products. On the other hand ‘bottom-up’ manufacturing which involves building up of the atom or molecular constituents as against the top method which involves making smaller and smaller structures through etching from the bulk material as exemplified by the semiconductor industry.

2.9.1 Inert Gas Condensation

This method is one of the earliest method to synthesize nanoparticles. In this method, materials are evaporated first then cool them by using inert gas, at a very low pressure, usually 1mbar. So for that this method is known as inert gas evaporation method. Granqvist and Buhrman, 1976 described inert gas forwarded towards evaporation source and nanoparticles are transported towards a N_2 cooled substrate via thermophoresis over the evaporation source [2.27]. This methods was further developed by Birringer *et al.*, 1984. His modification consists of a scraper and a collection funnel allows the production of relatively large quantities of nanoparticles, which are agglomerated but do not form hard agglomerates and which can be compacted in the apparatus itself without exposing them to air [2.28]. The particle size is depends proportionally on the increasing pressure and molecular weight of the inert gas. This method is widely used commercially. There are several evaporation methods are used to synthesis nanoparticle. Sputtering, laser evaporation are the most common uses. Another method introduced by Kear and Strutt, in 1995 name Chemical Vapor Condensation, which replaces the evaporation boat by a hot-wall reactor in which an organometallic precursor in a carrier gas is introduced [2.29]. Another fantastic technique is also used in synthesis nanoparticle named as Gas Deposition method. In this method, nanoparticles are formed by evaporation in an inert gas at atmospheric pressure and transported by a special designed transfer pipe to the spray chamber at a pressure of about 0.3 mbar. By moving the nozzle at the end of the transfer pipe, the particles which have a mean velocity of 300 m/s can be deposited in required places on the substrate in the spray chamber. Oda *et al.*, 1992 [2.30] find micron sized pattern using this technique.

2.9.2 Sputtering

Another interesting and efficient physical technique is sputtering. In this methods, solid surface is vaporized by bombardment with a high velocity ions of inert gas, causing an ejection of atoms and cluster. Sputter sources such as an ion gun or a hollow-cathode plasma sputter source are normally used in vacuum systems, below 10^{-3} mbar, as a higher pressure hinders the transportation of the sputtered material. Instead of ions, electrons from an electron gun can be also used. Different research used different condition for synthesis, i.e Iwama *et al.* (1982)[2.31] operated an electron gun at 10^{-5} mbar separated by a differential pumping system from a 1 mbar evaporation chamber in order to evaporate Ti and Al targets in a N_2 or NH_3 atmosphere, producing TiN and AlN nanoparticles smaller than 10 nm whereas Günther and Kumpmann (1992)[2.32] applied an electron beam in an inert gas atmosphere with pressures up to 5 mbar in order to produce 5 nm Al_2O_3 and SiO_2 particles. Hahn and Averback (1990)[2.33] showed that a DC/RF magnetron sputter source can be operated in the mbar range, ejecting nanoparticles of sizes between 5 and 20 nm. Sputtering has the advantage that it is mainly the target material which is heated and that the composition of the sputtered material is the same as that of the target.

2.10 Preparation of Nano Ferrites by Chemical Methods

Although the physical methods are simple and versatile, enabling the preparation of a wide variety of ferrite nano-powders in large quantities and with a relatively low cost , their reliability is often questionable due to the contamination of the products and the limited control of the morphology of the resulting man-sized materials. Along with the chemical composition were found to be influenced significantly the magnetic properties of the ferrite nanoparticles and therefore their potential application in high density magnetic storage device [2.34], magnetic refrigeration [2.35], and magnetic resonance imaging [2.36], magneto-optical device [2.37] and ferrofluids [2.38]. There are many other uses of MNPs describe by the researcher [2.39-2.40]. The disadvantage of the chemical methods lie in the fact that some of them are highly toxic reagents as metal precursors and necessitate a rigorous control over the reaction parameters in order to obtain nanocrystaline ferrite with the desired morphology. For biomedical application required solubility in aqueous media. Several solution-based approaches both in aqueous and non-aqueous media, such as co-precipitation, micro combustion, sol-gel, hydrothermal etc. are the common method for preparation of MNPs.

2.10.1 Chemical precipitation and Co-precipitation methods

The chemical precipitation method is the pre-version of co-precipitation method for nanoparticle synthesis. Chemical reaction, nucleation and crystal growth are the three main steps by which consists of chemical precipitation method. This process is not a controlled process in terms of reaction kinetics and solid phase nucleation and growth processes which lead a wide particle range distribution and uncontrolled particle morphology, along with agglomeration. After a series of development researcher find a path to synthesis narrow size distribution of nanoparticles. The necessary requirements are (a) a high degree of supersaturation, (b) a uniform spatial concentration distribution inside a reactor and (c) a uniform growth time for all particles or crystals.

One of the most efficient and common method for the synthesis of nanoparticle is co-precipitation method. In this method produces a “mixed” precipitate comprising two or more insoluble species that are simultaneously removed from solution. Transition metal ferrite nanoparticles with a wide variety of compositions ranging from ternary metal oxides [2.42] (MFe_2O_4 where M^{2+}= Mn^{2+}, Fe^{2+}, Zn^{2+}, Co^{2+}, Cu^{2+}) to mixed metal oxides containing two [2.43] [$A_xB_{1-x}Fe_2O_4$, A^{2+} = Co^{2+}, B^{2+} = Zn^{2+}] or three [2.44] [$AxByC_{1-x-y}$ Fe_2O_4, A^{2+} = Co^{2+}, B^{2+} = Zn^{2+}, C^{2+} = Cu^{2+}] different divalent metal ions have been prepared by using the co-precipitation technique. Those metal ions are coming from mostly form the inorganic salt like chloride, nitrate and sulfate additionally as a precipitant NaOH, KOH, NH_3 are commonly used [2.45]. The solution is then subjected to PH adjustment or evaporation to force those salts to precipitate as hydroxides, hydrous oxides or oxalates. The crystal growth and their aggregation are influenced by the concentration of salt, temperature, the actual PH and the rate of PH change. The temperature is one of the most important parameters in the co-precipitation process. After precipitation, the solid mass is collected, washed and gradually dried by heating to the boiling point of the medium. The washing and drying procedures applied for co-precipitated hydroxides affect the degree of agglomeration in the final powder and must be considered when nanosized powders are the intended product.

A large number of reports are available on the synthesis of ultrafine oxide powders [2.46], oxide-oxide composites and biomaterial [2.47] by co precipitation reactions. There are several advantage of co-precipitation reactions. The advantages of co-precipitation reactions are (i) the temperature, (ii) the fine and uniform particle size with weakly agglomerated particles and (iii) the low cost. However, these reactions are highly susceptible to the reaction conditions and because of incomplete precipitation of the metal ions, control over the stoichiometry of the precursors is rather difficult to achieve. In addition, the co-precipitation reactions are not suited for certain oxides/hydroxides, for instance, in the case of amphoteric systems.

2.10.2 Sol-Gel Method

The sol-gel technology is a well-established colloidal chemistry technology, which offers possibilities to produce various materials with novel, predefined properties in a simple process and a relatively low process cost. Sol-gel process consist in the chemical transformation of liquid into a gel state and with a subsequent post treatment and transition into solid oxide materials. The reaction product of the sol–gel synthesis could be either colloidal powders or films. In addition to the sol–gel method precursor-based solution deposition routes can also be used for nanostructure formation. However, upon mixing with a liquid colloids appear bulky whereas the nanosized molecules always look clear. It involves the evolution of networks through the formation of colloidal suspension (sol) and gelatin to form a network in continuous liquid phase (gel). The precursor for synthesizing these colloids consists of ions of metal alkoxides and aloxysilanes. The most widely used are tetramethoxysilane (TMOS), and tetraethoxysilanes (TEOS) which form silica gels. Alkoxides are immiscible in water. They are organo metallic precursors for silica, aluminum, titanium, zirconium and many others. Mutual solvent alcohol is used. The sol gel process involves initially a homogeneous solution of one or more selected alkoxides. These are organic precursors for silica, alumina, titania, zirconia, among others. Mortia *et al* [2.48-2.49] A catalyst is used to start reaction and control pH.

There are two distinct reactions in the sol-gel process: hydrolysis of the alcohol groups and condensation of the resulting hydroxyl groups. For example, in the case of isomorphous γ-

AlOOH precursor, it exists as the un-hydrolyzed species $[Al(OH_2)_6]^{3+}$ below pH 3, and can be hydrolyzed extensively with increasing pH

$$[Al(OH_2)_6]^{3+} + kH_2O \rightarrow [Al(OH)_k(OH_2)_{6-k}]^{(3-k)+} + kH_3O^+$$

And

$$hH_3O^+ + kOH^- \rightarrow 2kH_2O$$

In the time of hydrolysis, water is added to replace the [OR] group with [OH-] group. The process of hydrolysis occurred by the reason of attracting of oxygen on silicon atoms in silica gel and this process can be accelerated by adding catalyst like HCl and NH_3. Hydrolysis continues until all alkoxy groups are replaced by hydroxyl groups. Subsequent condensation involving silanol group (Si-OH) produced siloxane bonds (Si-O-Si) and alcohol and water. Hydrolysis occurs by attack of oxygen contained in the water on the silicon atom.

The next step to hydrolysis is polymerization to form siloxane bond occurs by either a water producing or alcohol producing condensation reaction. The end result of condensation products is the formation of monomer, dimer, cyclic tetramer, and high order rings. The rate of hydrolysis is affected by pH, reagent concentration and H_2O/Si molar ratio (in case of silica gels). Also ageing and drying are important. By control of these factors, it is possible to vary the structure and properties of sol-gel derived inorganic networks. As the number of siloxane bonds increase, the molecules aggregate in the solution, where they form a network, a gel is formed upon drying. The water and alcohol are driven off and the network shrinks. At values of pH of greater then 7, and H_2O/Si value ranging from 7 to 5. Spherical nano-particles are formed. Polymerization to form siloxane bonds by either an alcohol producing or water producing

$$2OHSi(OR)_3 \rightarrow (OR)_3Si\ O\ Si(OR)_3 + H_2O$$

$$Or$$

$$2OHSi(OR)_3 \rightarrow (OR)_2OH\ Si\ O\ Si(OR)_3 + H_2O$$

Above pH of 7, Silica is more soluble and silica particles grow in size. Growth stops when the difference in solubility between the smallest and largest particles becomes indistinguishable. Larger particles are formed at higher temperatures. Zirconium and Yttrium gels can be similarly produced. Despite improvements in both chemical and physical methods of synthesis, there remain some problems and limitations. One of the advantages of this method is the ability to control the microstructure of final product by controlling chemical reaction parameters. This method is widely used in the synthesis of inorganic and organic-inorganic hybrid materials and capable of producing nanoparticles, nanorods, thin films and monoliths.

2.10.3 Sonochemical Synthesis

Currently, ultrasound irradiation has become an important tool in chemistry. High intensity ultrasound has found many important applications in organic synthesis, materials and organometallic chemistry, and industrial manufacturing processes. It provides an unusual mechanism for generating high-energy chemistry with extremely high local temperatures and pressures and an extraordinary heating and cooling rate. Sonochemistry originates from the extreme transient conditions induced by ultrasound, which produces unique hot spots that can achieve temperatures above 5000 K, pressures exceeding 1000 atmospheres, and heating and cooling rates in excess of 1010 Ks^{-1}[2.50]. These extreme conditions enable many chemical reactions to occur. In this method high temperature and high-pressure fields are produced at the centers of the bubbles, this bubbles collapse and generate localized hotspot through a shock wave formation within the gas phase of the collapsing bubbles. Many researcher showed that using this methods nanoparticle can be formed [2.51]. Ultra sound irradiation offer wide range particle size nanomaterials, but they are always of nanometer size.

2.10.4 Chemical Vapor Deposition and Chemical Vapor Condensation

Chemical Vapor Deposition (CVD) is widely used materials processing methods by which solid state thin film are coated, but it also use to produce high purity nanoparticle. There are several way the reaction can be achieved. In thermal CVD the reaction is activated by a high temperature which is more than 900^0C and the typical apparatus comprises of gas supply system, deposition chamber and an exhaust system. In plasma CVD, the reaction is activated by plasma at temperatures between 300 and 700°C. In laser CVD, pyrolysis occurs when laser thermal energy heats an absorbing substrate. In photo –

laser CVD, the chemical reaction is induced by ultra violet radiation which has sufficient photon energy, to break the chemical bond in the reactant molecules. In this process, the reaction is photon activated and deposition occurs at room temperature. Nano composite powders have been prepared by CVD. SiC/Si_3N composite powder was prepared using SiH_4, CH_4, WF_6 and H_2 as a source of gas at 1400°C.

Another process called chemical vapor condensation (CVC) was developed in Germany in 1994. It involves pyrolysis of vapors of metal organic precursors in a reduced pressure atmosphere. Particles of ZrO_2, Y_2O_3 and nanowhiskers have been produced by CVC method [2.52-2.53]. A metalorganic precursor is introduced in the hot zone of the reactor using mass flow controller. For instance, hexamethyldisilazane $(CH_3)_3$ Si NHSi $(CH_3)_3$ was used to produce SiCxNyOz powder by CVC. The reactor allows synthesis of mixtures of nanoparticles of two phases or doped nanoparticles by supplying two precursors at the front end of reactor and coated nanoparticles, $nZrO_2$, coated with $n\text{-}Al_2O_3$ by supplying a second precursor in a second stage of reactor.

2.10.5 Hydrothermal Method

Hydrothermal decomposition method is another types of important chemical method for nanoparticle synthesis. It involves the use of liquid-solid –solution reaction which lead an excellent control over the size and shape of the nanoparticle. This method constructed in two stage, one is crystal nucleation and other is subsequent growth. The desired particle size, shape and the surface is achieved by controlling the pressure, temperature, pH of the solution. The phenomena underlying the size and morphology control through tuning the process variables are the overall nucleation and growth rates, which depend on supersaturation [2.54]. For this method it is important to find the equilibrium condition of solution. Several methods have been developed to find this equilibrium position [2.55-2.57]. One of the famous methods is Helgeson-Kirkham-Flowers (HKF) model [2.58]. In this method, the solubility of hundred inorganic compound have been calculated over the wide range of conditions (25–1,000^{0}C, 0.1–500 MPa) based on the HKF model [2.59-2.60].

This synthetic technique involved the fabrication of magnetic metallic nanocrystals at different reactions conditions. The reaction strategy is based upon the phase separation which occurs at the interface of solid–liquid–solution phases present in the reaction. For instance Sun et al. Synthesized monodisperse of size 6, 10, and 12nm Fe_2O_4 and M Fe_2O_4 nanocrystal [2.61]. Wuwei and co-worker have synthesized oblique and truncated nano cubes of α- Fe_2O_3 by one step facile hydrothermal method. Hydrothermal and solvothermal methods can be combined with microwaves and magnetic fields for semicontinuous synthesis of materials having much improved reproducibility and high quality. Unsing the hydrothermal and solvothermal methods employed to prepare oxides; Group II–VI, III–V, and IV NPs; metal-organic frameworks (MOFs); and transitional-metal NPs composite can be prepared.

2.10.6 Microwave Synthesis

Microwave assisted method is a chemical method that use microwave radiation for heating materials containing electrical charges for instance polar molecule in the solvent or charge ion in the solid. As compared to the other heating methods microwave assisted solution fabrication methods have got more focus of research because of rapid processing, high reaction rate, reduce reaction time and high yield of product. The microwave irradiation has been used in the synthesis of inorganic nanoparticles and keeps showing rapid growth in its application to materials science. Compared with conventional heating methods, microwave assisted heating presents a more rapid and simultaneous environment for the formation of nanoparticles due to the fast and homogeneous heating effects of microwave irradiation. Therefore, microwave assisted heating method has the advantages of short reaction time, high energy efficiency and the ability to induce the formation of particles with small size, narrow size distribution and high purity. The interaction of dielectric materials, liquids or solids, with microwaves leads to what is generally known as dielectric heating. Electric dipoles present in such materials respond to the applied electric field. In liquids, constant reorientation leads to the friction between molecules, which subsequently generate heat. The microwave irradiation can be thermal and non-thermal. Microwave irradiation as a heating method has found a number of applications in chemistry. The frequency applied for the microwave heating in the range of 918 MHz to 2.45 GHz. The microwave ovens used in microwave chemistry range from simple household multimode ovens to large-scale batch as well as continuous multimode ovens.

In the past few years, microwave assisted heating has been applied in the soft chemical synthesis of various nanocrystalline metal chalcogenides and presents a promising trend in its future development [2.62]. Wang reported the synthesis of cubical spinal $M^{II}Fe_2O_4$ (M = Co, Mn, Ni) high crystalline structure in a short time of just 10 min by exposure the precursors to microwave radiation. Presently, Swaminathan *et al* and co-worker have reported the facile synthesis of NdFeb nanoparticles using microwave radiations. Liao *et al* (2001)[2.63] extended this methodology to the microwave assisted preparation of various metal sulfide nanoparticles including CdS, ZnS, CuS, HgS and Bi_2S_3 by choosing formaldehyde aqueous solution as solvent. Zhu *et al* (2002)[2.64] has successfully applied microwave irradiation, to induce the one-dimensional preferential growth of some II-VI and V-VI group semiconductors and prepared CdS nanoribbons by microwave-induced decomposition of single-source precursors.

2.10.7 Electrodeposition Method

This is a simple and well-established process and can be easily adopted to produce nanocrystalline materials. Electrodeposition of multilayered (1-D) metals can be achieved by using either two separate electrolytes or much more conveniently from one electrolyte by appropriate control of agitation and the electrical conditions (particularly voltage). Also, 3D nanostructure crystallites can be prepared using this method by utilizing the interference of one ion with the deposition of the other. The nucleation of nanostructures on the electrode substrate during electrodeposition is influenced by the crystal structure of the substrate, specific free surface energy, adhesion energy, lattice orientation of the electrode surface, and crystallographic lattice mismatch at the nucleus-substrate interface boundary [2.65]. The final size distribution of the electrodeposits, however, strongly depends on the kinetics of the nucleation and growth. These nuclei gradually grow and overlap, and therefore, the progressive nucleation process exhibits zones of reduced nucleation rate around the growing stable nuclei. The electrodeposition method consists of an electrochemical cell and accessories for applying controlled current at a certain voltage. The cell usually contains a reference electrode, a specially designed cathode, and an anode or counter electrode. The cathode substrate on which electrodeposition of the nanostructure takes place can be made of either nonmetallic or metallic materials. Using the surface of the cathode as a template, various desired nanostructures or morphologies can be synthesized for specific applications. Such a template-assisted electrodeposition process can be broadly divided into two groups: active template-assisted and restrictive template-based electrodeposition.

Recently many researchers extensively used this process to study the synthesis and properties of nanocrystalline materials [2.66-2.68]. It has been shown that electrodeposition yields grain sizes in the nanometer range when the electrodeposition variables (e.g., bath composition, pH, temperature, current density, etc.) are chosen such that nucleation of new grains are favoured rather than growth of existing grains. This is achieved by grains are favoured rather than growth of existing grains. This is achieved by addition of suitable surface-active elements to reduce surface diffusion of ad-atoms, etc. This technique can yield porosity-free finished products that do not require subsequent consolidation processing. Further, the process requires low initial capital investment and provides high production rates with few shape and size limitations.

2.11 Preparation of Nanocrystalline Ferrites by Biological Approach

The biological approach, also referred to as the biosynthesis, typically involves employing whole living organism for the synthesis of bionanoorganic materials. This approach of nanomaterials are synthesis are still largely in discovery phase, where a verity of nanomaterials are synthesized using different organisms such as fungi, bacteria, algae and plants which is reported by Thakkar *et al*. 2010 and Bansal *et al.* in 2011 and 2012. In recent years, the development of efficient green chemistry methods employing natural reducing, capping, and stabilizing agents to prepare silver nanoparticles with desired morphology and size have become a major focus of researchers. Biological methods can be used to synthesize silver nanoparticles without the use of any harsh, toxic and expensive chemical substances [2.69-2.70]. The bioreduction of metal ions by combinations of biomolecules found in the extracts of certain organisms (e.g., enzymes/proteins, amino acids, polysaccharides, and vitamins) is environmentally benign, yet chemically complex. Many studies have reported successful synthesis of silver nanoparticle using organisms [2.71-2.71].

MATERIALS PROCESSING AND THEORY OF EXPERIMENTATION

3.1 Synthesis of $Co_{0.5}Zn_{0.5}Fe_2O_4$ nanoparticles

A lots of synthesis strategies for preparing nanosized Co-Zn ferrite MNPs but chemical co-precipitation method is prominent one. Because, this method can be greatly varies depending on pH, salt concentration, temperature, stirring speed etc. to synthesis expected properties of nanomaterial. The advantage of this methods over others is that the control of production of ferrite particle, its size distribution is relatively easy and there is no need of extra mechanical or subsequent step.

The sample $Co_{0.5}Zn_{0.5}Fe_2O_4$ have been prepared by co-precipitation methods from aqueous solution of cobalt chloride hexahydrated ($CoCl_2 . 6H_2O$), Zinc Chloride dihydeated ($ZnCl_2 . 2H_2O$) and ferric chloride hexahydrated ($FeCl_3 . 6H_2O$) and all of those materials were of analytical grade. 8M NaOH solution was also prepared in another beaker. At first those materials were weighted according to the molar ratio and then making a solution using distilled water. Taking all of the materials in a beaker and placed in a magnetic starrier. NaOH was added drop wise in the beaker and the speed of the magnetic stirrer was gradually increased until precipitation completed. NaOH was added to control the pH of the solution. Using a pH meter the pH of the solution was kept constant at 13.5. The stirring process stopped and the sample was left to settle down the precipitates for one an hour. The particles were settled down at the bottom of the beakers. In this final product enormous amount of NaOH present which should be washed away from the final product. After cooling to the room temperature the particles were separated by subsequent using centrifugation and washed with distilled. The solution was centrifuged at 13000 rpm for 20 munities for 10 times. After removal of NaOH from the mixture was subjected to be a heat treatment at 353K for 72 hours. This solid phase is form via a chemical process involving the formation of an intermediate phase, to remove this the sample was milled by hand milling for 3 hours and preserved this powder sample in vial and made pallet size sample for annealing at various temperature.

3.1.1 Synthesis Route of $Co_{0.5}Zn_{0.5}Fe_2O_4$

The MNPs of $Co_{0.5}Zn_{0.5}Fe_2O_4$ are prepared by co-participation method from the mixture of the solution of $CoCl_2$. $6H_2O$, $ZnCl_2$. $2H_2O$, and $FeCl_2$. $6H_2O$. NaOH was used as a co-precipitant agent to control the pH level of the solution. All those chemical were lab grated. The synthesis of $Co_{0.5}Zn_{0.5}Fe_2O_4$ MNPs involving two steps: The preparation of nano-sized magnetic particles and the stabilization of the nanoparticles. The reaction for the ions Fe^{2+}, Zn^{2+} and Co^{2+} given the final product of $Co_{0.5}Zn_{0.5}Fe_2O_4$ nanoparticles. The reaction takes placed in several steps which is given below:

$$0.5Cocl_2.\ 6H_2O + NaOH = 0.5\ Co(OH)_2 + NaOH + 3\ H_2O$$

and

$$0.5\ ZnCl_2.2H_2O + NaOH = 0.5Zn(OH)_2 + NaOH + H_2O$$

and

$$2\ FeCl_3.\ 6H_2O + 6\ NaOH = 2\ Fe(OH)_3 + 6Nacl + 12\ H_2O$$

and

$$0.5Cocl_2.6H_2O + 0.5\ ZnCl_2.2H_2O + 2\ FeCl_3.\ 6H_2O = Co_{0.5}Zn_{0.5}Fe_2O_4 + 4\ H_2O$$

The final reaction could be write as

$$0.5Cocl_2.\ 6H_2O + 0.5\ ZnCl_2.\ 2H_2O + 2\ FeCl_3.\ 6H_2O + 8\ NaOH =$$

$$Co_{0.5}Zn_{0.5}Fe_2O_4 + 8NaCl + 20\ H_2O$$

1M $Co_{0.5}Zn_{0.5}Fe_2O_4$, 8M NaCl and approximate 20M H_2O were produced in the final product. The final product contained NaCl, which should be removed. As NaCl is a metallic salt which completely dissolved in distilled water. This NaCl of the final product was removed by subsequent washing and centrifuged of the sample with distilled water. To wash out NaCl from the solution, the solution was centrifuged by centrifuge rotor. The rotor speed was 1350 rpm and the time length was 20 minutes. This operation was continued for 10 times.

Figure 3.1 summarized the experimental procedure to synthesized $Co_{0.5}Zn_{0.5}Fe_2O_4$ nanoparticles:

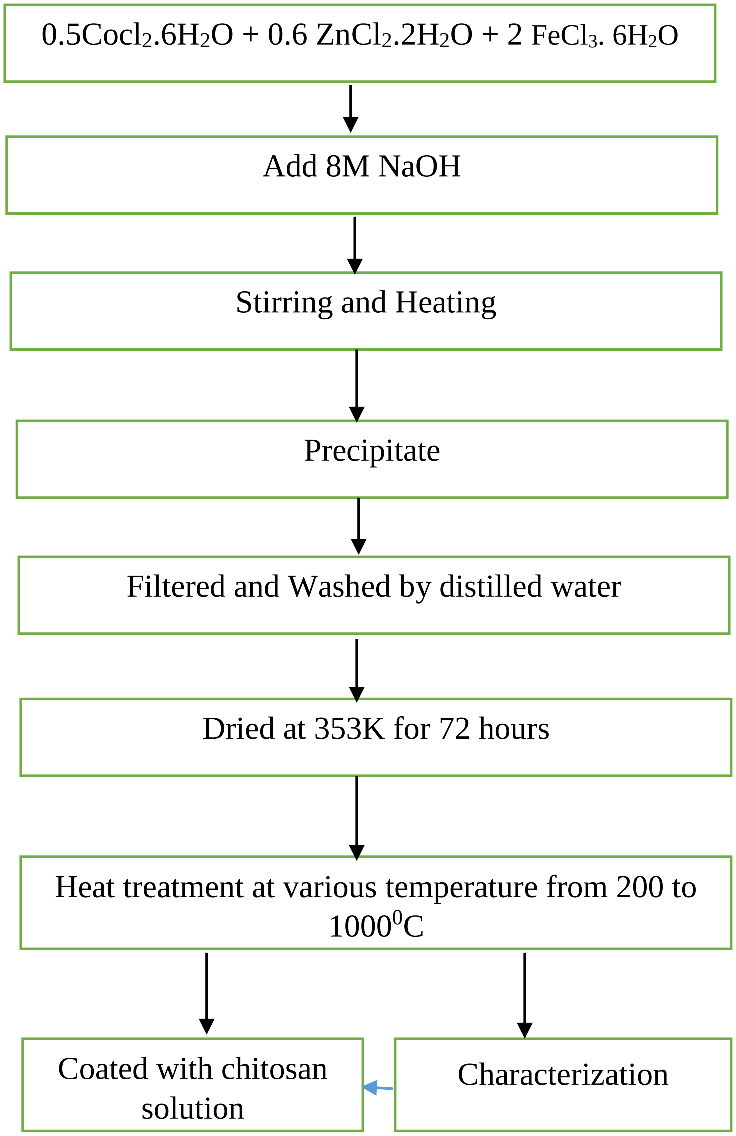

Figure 3.1: Flow chart of $Co_{0.5}Zn_{0.5}Fe_2O_4$ nanoparticles synthesis by chemical co- precipitation method

3.1.2 Method of Coating of $Co_{0.5}Zn_{0.5}Fe_2O_4$ by Chitosan

Chitosan is a partially acetylated glucosamine biopolymer with many useful features such as hydrophilicity, biocompatibility and biodegradability. In addition, the amino group on the chitosan can also be used for further functionalization with specific component, such as various drugs, specific binding sites on the functional groups [3.1-3.3]

Interest in the use of chitosan for medical and pharmaceutica applications has been growing, especially because of its remarkable properties such as biocompatibility, which makes it suitable for several medical applications [3.4]. Until a few years ago, chitosan was used mainly to remove sediments and metallic ions from water, as well as in the food industry. Currently, chitosan is used in the production of cosmetics, medicines, food additives, and semi-permeable membranes, and in the development of biomaterials for medical and dental applications.

The main constituent of chitosan is chitin. Chitin is a cellulose-like biopolymer found mainly in the exoskeleton of marine animals such as shrimp, crabs, or lobsters. Chitin can also be found in mushrooms and yeasts. Chitosan is a chemically processed form of chitin. “Squid pens,” waste shell by-products of squid processing, are a renewable and inexpensive source of chitosan. The chemical structure of chitosan as shown in figure 3.2:

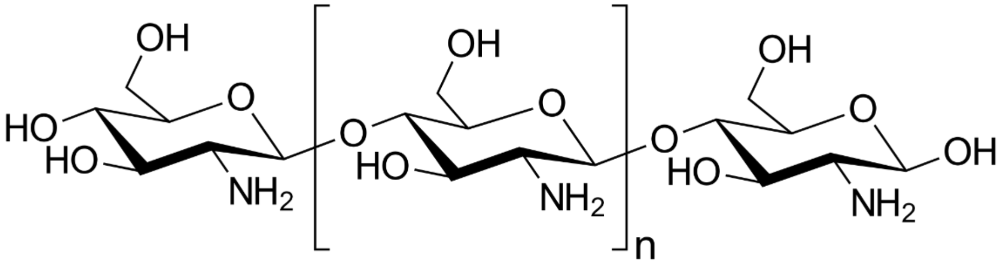

Figure 3.2: chemical structure of chitosan

Co-Zn ferrite MNPs could be controlled by adjusting concentration of chitosan, sonication time, and reaction temperature during the coating time. The effects of the above mentioned phenomenon on the synthesized chitosan bound MNPs were investigated using DLS measurement. The cobalt zinc ferrite were coated by chitosan. The nanoparticle were remained suspended homogeneously in the solution. As the nanoparticles are magnetic in nature, they tried to agglomerate but each nanoparticles are coated with a surfactant which have a Van der Waals force greater than the attraction of the nanoparticles. This Van der Waals force prevent nanoparticles from agglomeration. The 1% w/v chitosan solution was prepared as 0.4g chitosan was poured into 40ml water and 3ml acetic acid. 40mg dried sample was taken in a falcon tube with 2ml chitosan solution. This mixture of solution was vortexed for 30 minutes. After that this sample was sonigeted in a ultra sound bath for long time. This process was repeated for the sample annealed at 200^0C, 400^0C, 600^0C, 800^0C and as-dried sample. After that using distilled water 1mg/ml, 2mg/ml, 4mg/ml and 6mg/ml sample were prepared for each annealing temperature.

3.2 X-Ray Diffraction

X-ray diffraction (XRD) **[3.5-3.6]** is the most precise technique for studying the crystal structure of solids, generally requiring no elaborate sample preparation and is essentially non-destructive. A crystal lattice is regularly arranged 3D distribution of atoms in space. They are arranged in such a way that they form a series of parallel plane separated from one other by a distanced which varies according to the materials.

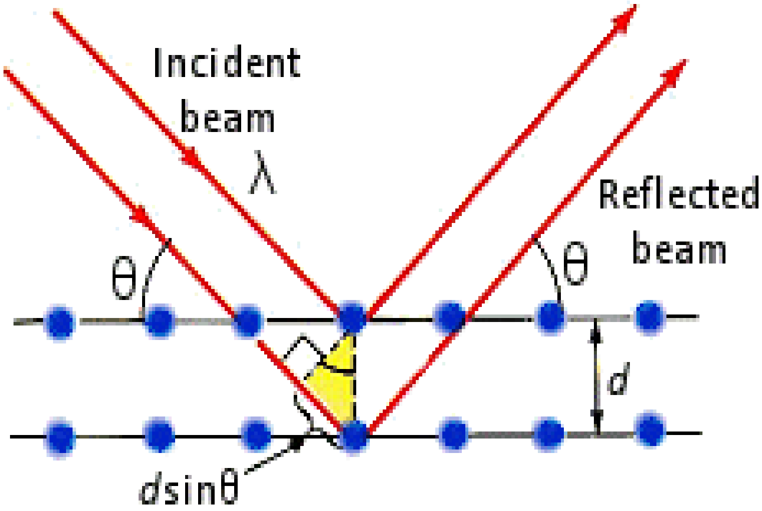

Figure 3.3: Schematic diagram of Bragg's diffraction pattern

The term structure encloses a variety of concepts, which describe on various scales, the arrangement of the building blocks of materials. On an atomic scale, one deals with the crystal structure, which is defined by the crystallographic data of the unit cell. These data contain the shape and dimensions of the unit cell and the atomic position within its Bravias structure. They are obtained by diffraction experiments. On a coaster scale, one deals with the microscopic observations of the microstructure, which characterizes the size, shapes and mutual arrangements of individual crystal grains. It also includes the morphology of the surface of the materials. Microstructure and surface morphology observation of coatings, which are too thick for direct transmission also depend heavily on the high resolving power of electron microscopy. Suitable technique is surface replication and scanning electron microscopy **[3.7-3.8]**. Frequently one has to determine whether a given deposit is a single crystal or polycrystalline either with a random distribution of orientation with respect to the coating plane. For a single crystal coating, it is important to know its orientation relationship with respect to the substrate **[3.9]**. XRD is a suitable tool to determine the crystal structure of any unknown materials, whether the sample is a single crystal or poly crystals **[3.10]** , either with a random distribution of orientations or with a preferred orientation with respect to the sample. The peaks in an XRD pattern are directly related to the atomic distance. Let us consider an incident X-ray beam interacting with the atoms arranged in a periodic manner as shown in 2D in figure 3.3. The atoms represented as sphere in illustration, can be viewed as forming different set of planes with an inter-plane distance of d, the condition for the diffraction to occur can be written as

$$2dSin\theta = n\lambda \tag{3.1}$$

This is known as Bragg's law. Where n is the order of diffraction, λ is the wavelength of the x-rays, d is the distance between two neighboring planes, θ is the angle between the incident x-ray and the crystalline plane (in radians).

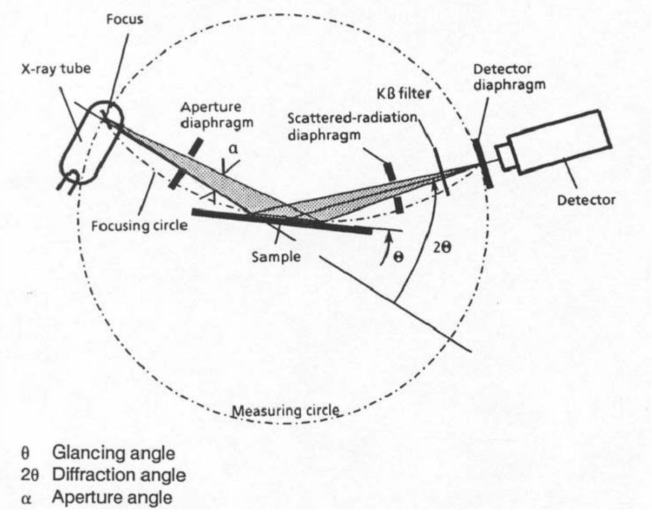

Figure 3.4: Schematic of the X-ray powder diffractometer.

The X-ray source provides a polychromatic radiation produced from a copper target source. The monochromator positioned in front of the detector is tuned to select only the Cu-Kα emission line from the source. The system can then be viewed as operating with a monochromatic source whose wavelength is 1.5406A^o. The sample is rotated around an axis. As the scanning proceeds, the detector is rotated around the same axis to detect the diffracted beam is shown in Figure. 3.4. The instrument is fully computer controlled. The x-rays detected from the sample surface have been diffracted by families of planes, according to Bragg's law. The result of XRD measurements is a diffractogram, which is a plot of the intensity (number of counts) versus the angle. The different phases in the crystal (from peak positions), phase concentrations (from peak heights), crystallite sizes (from peak widths) and amorphous content (from background hump) can be deduced from a diffractogram.

The X-ray diffraction (XRD) method was used to investigate the structural properties of the $Co_{0.5}Zn_{0.5}Fe_2O_4$ sample at BCSIR. The diffraction pattern was recorded using a Bruker XRD system shown in Figure 3.5 with Cu-Kα radiation using the wavelength of 1.5406 Å, operated at 60 kV and 55 mA, with high temperature attachment up to 1600℃, with the scanning angular range $10° \leq 2\theta \leq 90°$ to get possible fundamental peaks for each sample **[3.11]**. The XRD machine was totally computer controlled and all the data were stored in the hard disk memory of the computer for further analysis.

Figure 3.5: Experimental set up of Bruker XRD system.

3.2.1 Interpretation of the XRD data from Bragg's law

In 1912, Max von Laue, a German physicist, discovered that X-rays could be diffracted, or scattered, in an orderly way by the orderly array of atoms in a crystal. That is, crystals can be used as three-dimensional ‘diffraction gratings’ for X-rays. The phenomenon of X-ray diffraction from crystals is used both to analyze X-rays of unknown wavelength using a crystal whose atomic structure is known, and to determine, using X-rays of known wavelength, the atomic structure of crystals. One method of interpreting XRD is the Bragg formulation. The X-ray waves are considered as being reflected by sheets of atoms in the crystal. When a beam of monochromatic (uniform wavelength) X-rays strikes a crystal, the wavelets scattered by the atoms in each sheet combine to form a reflected wave. If the path difference for waves reflected by successive sheets is a whole number of wavelengths, the wave trains will combine to produce a strong reflected beam.

The XRD data containing of θ_{hkl} and d_{hkl} values corresponding to the different crystallographic planes are used to determine the structural information of the samples like lattice parameter and constituent phase. Lattice parameter of Cu-Zn ferrite sample were determined by the Debye- Scherrer methods after extrapolating of the curve. We determine lattice special d_{hkl} using the Bragg’s reflection from the equation

$$2d_{hkl}Sin\theta = n\lambda$$

ie

$$d_{hkl} = \frac{n\lambda}{2Sin\theta} \qquad (3.2)$$

Where n is an integer and λ is the X-ray wavelength. The equation for reflection (Bragg condition) can be satisfied for any set of planes whose spacing is greater than half the wavelength of the X-rays used (if $d < \lambda/2$, then $\sin\theta > 1$, which is impossible). This condition sets a limit on how many orders of diffracted waves can be obtained from a given crystal using a x-ray beam of a given wavelength.

Since the crystal pattern repeats in three dimensions, forming a three-dimensional diffraction grating, three integers, denoted h, k, l are required to describe the order of the diffracted waves. These three integers, the Miller indices used in crystallography, denote the orientation of the reflecting sheets with respect to the unit cell and the path difference in units of wavelength between identical reflecting sheets. So the separation between two planes is given by

$$d_{hkl} = \frac{a}{\sqrt{h^2 + k^2 + l^2}} \tag{3.3}$$

Where a is the lattice parameter, which can be expressed as

$$a = d_{hkl}\sqrt{h^2 + k^2 + l^2} \tag{3.4}$$

Determining the exact lattice parameter for each sample, through the Nelson-Riley extrapolation method. The values of lattice parameter obtained from each plane are plotted against Nelson-Riley function [3.12]. The Nelson-Riley function is given by

$$F(\theta) = \frac{1}{2}\left[\frac{\cos^2\theta}{\sin\theta} + \frac{\cos^2\theta}{\theta}\right] \tag{3.5}$$

Where θ is the Bragg's angle. Now drawing the graph of 'a' vs. F(θ) and using linear fitting of those points will give us the lattice parameter 'a_0'. This value of 'a_0' at F(θ) = 0 or θ = 90° .These 'a_0's are calculated with an error estimated to be ± 0.0001Å.

3.2.2 Determination of Nanometric Grain Size using Scherrer's formula

The crystal size of the nanoparticle can be determine by using Scherrer's formula. Consider a set of N planes spaced 'a' apart. First we will derive the structural factor for this case, and then determine an expression for the peak width.

This system, effectively, a one dimensional perfect crystal, has a structural factor or scattering factor S(q)

$$S(q) = \frac{1}{N}\sum_{j,k=1}^{N} e^{-iq(x_j - x_k)} \tag{3.6}$$

Where for N planes $x_j=a_j$ so,

$$S(q) = \frac{1}{N}\sum_{k=1}^{N} e^{-iqak} \times \sum_{j=1}^{N} e^{-iqaj} \tag{3.7}$$

This sum are the simple geometric series. Then

$$S(q) = \frac{1}{N}\frac{[e^{-iqa} - e^{-iqa(N+1)}]}{[1 - e^{-iqa}]} \times \frac{[e^{iqa} - e^{iqa(N+1)}]}{[1 - e^{iqa}]} \qquad (3.8)$$

Nanoparticles are basically crystalline and because their crystallinity exhibit Bragg scattering peak in XRD experiment

$$S(q) = \frac{1}{N}\frac{2 - e^{iqaN} - e^{-iqaN}}{2 - e^{iqa} - e^{-iqa}} \qquad (3.9)$$

Converting to trigonometric function

$$S(q) = \frac{1}{N}\frac{1 - \cos(Nqa)}{1 - \cos(qa)} \qquad (3.10)$$

And finally

$$S(q) = \frac{1}{N}\frac{Sin^2(\frac{Nqa}{2})}{Sin^2(\frac{qa}{2})} \qquad (3.11)$$

Which gives a set of peaks at $q_p = 0, 2\pi/a\ldots\ldots$, all with height $S(q_p) = N$

From the definition of the FWHM, for a peak at q_p and a FWHM of Δq, $S(q_p \pm \Delta q) = \frac{S(\mathrm{qp})}{2} = \frac{N}{2}$. So we can write

$$S(\mathrm{qp} \pm \Delta\mathrm{q}) = \frac{1}{N}\frac{Sin^2[\frac{Na\left(\mathrm{qp} + \frac{\Delta\mathrm{q}}{2}\right)}{2}]}{Sin^2[\frac{a\left(\mathrm{qp} + \frac{\Delta\mathrm{q}}{2}\right)}{2}]} = \frac{N}{2} \qquad (3.12)$$

And

$$\frac{Sin[\frac{Na\left(\mathrm{qp} + \frac{\Delta\mathrm{q}}{2}\right)}{2}]}{Sin[\frac{a\left(\mathrm{qp} + \frac{\Delta\mathrm{q}}{2}\right)}{2}]} = \frac{Sin[\frac{Na\Delta\mathrm{q}}{4}]}{Sin[\frac{a\Delta\mathrm{q}}{4}]} = \frac{N}{2^{\frac{1}{2}}} \qquad (3.13)$$

As Δq is small for not too small N, then $Sin\left[\frac{a\Delta\mathrm{q}}{4}\right] = \frac{\Delta\mathrm{qa}}{2}$ and we can write the equation is a single non-linear equation$Sinx - \frac{x}{2^{\frac{1}{2}}} = 0$, for $x = \frac{Na\Delta\mathrm{q}}{4}$. The solution to the equation is x = 1.39. Therefore, the size of the set of planes is related to the FWHM by

$$D_g = Na = \frac{5.56}{\Delta q} \tag{3.14}$$

To convert to the equation to an expression for the crystal size in terms of peak width in the scattering angle 2θ used an X-ray powder diffraction, we note that the scattering vector, $q = \frac{4\pi}{\lambda} Sin\theta$. Then the peak width in the variable 2θ is approximately

$$\beta = \frac{2\Delta q}{\frac{dq}{d\theta}} = \frac{2\Delta q}{\frac{4\pi}{\lambda} Cos\theta} \tag{3.15}$$

So,

$$D_g = Na = \frac{5.56\lambda}{2\pi\beta Cos\theta} = \frac{0.88\lambda}{\beta Cos\theta} \tag{3.16}$$

Which is known as the Scherrer's formula. This formula can only be applicable for the nanoensemble. Particle size of the prepared $Co_{0.5}Zn_{0.5}Fe_2O_4$ nanoparticles was determined from the strongest peak of each XRD patterns using Scherrer equation (3.16), where D_g is the average particle size, λ is the wavelength of the radiation used as the primary beam of Cu-K_α (λ = 1.54178 Å), θ is the angle of incidence in degree and β is the full width at half maximum (FWHM) of the strongest reflection (311) in radian. At (311) reflection's position of the peak, the value of instrumental broadening was found to be 0.06^o.

3.3 Theory of Working of Vibrating Sample Magnetometer (VSM)

The principle of VSM is the measurement of electromotive force induces by magnetic sample when it is vibrate at a constant frequency in the presence of a static and uniform magnetic field. The VSM was first designed by Simon Foner, in 1959 at the Lincoln laboratories. [3.13]. since then many transformations and variants have been seen [3.14], but the basic underlying principle remains the same- induction of emf by Faraday's law. All the VSM work, involves the measurement of voltage induced in a stationary coil, otherwise called as detection coils, due to the harmonic vibration of the sample in a uniform magnetic field. It is thus the detection coil geometry and configuration which decides the sensitivity of measurement.

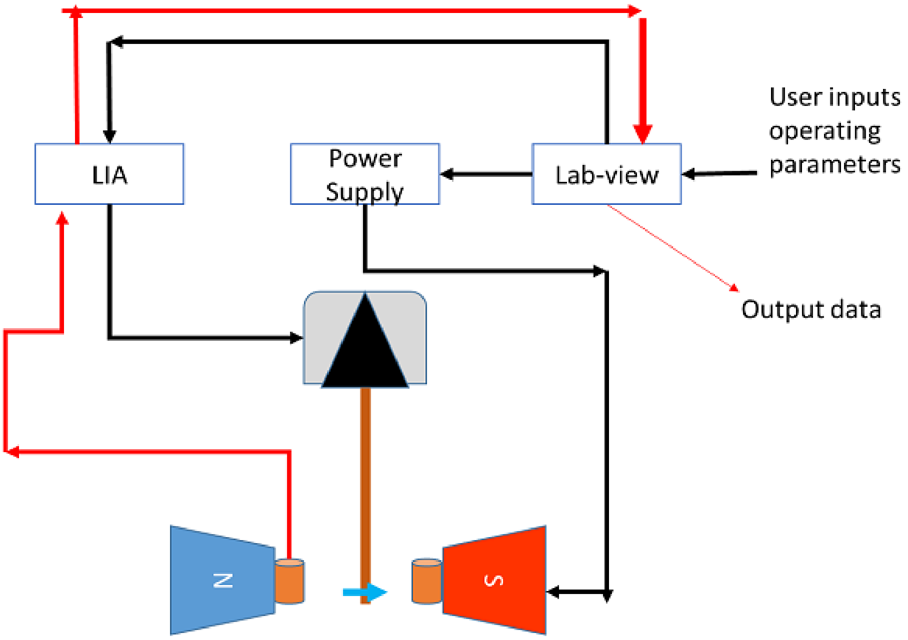

Figure 3.6: Measurement flow scheme

By employing electromagnetism principles, the induced voltage in the detection coil can be calculated. Suppose due to vibration of the sample, a flux φ is picked up by the detection coil. So,

$$\emptyset = \mu\mu_o H \tag{3.17}$$

Where$\mu_o = 4\pi \times 10^{-7}$, μ = Point dipole and H is the magnetic field. Due to the vibration, the flux linked to the coil changes and a voltage is induced.

$$V(t) = -N\frac{\partial\emptyset(t)}{\partial t} \tag{3.18}$$

Here N = number of turns in the detection coil. Or,

$$V(t) = -N\mu_o[\left(\frac{\partial H_x}{\partial x}\frac{\partial x}{\partial t} + \frac{\partial H_x}{\partial y}\frac{\partial y}{\partial t} + \frac{\partial H_x}{\partial z}\frac{\partial z}{\partial t}\right)\mu_x + \left(\frac{\partial H_y}{\partial x}\frac{\partial x}{\partial t} + \right. \\ \left. \frac{\partial H_y}{\partial y}\frac{\partial y}{\partial t} + \frac{\partial H_y}{\partial z}\frac{\partial z}{\partial t}\right)\mu_y + \left(\frac{\partial H_z}{\partial x}\frac{\partial x}{\partial t} + \frac{\partial H_z}{\partial y}\frac{\partial y}{\partial t} + \frac{\partial H_z}{\partial z}\frac{\partial z}{\partial t}\right)\mu_z] \tag{3.19}$$

From this it can be deduced that the induced voltage depends on: (1) Number of turns and (2) gradient of H. If the vibration is harmonic in Z axis

$$Z(t) = Z_0 Sin(\frac{vt}{Z_0}) \tag{3.20}$$

So,

$$Z(t) = -N\mu_0 v(\frac{\delta H_x}{\delta z}\mu_x + \frac{\delta H_y}{\delta z}\mu_y + \frac{\delta H_z}{\delta z}\mu_z) \times Cos(\frac{vt}{Z_0}) \tag{3.21}$$

Here, Z_0 = vibration amplitude, υ = velocity of the moving sample. As per the analysis of A. Zieba, for a coil carrying current,

$$B.\mu = I\emptyset \tag{3.22}$$

$$V(t) = \frac{\partial\emptyset(t)}{\partial t} = grad\left(\frac{H(r)\mu}{I}\right).v(t) \tag{3.23}$$

Or, $V(t) = \mu G(r)v(t)$ (3.24)

The scalar $G(r) = \frac{d}{dx}\left(\frac{H(r)\mu}{I}\right)$ is called the sensitivity function, and represents the derivative along the direction of the sample motion, which was summarized by Pattnaik *et al.* Therefore if the amplitude and frequency of the vibration is known, along with the sensitivity constant, the voltage induced in the detection coil is proportional to the magnetic moment and hence magnetization of sample. The different constituent parts of the VSM are the vibrating system, Lock-In amplifier, Electromagnet and power supply, Pick up coil or Detection coil, Sample, Temperature variation system. This above calculation was done by Pattnaik *et al*

Figure 3.6 shows VSM of Model EV7 system. The magnetic properties measurement system model EV7 is a sophisticated analytical instrument configured specially for the study of the magnetic properties of the small samples over a broad range of temperature from 103K to 800K and magnetic field from -20kOe to +20kOe. The VSM is designed to continuously measure the magnetic properties of materials as a function of temperature and the field. In this type of magnetometer, the sample is vibrated up and down in a region surrounded by several pick up coils. The magnetic sample is thus acting as a time-changing magnetic flux, varying the electric flux is accompanied by an electric field and the field induces a voltage in pick up coils. This alternating voltage signal is processed by a control unit system, in order to increase the signal to noise ratio. The result is a measure of the magnetization of the sample.

Figure: 3.7: Vibrating Sample Magnetometer at Materials Science Division, AECD

3.4 Mössbauer Spectroscopy

Fifty years ago Rudolf L. Mössbauer discovered the recoilless nuclear resonance absorption of γ-rays while working on his doctoral thesis. This phenomenon, which rapidly developed into a new spectroscopic technique is known as Mössbauer effect [3.15-3.16]. Over the last couple of decades, Mössbauer spectroscopy has become one of the most captivating tools in chemical physics providing information about the chemical environment of the resonating nucleus on an atomic scale [3.15-3.16]. The most well-known application is the determination of iron ^{57}Fe in crystalline and in disordered solid samples. Besides iron, there are many elements in the periodic table which have Mössbauer active nuclei [3.17-3.18]. The Mössbauer effect has been observed for the elements which are dotted in the periodic table shown the phenomenon of recoilless resonance absorption/emission of γ-rays by nuclei is the basic characteristic of Mössbauer Spectoscopy [3.19]. The information of the local magnetic and electronic environment of Mössbauer nuclei (i.e. ^{57}Fe or ^{119}Sn) in a sample can be get from the Mössbauer effect. This technique has no effect of external magnetic field as in this technique there is no need external magnetic field.

Mössbauer spectroscopy has also been used to determine the average direction of magnetization by using the well-known fact that for the ^{57}Fe, The intensity of the six lines of the hyperfine spectra have an area ratio 3: Z: 1:1: Z: 3, Where $Z = \frac{4}{1+\cot^2\theta}$, θ being the angle between the direction of magnetic field at the nucleus and the direction of γ-ray emission [3.20]. In ^{57}Fe the strength of this magnetic field is H=33T [3.21] at room temperature. The value Z varies from 0 for the axis magnetization in the sample phase to 4 for the axis of magnetization in sample plane.

By using Mössbauer spectroscopy the resonant energy of the γ-rays absorption could be determine precisely. So for that, it is easy to detect the small change in energy of the hyperfine interactions between the nucleus and surrounding. The change in number, shape, position and relative force of the different ingestion lines are the main determining parts of change in Mössbauer spectrum. This change most often archived by the oscillating a radioactive source in a very small velocity ie. mm/sec, and recording the spectrum in discrete velocity steps. The energy scale of a Mössbauer spectrum in terms of the source velocity is shown in figure 3.7.

A Mössbauer spectrum, which is a plot of the relative transmission of the γ radiation as a function of the Doppler velocity, reflects the nature and strength of the hyperfine interactions between the Mössbauer nucleus and the surrounding electrons. The Mössbauer effect makes it possible to resolve the hyperfine interactions and provide information on the electronic structure.

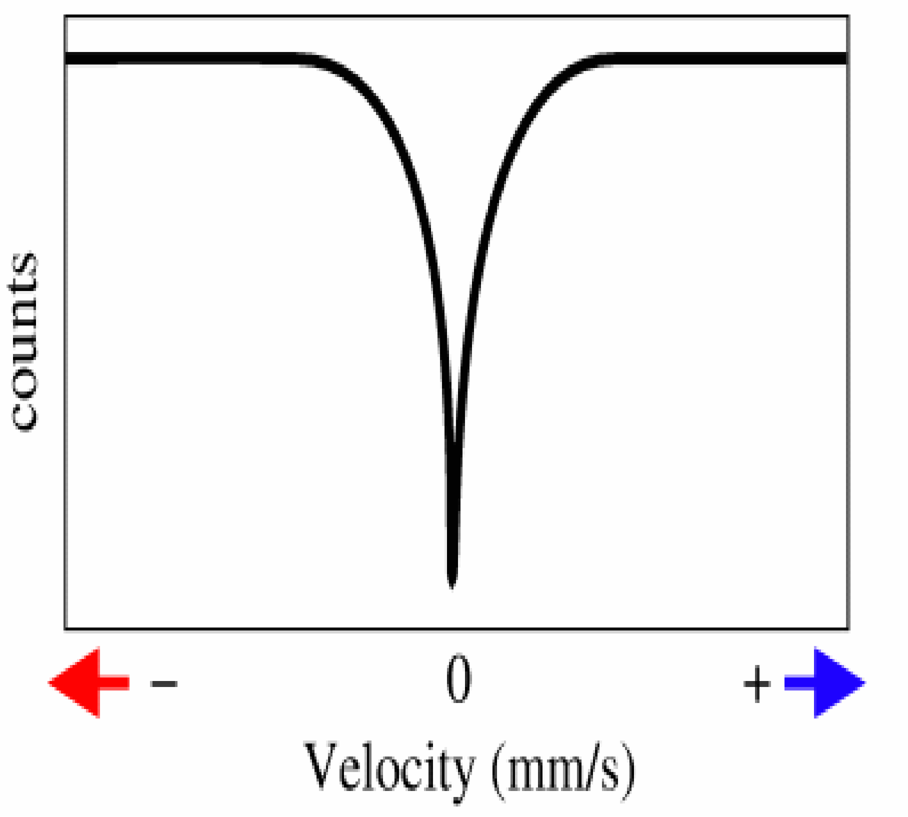

Figure 3.8: Specttrum counts Vs source velocity curve.

The three main hyperfine interactions corresponding to the nuclear moments are:

(i) Isomer Shift
(ii) Quadrupole Splitting
(iii) Magnetic Hyperfine Splitting

3.4.1. Isomer Shift

An isomeric shift (IS) occurs when non identical atoms play the role of source and absorber, thus the radius of the source is different that of the absorber, and the same holds that the electron density of each species is different. When the change in the Coulomb interaction between nuclear and electronic charge the IS arisen. In that time the volume of ^{57}Fe increase slightly to the $I = \frac{3}{2}$ state. The IS depends directly on the s-electron and can be influenced by the shielding p, d, f electron. In a Mössbauer experiment one measures the change of the energy of the resonance γ quantum between the source (s) and the absorber (a) nuclei, thus there appears a dependence of the energy of resonance γ quantum on the electronic environment in which the given nucleus is immersed. The IS, δ measured in terms of the Doppler velocity necessary to achieve resonance is given in equation (3.25)

$$\delta = \frac{c}{E_\gamma}(\Delta E_\gamma^a - \Delta E_\gamma^s) \qquad (3.25)$$

Where c is the velocity of light and Eγ is the energy of the γ quantum. Figure 3.8 represent the hyperfine splitting scheme for 57Fe Mössbauer spectra.

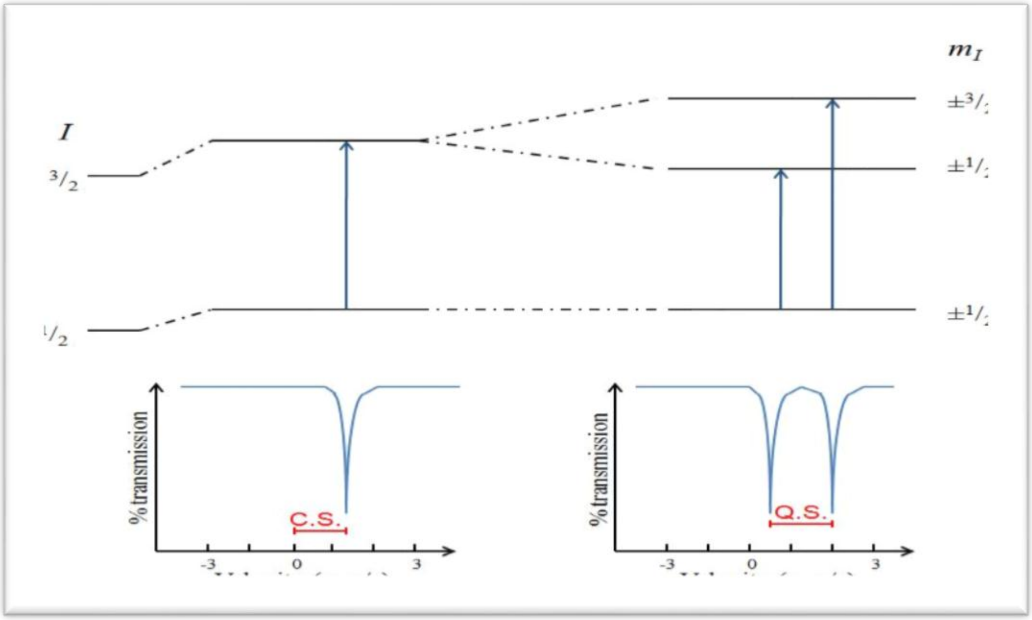

Figure 3.9: The isomer Shift and Quadrupole Splitting of the nuclear energy levels and corresponding Mössbauer spectra.

This shift appears in the spectrum as the difference between the position of the baricenter of the resonance signal and zero Doppler velocity as shown in figure 3.8 [3.22-3.24]. Traditionally, the energy differences $\Delta E_\gamma^{a/s}$ are calculated within the framework of perturbation theory, whereby the variation of the electron-nuclear interaction potential during the γ-transition is treated as a weak perturbation of the nuclear energy levels [3.25-3.26]. This approach leads to the well-known expression for the isomer shift of Mössbauer spectra as a linear function of the so-called contact electron density (electron density at the nucleus) in the absorber $\bar{\rho}_e^a$ and source $\bar{\rho}_e^s$ compounds, see equation. (3.26)

$$\delta = \alpha(\bar{\rho}_e^a - \bar{\rho}_e^s) \tag{3.26}$$

Where α is a calibration constant, which depends on the parameters of the nuclear γ-transition. The most valuable information derived from isomer shift data refers to the oxidation state and spin state of a Mössbauer-active atom, its bond properties *etc*.

The IS arises from the fact that aa nucleus has a finite volume and S-electrons spend a fraction of their time inside the nuclear region. The nuclear charge thus interacts electro statically with the S-electron charge. As a result of this interaction the nuclear energy levels get shifted by a small amount, the shift depends upon the chemical environment. Although, we cannot measure change directly, it is possible to compare values by mean of a suitable reference which can be either the γ-ray source or another standard absorber. The observed range of IS is within an order of magnitude of the natural line width of the transition i.e, 10^{-8} to 10^{-9} ev. Isomer shifts provides important information concerning the nature of the chemical bond because the outer electrons (valence electrons) would be must effected by changes chemical surrounding and consequently the changes in the outer S-electrons densities would contributed.

3.4.2 Quadrupole Splitting

Quadrupole splitting in the Mössbauer spectrum occurs when a nucleus with an electric quadrupole moment experiences a non-uniform electric field. Nuclei in states with an angular momentum quantum number $I>1/2$ have a non-spherical charge distribution. This produces a nuclear quadrupole moment. In the presence of an asymmetrical electric field (produced by an asymmetric electronic charge distribution or ligand arrangement) this splits the nuclear energy levels. The charge distribution is characterised by a single quantity called the Electric Field Gradient (EFG) [3.27-3.28].

The magnitude of the quadrupole moment may change in going from one state of excitation to another. The sign of the electric quadrupole moment, Q indicates the shape of the deformation. Q is negative for a flattened (pancake-shaped) nucleus and positive for an elongated nucleus (cigar-shaped). Q is constant for a given Mössbauer nucleus, ie, changes in the quadrupole interaction energy observed in different compounds of a given Mössbauer nucleide under constant experimental conditions can only arise from the changes in the electric field gradient (EFG) generated by the surrounding electrons and other nuclei. Therefore, the interpretation of quadrupole splittings requires the knowledge of the EFG. The interaction between the electric quadrupole moment of the nucleus and EFG at the nuclear position give rise to a splitting in the nuclear energy levels into substates which are characterized by the absolute magnitude of the nuclear magnetic spin quantum number $|m_I|$.

As the Mössbauer spectroscopy involves the absorption of the γ -rays to promote a nucleus from the ground state to an excited state, the quadrupole Hamiltonian has to be solved for each energy level if both levels have nuclear spin greater than 1/2. For ^{57}Fe, the ground state has nuclear spin I = 1/2 and the lowest excited state has I = 3/2. The second part of figure 3.9 shows the quadrupole splitting of the nuclear energy levels of ^{57}Fe, where the absoption line is split due to the interaction of the nuclear quadrupole moment with non-zero EFG at the nucleus. The separation between the lines, ΔE_Q, is known as the quadrupole splitting and is written as,

$$\Delta E_Q = \frac{1}{2} qQV_{zz}((1+\eta^2)/3)^{\frac{1}{2}} \qquad (3.27)$$

Where e is the electrical charge, Q is the nuclear quadrupole moment, and V is the electric field gradient due to the total electron density plus all nuclear charges. V can be decomposed into three principal components, V_{zz}, V_{yy}, and V_{xx}, in descending order of magnitude, and η is the asymmetry parameter defined as $(V_{xx} - V_{yy})/ V_{zz}$. For the substates with axially symmetric EFG (η = 0), the energy separation ΔE_Q is,

$$\Delta E_Q = \frac{1}{2} qQV_{zz} \qquad (3.28)$$

The quadrupole splitting provides information on the symmetry of the coordination sphere of the resonating atom.

3.4.3 Magnetic Hyperfine Interaction

The dipole interaction between the nuclear spin moment and the magnetic field is called the Magnetic Hyperfine Splitting (Nuclear Zeeman Effect) [3.23, 3.24]. The hyperfine Hamiltonian for a nuclear magnetic dipole ia a magnetic field H is given by

$H_M = -\mu H$ since $\mu = g\mu_N I$

$$H_M = -g\mu_N IH \qquad (3.29)$$

Where μ_N is the nuclear magnetron $\left(\frac{e\hbar}{2m_N C}\right)$, m$_N$ is the mass the nucleus and g is the gyromagnetic ratio. The energy level are

$$E_M = -\frac{\mu_N H m_I}{I} = g\mu_N IHm_I;\ m_I = I, (I-1)\ ... \qquad (3.30)$$

A nuclear state with spin I > 1/2 possesses a magnetic dipole moment μ. The magnetic field splits the nuclear level of spin I into (2I + 1) equispaced non-degenerate substates characterized by the magnetic spin quantum numbers m$_I$. Transitions between the excited state and ground state can only occur where m$_I$ changes by 0 or 1. This gives six possible transitions for a 3/2 to 1/2 transition, giving a sextet as illustrated in Figure 3.9

$$H = -\frac{8}{3} n\mu_B \left|\psi_\uparrow(0)\right|^2 \bar{s} - 2\mu_B \left\langle \bar{l} \right\rangle \left\langle \frac{1}{r^3} \right\rangle - 2\mu_B \frac{\left\langle 3\left(\bar{r}.\bar{\Delta}\right)\bar{r} - r^2 \bar{s} \right\rangle}{r^5} \qquad (3.31)$$

Where μ$_B$ is Bhor magnetron, s and l are operators for the spin and orbital moment of the electron and $\left|\psi_\uparrow(0)\right|^2$ is the electron density at the nucleus with $+\frac{1}{2}$ spin projection. The first term, in this expression is known as Fermi contact term which describes the contact magnetic interaction between the s-electrons and a nucleus, only S- electron contribute to the Fermi contact term since the S- electron have a non-zero charge density at the nucleus. The field resulting from this source is very large compared to that from other sources. The Fermi contact field mainly arises from the polarization of the spins of paired S- electrons by the unpaired 3d electrons via exchange attraction that emits between electrons of like spins [3.12-3.13]. The inner core electrons (1s and 2s) produce a large negative field, whereas 3s and 4s electron produce smaller positive fields resulting in a net negative field almost of the nuclei [3.14]. The second term in the above expression is known as orbital current field and it is produce due to an interaction of the unquenched orbital moment of the electron with the nuclear magnetic moment.

The third term known as Dipolar field arises due to dipole-dipole interactions operation between the electron spin and the nuclear magnetic moment. For observing a well resolved Zeeman splitting in the Mössbauer spectrum, two conditions have to satisfied

$$\tau_0 > \tau_L \quad \text{and} \quad \tau_s > \tau_L \tag{3.32}$$

Where τ_0 the life time of the nuclear is excited state, τ_s is the electron spin correlation time and τ_L is the larmour precession time of the nucleus.

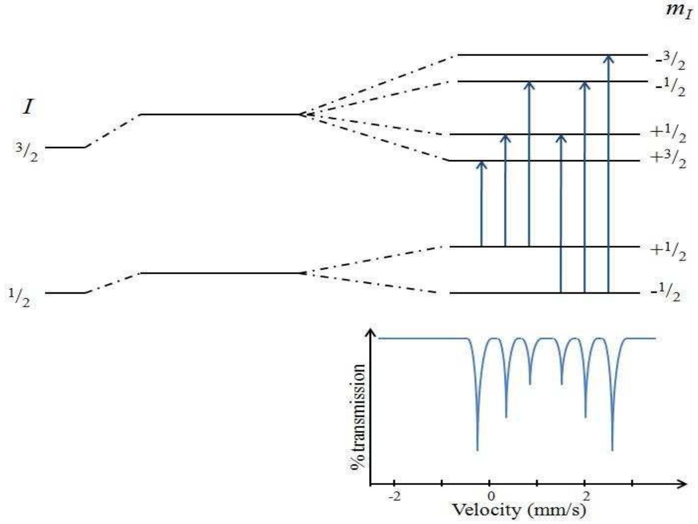

Figure 3.10: The Magnetic Splitting of the nuclear energy levels and corresponding Mossbauer spectrum.

The line positions are related to the splitting of the energy levels, but the line intensities are related to the angle between the Mössbauer gamma-ray and the nuclear spin moment. The outer, middle and inner line intensities are related by:

$$3 : \frac{4Sin2\theta}{1 + Cos2\theta} : 1 \tag{3.29}$$

Meaning the outer and inner lines are always in the same proportion but the middle lines can vary in relative intensity between 0 and 4 depending upon the angle the nuclear spin moments make to the gamma-ray. In polycrystalline samples with no applied field this value averages to 2 as shown in figure 3.9 but in single crystals or under applied fields the relative line intensities can give information about moment orientation and magnetic ordering.

3.4.4 Experimental Procedure for Mössbauer Spectrometer

The γ-ray source is attached to a vibrating mechanism driven so as to cause a triangular velocity waveform. That is, the velocities of the emitting source are swept through a specified range, increasing and then decreasing linearly with time. The velocity range is selected with a dial control, with maximum velocity up to 20 mm/s. The γ-rays which pass through the sample are detected by a proportional counter. Signals from the counter pass through a pre-amp and a linear amplifier before reaching a single-channel analyzer (SCA), which generates a digital pulse if the analog signal falls within a selected pulse-height range. The digital output from the SCA is fed into the computer which sorts the event into the associated velocity bin. The computer accumulates data in 1000 data bins, each corresponding to a specific velocity. Synchronization is maintained between the computer and piston-driving electronics so as to produce one pass through all bins for each oscillation cycle. This produces a spectrum with two zero-velocity positions, near bins 256 and 750, and with the maximum speeds near bins 1, 500, and 1000 (Though note that the online display counts bins from 0 instead of 1). On the computer screen, several versions of the same information are displayed in order to "see" the accumulating data at different resolution. The Mössbauer effect allows for very precise measurements of γ- rays resonance. In combination with Doppler shift, it can be used to observe the hyperfine splitting of ^{57}Fe nucleus and thus determine the internal field of the ^{57}Fe nuclei. A measurement of the line width can also be made. The source used in this experiment is ^{57}Co which decays with a half-life of 270 days to the l36.4 keV excited state of ^{57}Fe by electron capture. Gamma-ray transitions then occur very quickly by two paths, either to the 14.413 keV state, or directly to the ground state. The emission of the l4.413keV γ-ray has a significant recoilless fraction, and is the one used in this experiment. The emitted photon energies are unsplit, i.e. they have only one precise energy. This is because this source was prepared by ion implantation of the cobalt into a copper substrate, in which none of the perturbing interactions are present. The ground state of the ^{57}Fe has spin $\frac{1}{2}$, and the excited state at 14.413 keV has spin $\frac{3}{2}$. The samples used for absorbers are stainless steel (which exhibits only the isomer effect), soft iron (which shows the Zeeman splitting and the isomer effect), sodium nitroprusside "SNP" ($Na_2Fe(CN)_5NO\ .2H_2O$) (which shows the quadrupole splitting and the isomer effect), and hematite (α-Fe_2O_3) (which shows all the effects).

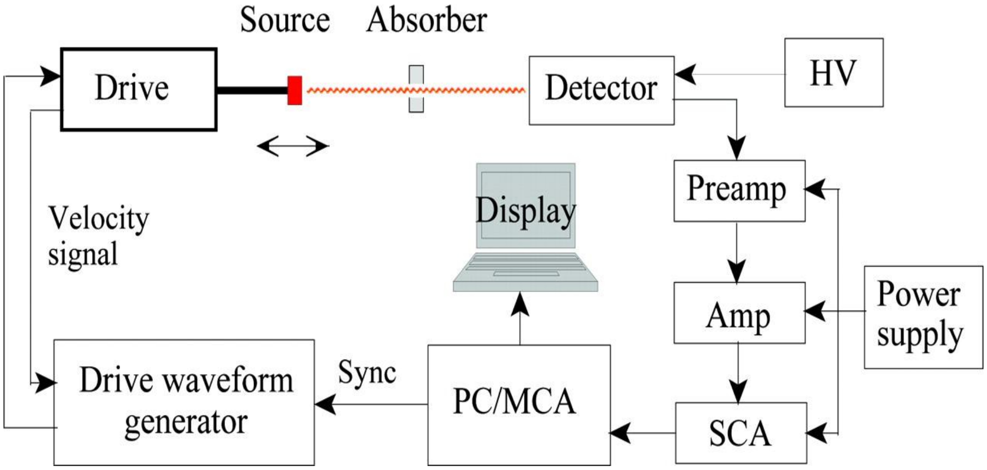

Figure 3.11: Schematic diagram of Mössbauer Spectroscopy

Note that hematite is a very common mineral oxide of iron and is one of form of iron ore. Each absorber contains the naturally-occurring abundance of the ^{57}Fe isotope of iron, which is about 2%. The experimental apparatus of schematic diagram of Mössbauer spectroscopy shown in the figure 3.10. This experiments on the cobalt Zinc ferrite powder sample were performed Materials Science Division, AECD.

3.5 Dynamic Light scattering (DLS)

Dynamic light scattering (DLS) is a technique in physics that can be used to determine the size distribution profile of small particles in suspension in polymer solution [3.34]. In the scope of DLS, temporal fluctuations are usually analyzed by means of the intensity or photon auto-correlation function (also known as photon correlation spectroscopy or quasi-elastic light scattering). In the time domain analysis, the autocorrelation function (ACF) usually decays starting from zero delay time, and faster dynamics due to smaller particles lead to faster decorrelation of scattered intensity trace. It has been shown that the intensity ACF is the Fourier transformation of the power spectrum, and therefore the DLS measurements can be equally well performed in the spectral domain. DLS can also be used to probe the behavior of complex fluids such as concentrated polymer solutions.[3.35]

3.5.1 Theory of Dynamic Light scattering (DLS)

The DLS technique investigates the relationships between the normalized time autocor relation function $g^{(2)}(\tau)$ and the delay timeτ was done by Y. Sun in his M.S thesis. The time dependence of scattered light is analyzed in terms of the time autocorrelation function$\langle I(t) + I(t+\tau)\rangle$, where $I(t)$ and $I(t+\tau)$ are the scattered intensities of light at time t and $t+\tau$ and τ is the delay time [22]. Results are typically expressed in terms of the normalized time autocorrelation function $g^{(2)}(\tau)$

$$g^{(2)}(\tau) = \frac{\langle I(t) + I(t+\tau)\rangle}{\langle I(t)\rangle^2} \tag{3.33}$$

Where the braces indicate averaging over time. The time autocorrelation function of the scattered light intensity is related to the scattered field by

$$\langle I(t) + I(t+\tau)\rangle = \langle |E(t)|^2 |E(t+\tau)|^2\rangle = \langle |E(t)|^2\rangle\langle |E(t+\tau)|^2\rangle + \langle E(t)E^*(t+\tau)\rangle\, \langle E(t+\tau)E^*(t)\rangle \tag{3.34}$$

Where $E(t)$ and $E(t+\tau)$ are the scattered electric field of light at time t and $t+\tau$, respectively. Using the relations

$$\langle |E(t)|^2\rangle = \langle |E(t+\tau)|^2\rangle \tag{3.35}$$

And

$$\langle E(t+\tau)E^*(t)\rangle = \langle E(t)E^*(t+\tau)\rangle \tag{3.36}$$

Equation (2.34) can be written

$$\langle I(t) + I(t+\tau)\rangle = \langle |E(t)|^2\rangle^2 + \langle E^*(t+\tau)\rangle^2 \tag{3.37}$$

Using the normalized time autocorrelation function of the electric field of the scattered light $g^{(1)}(\tau)$,

$$g^{(1)}(\tau) = \frac{\langle E(t)E^{*}(t+\tau)\rangle}{\langle E(t)E^{*}(t)\rangle} \tag{3.38}$$

The normalized intensity correlation function can be written

$$g^{(2)}(\tau) = 1 + (g^{(1)}(\tau))^2 \tag{3.39}$$

This is known as the Siegert relation. To this point only the complex amplitude at a single point on the detector has been considered. In practice, large detector apertures are commonly used. The statistical consequences of spatial averaging over the detector apertures must be calculated. For a typical continuous-wave gas laser, beam-intensity profiles are reasonably close to a Gaussian bell shape. The complex field or the intensity of scattered light is a stochastic process in space as well as in time. From the Siegert relation and considering the spatial dependence, one can write the normalized time autocorrelation function of the intensity of the scattered light $g^{(2)}(\tau)$ as

$$g^{(2)}(\tau) = 1 + \beta[g^{(1)}(\tau)]^2 \tag{3.40}$$

Where $\beta + 1$ is the value of the normalized time autocorrelation function of the intensity of the scattered light at a given scattering angle and zero delay time

For a solution of noninteracting, monodisperse particles, $g^{(1)}(\tau)$has the form

$$g^{(1)}(\tau) = \exp(-\Gamma_{\tau}) \tag{3.41}$$

Where $\Gamma = q^2 D$is the decay rate, D is the macromolecular translational diffusion coefficient of the particles and q is the magnitude of the scattering vector.

For a polydisperse system, $g^{(1)}(\tau)$ consists of a distribution of exponentials

$$g^{(1)}(\tau) = \int_0^{\infty} G(\Gamma)e^{-\Gamma_{\tau}}d\Gamma \tag{3.42}$$

Where, $G(\Gamma)$ is the normalized distribution of the decay rates.

The size distribution can be obtained using the method of moment analysis. For this calculation, a mean decay rate $\bar{\Gamma}$ and the moments of the distribution μ_i are defined

$$\bar{\Gamma}=\int_0^{\infty} \Gamma G(\Gamma) d\Gamma \tag{3.43}$$

$$\mu_2 = \int (\Gamma - \bar{\Gamma})^2 G(\Gamma) d\Gamma \tag{3.44}$$

$$\mu_3 = \int (\Gamma - \bar{\Gamma})^3 G(\Gamma) d\Gamma \tag{3.45}$$

Assuming that $(\Gamma - \bar{\Gamma})\tau \ll 1$, one can write the exponential function in Eq. 3.39 as

$$\begin{aligned} \exp(-\Gamma_\tau) &= \exp(-\bar{\Gamma}_\tau) \exp(-(\Gamma - \bar{\Gamma})\tau) \\ &= \exp(-\bar{\Gamma}_\tau) [1 - (\Gamma - \bar{\Gamma})\tau + \frac{(\Gamma - \bar{\Gamma})^2 \tau^2}{2!} +..] \end{aligned} \tag{3.46}$$

Substituting this expression into Eq. 3.39, we get

$$g^{(1)}(\tau) = \exp(-\bar{\Gamma}_\tau)[1 + \frac{\mu_2 \tau^2}{2!} + \frac{\mu_3 \tau^3}{3!} + \cdots] \tag{3.47}$$

Then the intensity-intensity autocorrelation function can be written as

$$g^{(2)}(\tau) = 1 + \beta \exp(-2\bar{\Gamma}_\tau)[1 + \frac{\mu_2 \tau^2}{2!} + \frac{\mu_3 \tau^3}{3!} + \cdots]^2 \tag{3.48}$$

Details of the particle size distribution can then be obtained by fitting equation (3.48) to the data. The apparent hydrodynamic radius R_h is defined using the Stokes-Einstein relation

$$R_h = \frac{K_B T}{6\pi \eta_0 D} \tag{3.49}$$

Where, η_0, K_B and T are the viscosity of the solvent, Boltzmann's constant and the absolute temperature. Equation. 3.38 is obtained in the Stokes approximation for stick-boundary conditions [3.36- 3.37].

The width of the hydrodynamic radius distribution and the polydispersity index are defined as [3.38]

$$Width = \frac{\sqrt{\mu_2}}{\bar{\Gamma}} R_h \qquad (3.50)$$

$$PD.I = \frac{\sqrt{\mu_2}}{\bar{\Gamma}^2} \qquad (3.51)$$

3.5.2 Assembly of a Dynamic Light scattering (DLS)

This experiments on the cobalt Zinc ferrite powder sample were performed Materials Science Division, AECD. A principal scheme of a DLS set-up is given in figure. 3.12. In a typical set-up of a DLS experiment the sample is contained in a fixed holder. It is il luminated from a coherent monochromatic light source. Typically, lasers (often He-Ne with 632.8 nm or Ar-ion with 592 nm wavelength) with vertical polarization are used. The scattered light from the particles is collected by a detector under the scattering angle θ. In industrially relevant commercial instruments usually one or a set of fixed scattering angles is used while in academic applications goniometers that allow for measurements at different scattering angles can be found. In recent developments also fiber optics are used that act simultaneously as illuminating and detection optics (θ = 180°). The scattered light is then coupled out in a Y-coupler and led to the detector.

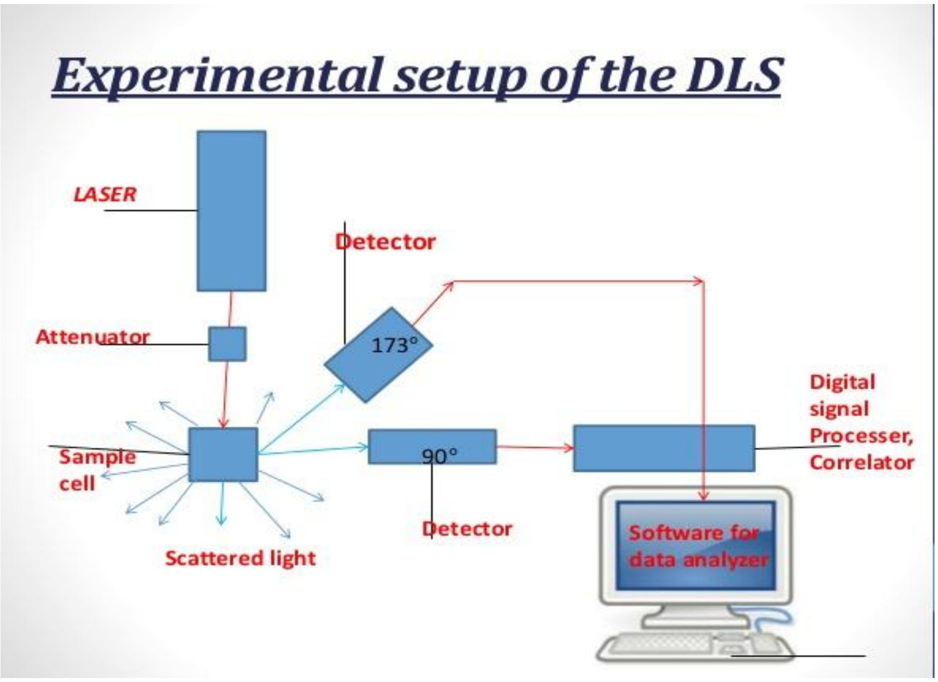

Figure 3.12: Scheme of a typical DLS set-up

Photomultiplier tubes (PMT) or Avalanche Photodiodes (APD) are used as detectors in DLS set ups. A photomultiplier has a photocathode at the entry window. When a photon of the scattered light hits the photocathode, an electron is produced by the photoelectric effect. This electron is then multiplied at the following dynodes by secondary emission which finally leads to a measurable current at the anode. Avalanche photodiodes can be regarded as the semiconductor analogue to photomultipliers. A high barrier voltage leads to an enormous internal gain of an incoming photon by ionization in the barrier layer. From the functional principle of a PMT and an APD it is clear that the measurement of the scattered intensities means counting the impinging photons. The photon count rate (Number of photons per unit time in kHz) is taken as an equivalent to the intensity. The detected scattering signal is processed to obtain information on the diffusional properties of the sample. Finally, a computer is used for data output and handling.

3.6 Magnetic Hyperthermia

Magnetic hyperthermia is a promising option for cancer therapy. In this method, MNPs are heated by external alternating (AC) magnetic field. After applying magnetic field, nanoparticles are generate heat by the process of eddy current, hysteresis losses, and relaxation loss. Advances in science have made it so that magnetic nanoparticles can be specifically targeted at cancer cells, making magnetic hyperthermia a truly local treatment. MNPs can therefore, be used to induce localized hyperthermia used to kill tumor or by increasing the effectiveness of radiotherapy or chemotherapy. The procedure consist of dispersing MNPs within the target tissue and applying a Ac magnetic field that cause the particle produce heat. In addition, due to the small area of the treatment, the nanoparticles can be heated to a temperature high enough to kill the cancer cells while keeping surrounding tissue unaffected.

3.6.1 Heating Mechanism of Nanoparticle

The heat generation of magnetic nanoparticle can be achieved by three different way using alternating field, which are Eddy current loss, hysteresis losses, Néel and Brownian relaxation. Each process of heat generation strongly depends on the crystal size of the nanoparticle. Mainly, single domain nanoparticle are used in magnetic fluid hyperthermia treatment. In such small NPs, magnetization relaxation is governed by a combination of the external rotation (Brownian) and internal (Néel) diffusion of the particle's magnetic moment, with a negligible contribution of hysteresis loss [3.39].

3.6.1.1 Hysteresis Loss

Hysteresis**,** lagging of the magnetization of a ferromagnetic material, such as iron, behind variations of the magnetizing field. When ferromagnetic materials are placed within a coil of wire carrying an electric current, the magnetizing field, or magnetic field strength H, caused by the current forces some or all of the atomic magnets in the material to align with the field. The net effect of this alignment is to increase the total magnetic field, or magnetic flux density B. The aligning process does not occur simultaneously or in step with the magnetizing field but lags behind it.

If the intensity of the magnetizing field is gradually increased, the magnetic flux density B rises to a maximum, or saturation, value at which all of the atomic magnets are aligned in the same direction. When the magnetizing field is diminished, the magnetic flux density decreases, again lagging behind the change in field strength H. In fact, when H has decreased to zero, B still has a positive value called the remanence, residual induction, or retentivity, which has a high value for permanent magnets. B itself does not become zero until H has reached a negative value. The value of H for which B is zero is called the coercive force. A further increase in H (in the negative direction) causes the flux density to reverse and finally to reach saturation again, when all the atomic magnets are completely aligned in the opposite direction. The cycle may be continued so that the graph of the flux density lagging behind the field strength appears as a complete loop, known as a hysteresis loop. The energy lost as heat, which is known as the hysteresis loss, in reversing the magnetization of the material is proportional to the area of the hysteresis loop. Therefore, cores of transformers are made of materials with narrow hysteresis loops so that little energy will be wasted in the form of heat.[3.40]

The application of an alternating field with an amplitude of more than two times of the coercivity of the particles, the hysteresis will defeat and the flipping of the magnetization in the particles leads to heating of the particles. If an assembly of MNPs is put into an alternating magnetic field of frequency f and amplitude $\mu_0 H_{max}$, the amount of heat 'A' released by the MNPs during one cycle of the magnetic field simply equals the area of their hysteresis loop. The amount of heat released by ferromagnetic material through hysteresis loss is given by,

$$A = \int_{H_{min}}^{H_{max}} \mu_0 M(H) dH \tag{3.52}$$

Then the SAR is

$$SAR = fA \tag{3.53}$$

Where *f* denotes the frequency of the AC magnetic field and it is expressed as *f* = ω/2π, M magnetization and H applied magnetic field.

3.6.1.2 Eddy Current

Eddy currents are loops of electrical current induced within conductors by a changing magnetic field in the conductor, due to Faraday's law of induction. By Lenz's law, an eddy current creates a magnetic field that opposes a change in the magnetic field that created it, and thus eddy currents react back on the source of the magnetic field.

Following the Faraday-Lenz's law of electromagnetic induction, when an AC field penetrates a conducting sample, the associated time-varying magnetic flux will induce the evolution of eddy currents opposing to the applied field shown in figure 3.12. This results in a field attenuation, which will depend on the field frequency, the electrical conductivity of the material and its permeability. The heat loss due to eddy currents (ED) is given by,

$$ED = \frac{(\mu \pi d f H)^2}{20\rho} \tag{3.54}$$

Where μ is the permeability of a material, *d*, the diameter of the particle and ρ, resistivity of the material.

In comparison to magnetic losses eddy current induced heating of small magnetic particles is negligibly small. Thus the magnetic induction heating of ferrite materials is mainly caused by hysteresis loss and relaxation loss in alternating magnetic field [3.41].

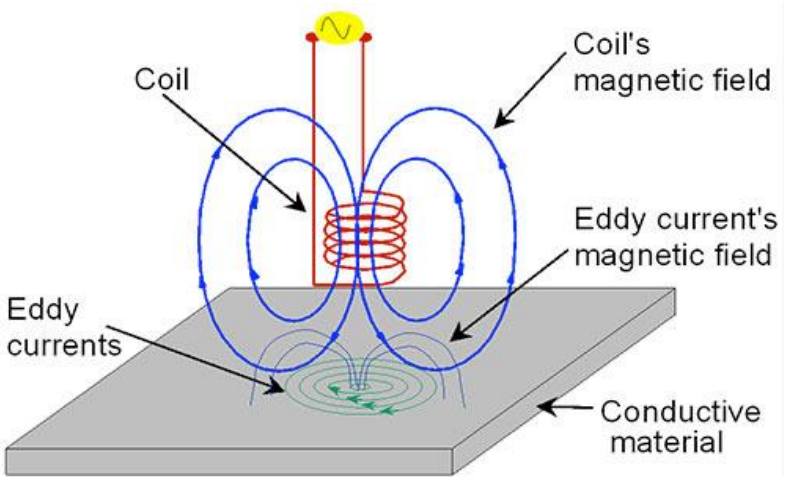

Figure 3.13: Eddy Current

3.6.1.2 Relaxation Loss

When the volume of a small particle is reduced below a certain value, called critical domain size, $D_{critical}$, the proximity of many domain walls in a small volume is not energetically stable, so that a single-domain configuration is adopted. Within this single magnetic domain all the atomic magnetic moments will be magnetized along the same direction, adding up so they behave like a giant magnetic moment (superparamagnet). In this case, an external AC magnetic field supplies energy and assists magnetic moments to rotate in overcoming the energy barrier E ~ KV, where K is the anisotropy constant and V is the volume of the magnetic core. Superparamagnetic MNPs show two different kinds of heat generating mechanism, Néel relaxation and Brown relaxation mechanism.

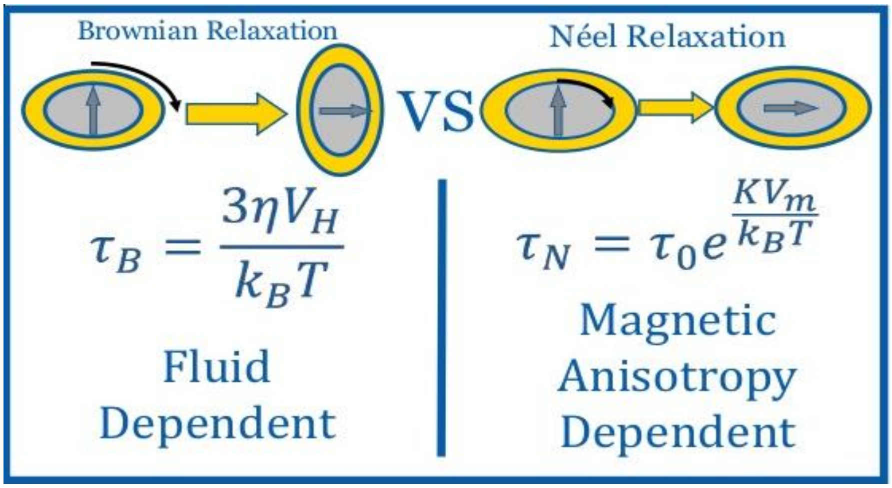

Figure 3.14: Brownian and Neel Relaxation

The Néel relaxation mechanism is characterized by the rotation of the magnetic spin moment. In this case, the magnetic anisotropy energy barrier of the superparamagnetic MNPs needs to be overcome before the reversal of the magnetization of the superparamagnetic NPs can occur. Thus, the intrinsic anisotropy (material, surface, shape, etc.) and the volume of the superparamagnetic NPs affect the Néel relaxation time and hence the heating efficiency of the superparamagnetic NPs. The formula for the Néel relaxation time constant

$$\tau_N = \tau_0 e^{\frac{kV_m}{K_B T}} \tag{3.55}$$

Where τ_0 is the relaxation factor, K is the magnetic anisotropy energy density, is the mean particle volume, kB is the Boltzmann constant, and T is the absolute temperature.

In Brownian rotational relaxation (τ_B), the magnetic moment aligns with the magnetic field (H) and the particle rotates under an AC field. During rotation, collision with the surrounding medium generates heat. Heat dissipation phenomena observed is due to the rotational Brownian motion of the particle within the carrier liquid. In essence, this is attributed to the rotation of the magnetic particle as a whole because of the torque exerted on the magnetic moment by the external AC magnetic field. Energy has to be provided to overcome the rotational friction offered by the adjacent liquid. This energy is released during relaxation is called Brown relaxation. Brownian relaxation at temperature (T) is given by

$$\tau_b = \frac{3\eta V_H}{K_B T} \tag{3.56}$$

Where η is the dynamic viscosity of carrier liquid and V_H is the hydrodynamic radius of the particle, K_B is Boltzmann constant.

RESULT AND DISCUSSION

4.1 Structural Analysis

Ferrite powder of $Co_{0.5}Zn_{0.5}Fe_2O_4$ nanoparticles were prepared by co-precipitation method. The as-prepared and the samples annealed at 200^0C, 400^0C, 600^0C, 800^0C and 1000^0C were analyzed by Bruker XRD system with Cu- K_α radiation of wavelength λ= 1.5406 A^0 in the range of 2θ=15 to 80^0 in the step of 0.02^0, those are presented in figure 4.1 (a, b, c, d, e, and f) and combined in figure 4.2. The as-prepared and annealed samples were examined using XRD in order to determine the crystal structure, lattice parameter and average crystallite size.

The structural characterization and the identification of phases are prior for the study of the ferrite properties. The result obtain from the XRD pattern for all samples of $Co_{0.5}Zn_{0.5}Fe_2O_4$ with the (hkl) values corresponding to the diffraction peaks of different plane (111), (220), (311), (400), (511) and (440) represents either even or odd, indicating the sample are spinal cubic phase. The reflection also demonstrate the homogeneity of the samples. It has been also found from those figure, that well defined peaks of major phase of $Co_{0.5}Zn_{0.5}Fe_2O_4$ with good diffraction line broadening, indicating the formation of Co-Zn ferrite samples have spinal cubic structure with a single phase. The most intense reflection peak (311) at approximately $2\theta = 35^0$ is indicated in each diffraction pattern of the samples. It must be noted that these peak, as with other peaks present in the samples sharpen and narrow as they are heated making more intense and more clearly seen by the naked eye. This is a direct result of the particle growth's contribution to the annealing process, not in the internal crystallographic ordering. This observations matches with those of earlier reports [4.1, 4.2]. All peaks were matched with indexed reference pattern: 89-1012 for Zinc iron oxide and 22-1086 for cobalt iron oxide [4.2].

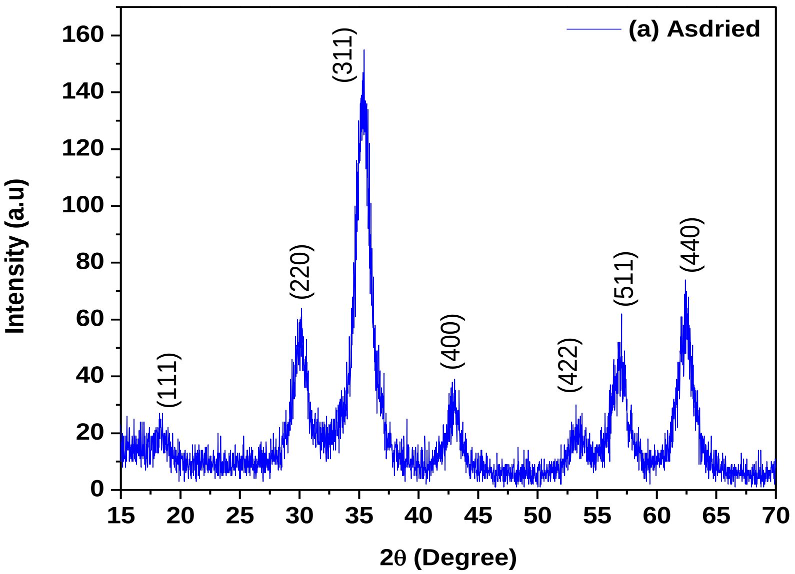

Figure 4.1 (a): XRD spectra of $Co_{0.5}Zn_{0.5}Fe_2O_4$ nanoparticles (as-dried sample)

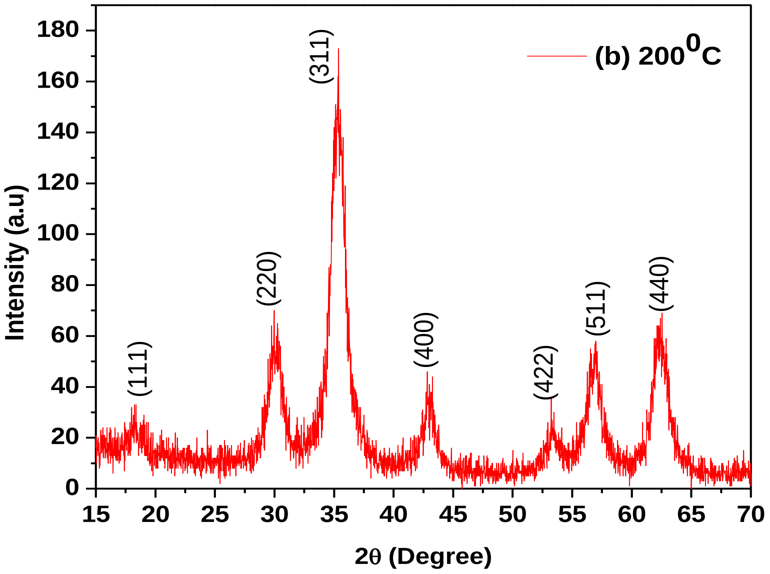

Figure 4.1 (b): XRD spectra of $Co_{0.5}Zn_{0.5}Fe_2O_4$ nanoparticles annealed at 200^0C

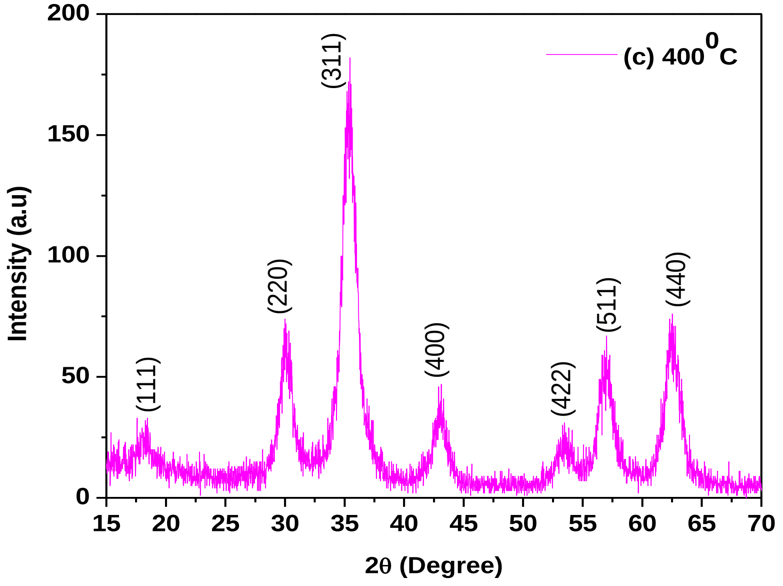

Figure 4.1 (c): XRD spectra of $Co_{0.5}Zn_{0.5}Fe_2O_4$ nanoparticles annealed at 400^0C

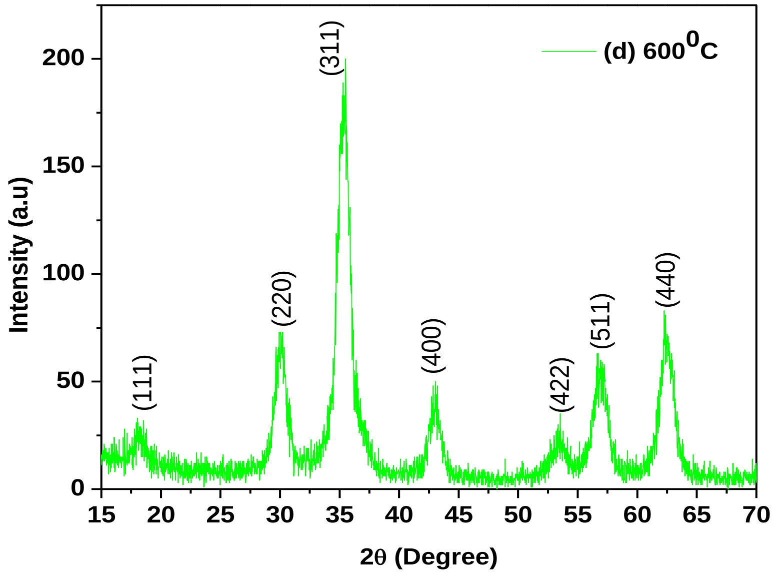

Figure 4.1 (d): XRD spectra of $Co_{0.5}Zn_{0.5}Fe_2O_4$ nanoparticles annealed at 400^0C

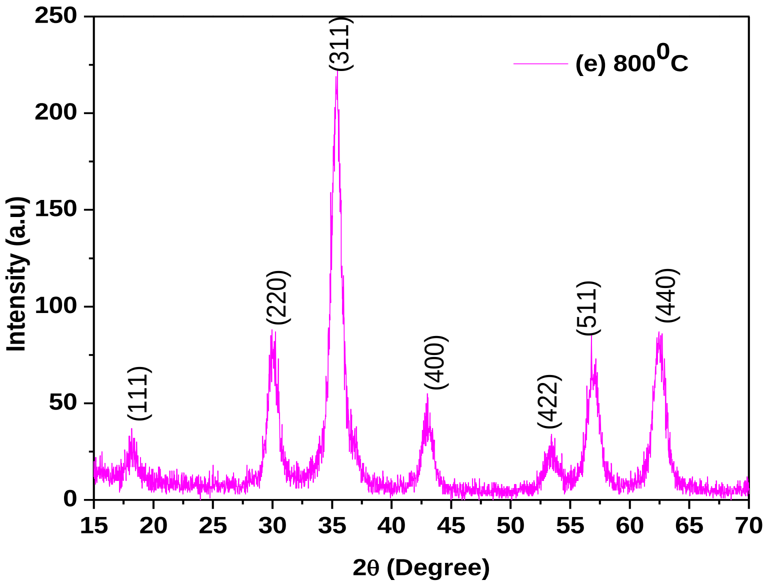

Figure 4.1 (e): XRD spectra of $Co_{0.5}Zn_{0.5}Fe_2O_4$ nanoparticles annealed at 800^0C

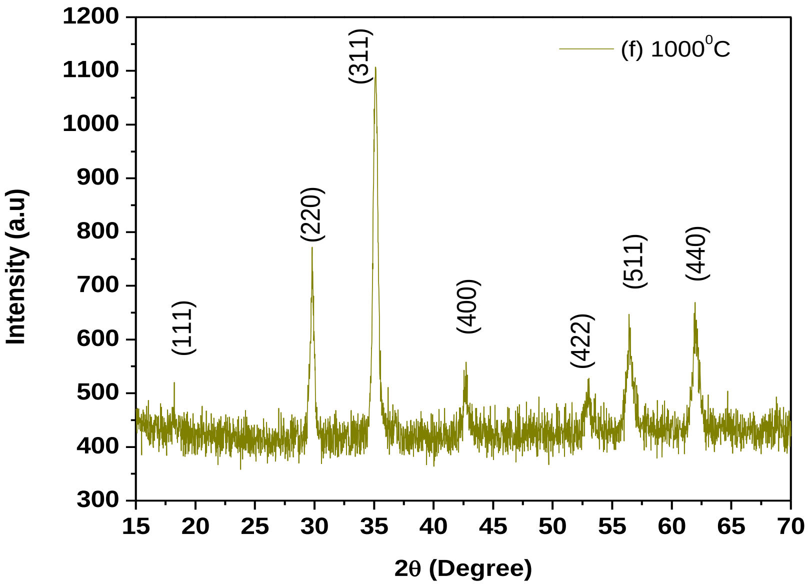

Figure 4.1 (f): XRD spectra of $Co_{0.5}Zn_{0.5}Fe_2O_4$ nanoparticles annealed at 1000^0C

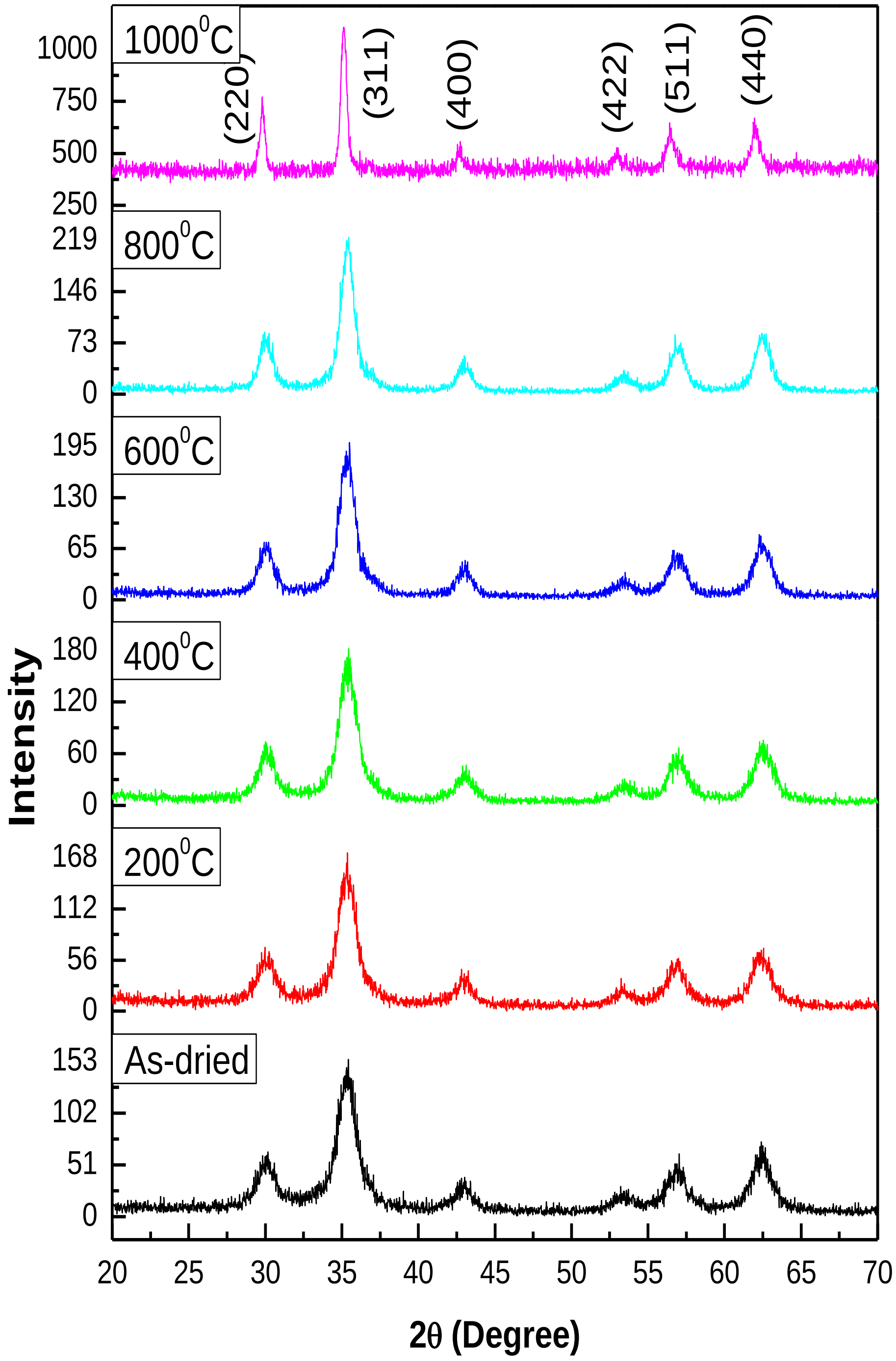

Figure 4.2: Compare the XRD patterns of as dried and annealed $Co_{0.5}Zn_{0.5}Fe_2O_4$ nanoparticles

From figure 4.3 the average crystallite size was calculated from the full- width half-maxima (FWHM) of (311) reflection peak, which is the strongest reflection, by using Scherer's formula [4.3]. The average crystallite size of $Co_{0.5}Zn_{0.5}Fe_2O_4$ reveals growth of grain from 6nm to 24nm the samples were annealed from 200^0C to 1000^0C respectively. XRD analysis indicates that the crystallite size increases as annealing temperature of the Co-Zn ferrite samples increases and the intense diffraction feature become stronger due to the growth of grains. This indicates that, with more annealing, the crystallite size of Cobalt Zinc Ferrite single phase increased as a result of rising atomic mobility and higher reaction temperature as well as disappearing structural defects and dislocations.

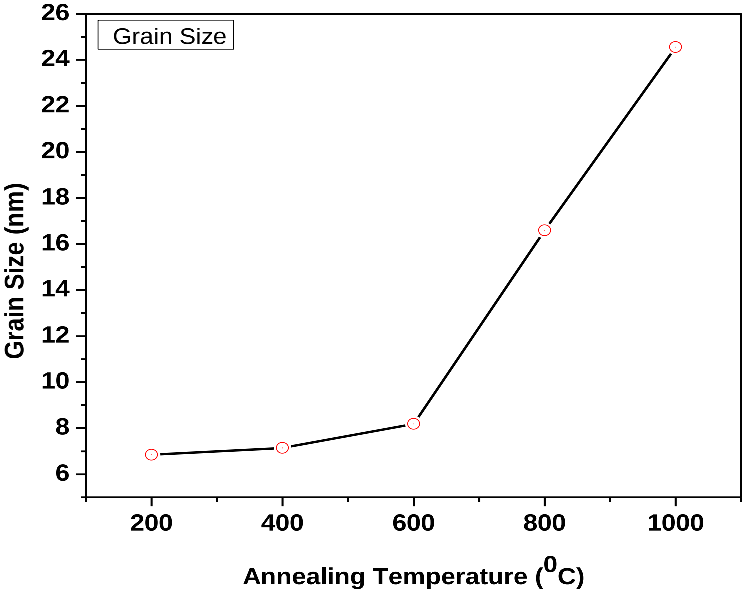

Figure 4.3: Variation of the grain size with different annealing temperature for $Co_{0.5}Zn_{0.5}Fe_2O_4$ nanoparticles

In figure 4.4 shown the lattice parameters "a" which was calculated from the spacing of the relative parameter (hkl) of the sample. The result are depicted that the lattice parameter remained almost constant with the raising of the annealing temperature, which provided the information of a compositionally homogeneous structure.

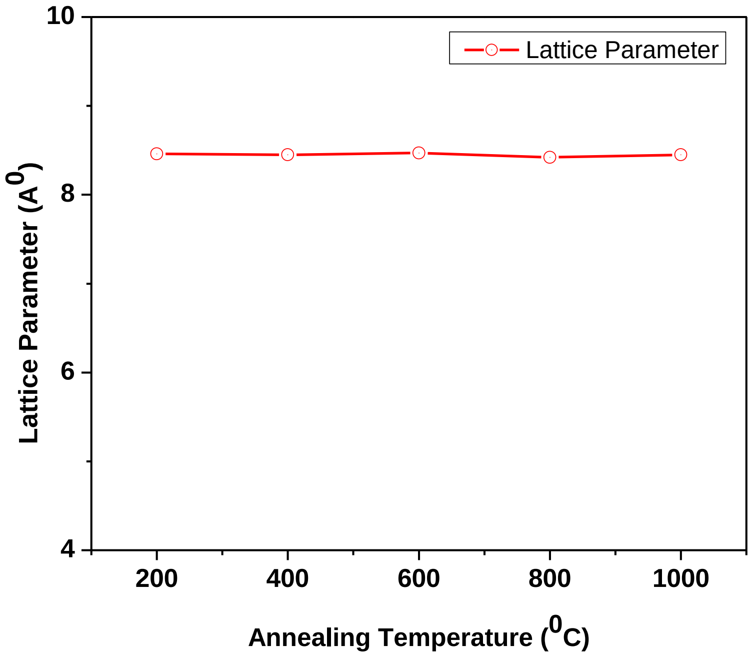

Figure 4.4: Variation of the lattice parameter with different annealing temperature for $Co_{0.5}Zn_{0.5}Fe_2O_4$ nanoparticles

In the following table 4.1 the crystallite size and lattice parameter are presented numerically with annealing temperature. This calculated lattice parameter a = 8.5A^0 are close agreements with the standard JCPDS file number # 89-1012

Table 4.1 Average grain size and lattice parameter of $Co_{0.5}Zn_{0.5}Fe_2O_4$ nanoparticles annealed at different temperature

Annealing Temperature (^0C)	Crystal Size (nm)	Lattice Parameter (A^0)
200	6	8.46
400	7	8.45
600	8	8.47
800	17	8.42
1000	25	8.45

4.2 Magnetic Properties analysis

Magnetic properties of a ferrite nanoparticles are immense interest for the fundamental understanding of magnetic interaction and have a great significance finding to their possible applications. The chemical composition and size of the particles play an important role in determining the magnetic properties. The magnetic properties of the as-prepared and annealed samples were determined by using Vibrating Sample Magnetometer (VSM) and Mössbauer experiment.

4.2.1 Effect of Annealing Temperature on the Magnetic Properties

To understand the magnetic properties for the different annealing temperature and corresponding crystallite size all the sample were characterized using VSM at room temperature within the applied magnetic field range -20KOe to +20KOe. The variation of the magnetization (M) as a function of applied field (H) for as-prepared and annealed at 200^0C, 400^0C, 600^0C, 800^0C and 1000^0C for $Co_{0.5}Zn_{0.5}Fe_2O_4$ nanoparticles exhibit very clear M-H curve as shown in figure 4.5 (a, b, c, d, e, f) separately and combined curve is shown in figure 4.6.

It has been seen that the magnetization for the samples are week and very narrow hysteresis cycle, this indicates that the samples are soft magnetic nature. The VSM curve reveals the information of hysteresis loop for the $Co_{0.5}Zn_{0.5}Fe_2O_4$ nanoparticles, with zero coercivity and remanance values, which exhibits superparamagnetic behavior of the nanoparticles [4.5-4.8]. On increasing the applied field from 0 to 10KOe, the magnetization "M" increase sharply and become nearly saturated at about 10KOe [4.5].

Figure 4.6 depicts that saturation of magnetization value of $Co_{0.5}Zn_{0.5}Fe_2O_4$ samples increased with the annealing temperature as the magnetic properties are depends on the size and the morphology of the nanoparticles [4.9]. As the annealing temperature changed, particle size of the nanoparticles also changes and surface area to volume ratio changes and hence the magnetic changes. The $Co_{0.5}Zn_{0.5}Fe_2O_4$ nanoparticles obtain from as-dried samples possessed a saturation magnetization M_s of 32.22 emu/g, while the annealed samples obtained after 200^0C, 400^0C, 600^0C, 800^0C, and 1000^0C had M_s value of 29.006 emu/g, 35 emu/g, 40 emu/g and 56.0781 emu/g.

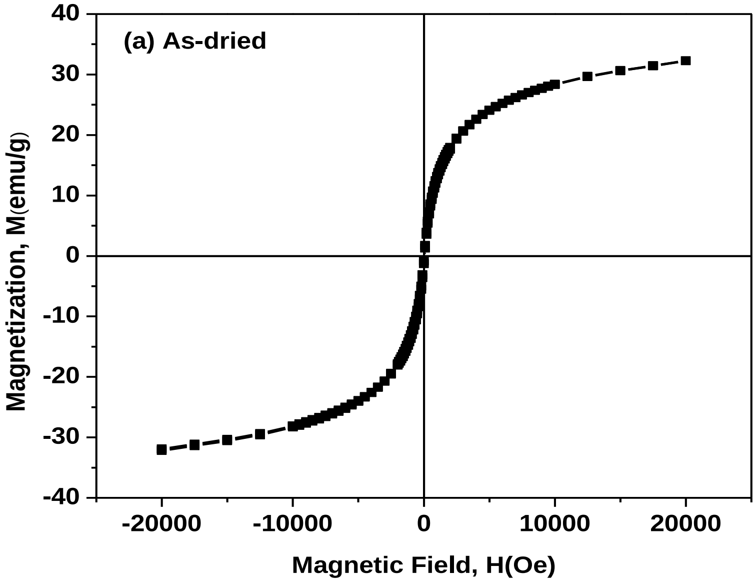

Figure 4.5 (a): M-H loop of $Co_{0.5}Zn_{0.5}Fe_2O_4$ nanoparticles of as-dried sample

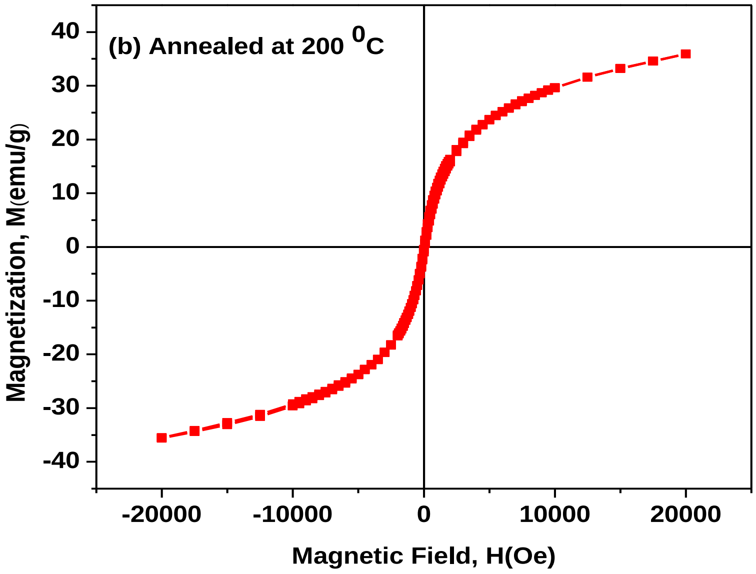

Figure 4.5 (b): M-H loop of $Co_{0.5}Zn_{0.5}Fe_2O_4$ nanoparticles annealed at 200°C

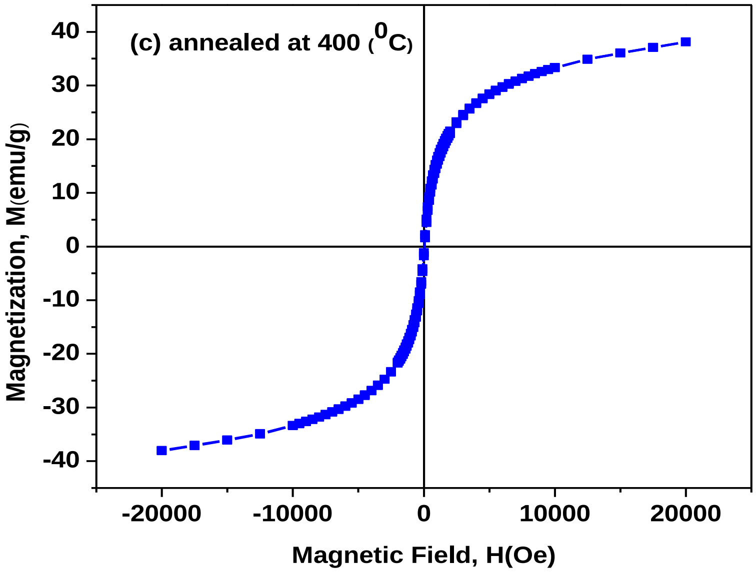

Figure 4.5 (c): M-H loop of $Co_{0.5}Zn_{0.5}Fe_2O_4$ nanoparticles annealed at 400°C

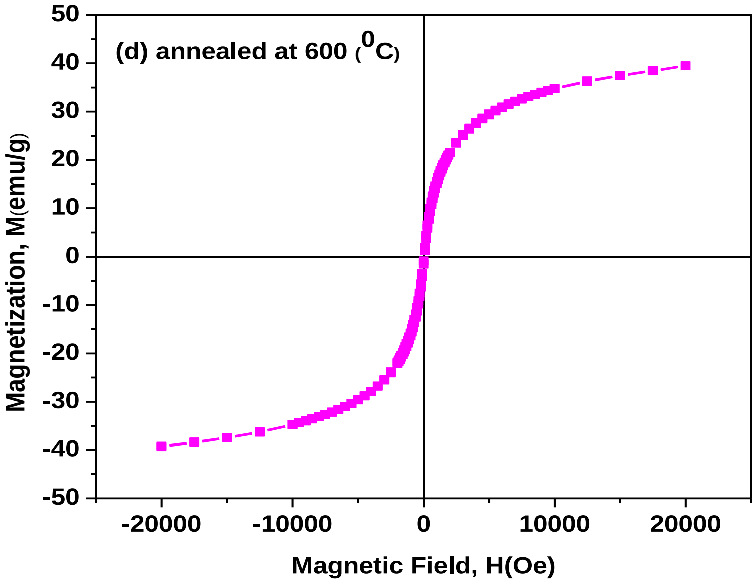

Figure 4.5 (d): M-H loop of $Co_{0.5}Zn_{0.5}Fe_2O_4$ nanoparticles annealed at 600°C

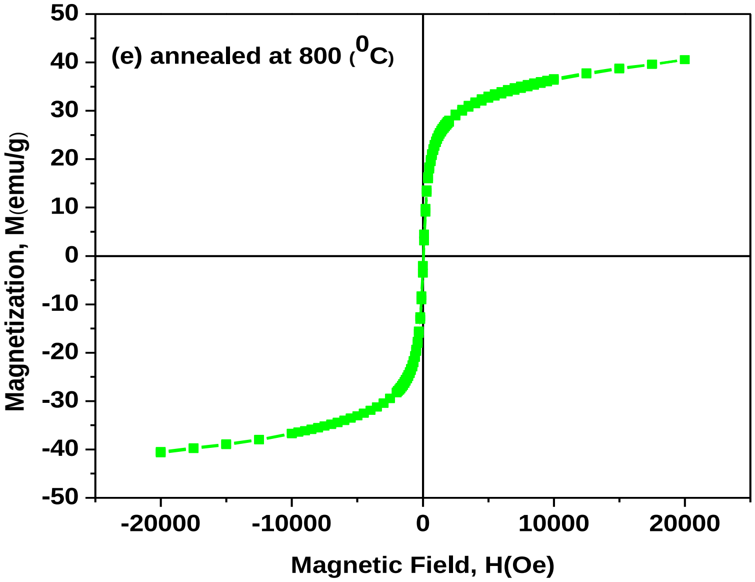

Figure 4.5 (e): M-H loop of $Co_{0.5}Zn_{0.5}Fe_2O_4$ nanoparticles annealed at 800°C

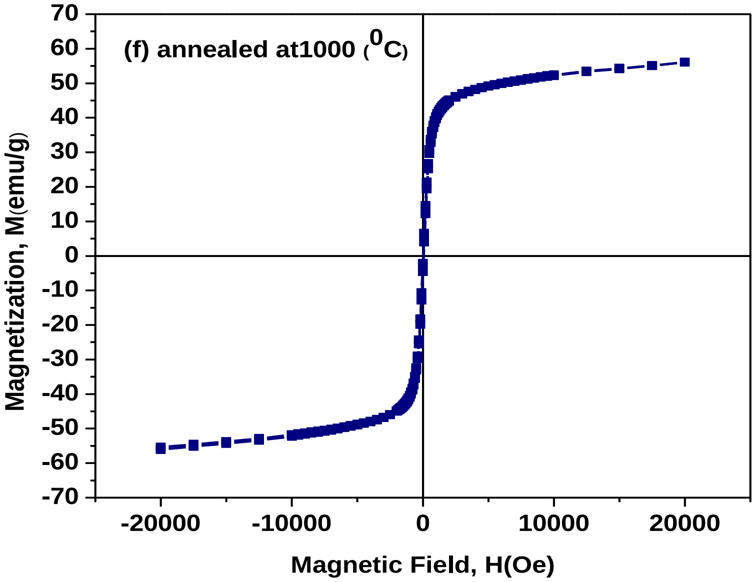

Figure 4.5 (f): M-H loop of $Co_{0.5}Zn_{0.5}Fe_2O_4$ nanoparticles annealed at 1000°C

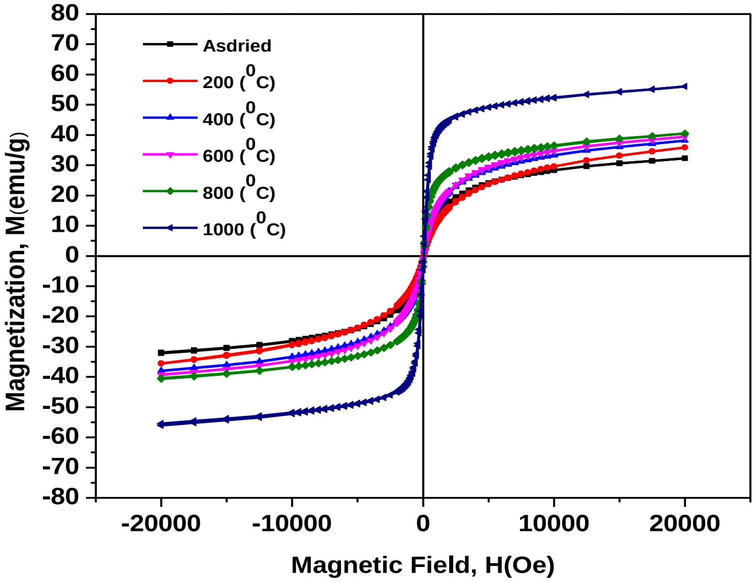

Figure 4.6: Compare the M-H curve among the $Co_{0.5}Zn_{0.5}Fe_2O_4$ nanoparticles of as-prepared and annealed samples

The variation in coercivity (H_c) with annealing temperature is shown in figure 4.7 and in the table 4.2. It is indicated that the annealing temperature have a significance influences on the H_C of prepared nanoparticles. H_c has gausin behavior and exhibit significant values ranging between 8.478 Oe and 16.154 Oe for synthesized ferrite nanoparticles. The variation in H_C with annealing temperature can be explained on the basis of the domain structure and anisotropy of the crystals [4.10]. H_c initially increases slightly with annealing temperature and then increase remarkably reaching its maximum value 16.154 Oe at 600^0C. Upon further annealing, the value of H_C decrease significantly. This variation in the value of H_C may possible be attributed to the crystallite size due to surface effects [4.3]. And above the critical crystallite size, H_c tends to decrease with increase in crystallite size, the number of grain boundaries increases, and consequently H_c of nanoparticles decreases. Hence, the decrease in the H_C with the increasing of annealing temperature can be attributed to decrease in the anisotropy field that in response decrease the domain wall energy.

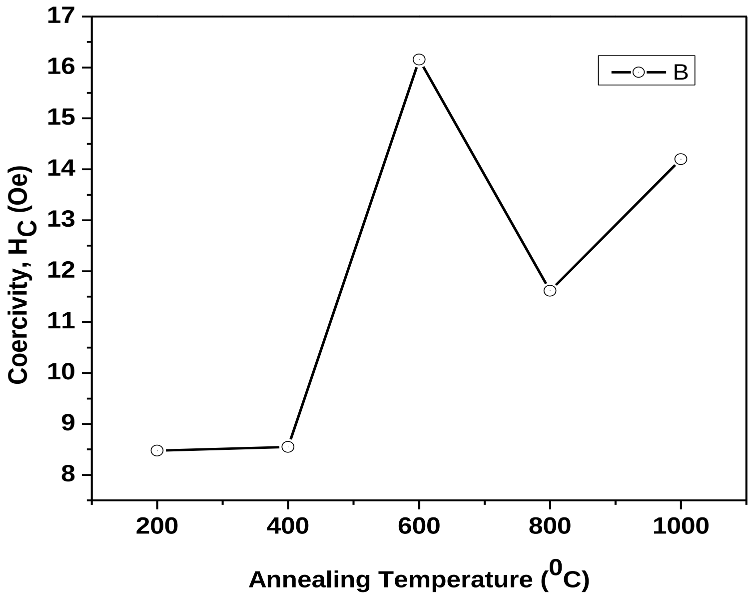

Figure 4.7: The correlation between the coercivity and the annealing temperature of $Co_{0.5}Zn_{0.5}Fe_2O_4$ nanoparticles

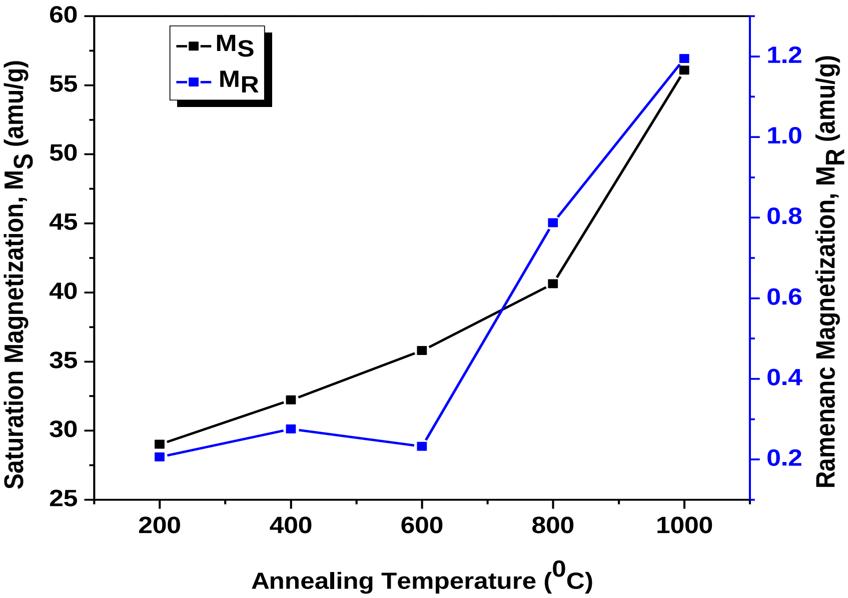

Figure 4.8: Variation of the M_s and M_r with annealing temperature of $Co_{0.5}Zn_{0.5}Fe_2O_4$ samples

From figure 4.8 clearly shows that both the saturation magnetization M_s and M_r increases with increasing value of annealing temperature. This increases of M_s and M_r with respect to annealing temperature can be explain by Neel's theory [4.11]. Both M_s and M_r increases due to a study increase in particle size and crystallinity.

Table: 4.2 Saturation magnetization Ms, Coercivity Hc and Ramenance measured by VSM technique at room temperature for $Co_{0.5}Zn_{0.5}Fe_2O_4$ nanoparticles produced at different annealing temperatures.

Annealing Temperature (^{0}C)	**Coercivity, Hc (Oe)**	**Saturation magnetization, M_s (emu/g)**	**Ramenance, M_r (emu/g)**	**M_r/M_s**
200	8.47	29.00	0.206	0.0071
400	8.55	32.23	0.276	0.0085
600	16.15	35.79	0.232	0.0065
800	11.61	40.63	0.787	0.0194
1000	14.19	56.08	1.195	0.0213

4.3 Mössbauer Study

For biomedical application nanomaterials should be in superparamagnetic state and the size of the particle should be small. Mössbauer Study is one of the prominent methods, which is used to determine the magnetic state of nanoparticles. For performing Mössbauer experiment, the change in spectrum was investigated as a function of temperature. The superparamagnetic behavior is marked by the doublet pattern on the Mössbauer spectrum. The continuous improvement of computation capabilities for spectral analysis and the introduction of sophisticated software for the treatment of Mössbauer data has enabled researchers to obtain rich and valuable information from the Mössbauer experiments as well as to study the structure with high accuracy and from complementary point of view.

The superparamagnetic behavior is indicated by the presence of blocking behavior characteristic by the blocking temperature which mark the transition of the system to a superparamagnetic state.

The fitting of spectral lines were performed assuming Lorentzian absorption line shapes using the Mössbauer spectral fitting software WMOSS by web research. In which allows for fitting to a continuous distribution. In figure 4.9(a) to figure 4.9(d), which corresponds to as-dried sample annealed at 200^0C, 400^0C and 600^0C respectively, a prominent doublet was observed at the central spectra. This doublet pattern arise from the relaxation of the Fe in Co-Zn ferrite, which has a relaxation time τ less than τ_L, which is the Larmer precession time of the nuclear magnetic moment. The doublet pattern indicates superparamagnetic behavior of the smaller sized particles in the absence of hyperfine interaction field. It was also observed that with increasing annealing temperature (particle size increase), the peaks become sharper due to the reduction in energy distribution with decreasing surface area.

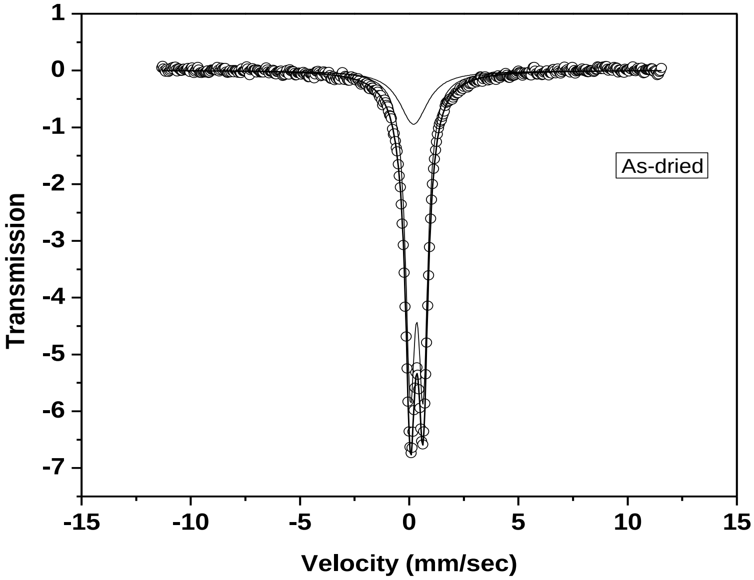

Figure 4.9 (a): Mössbauer spectra of $Co_{0.5}Zn_{0.5}Fe_2O_4$ in as-dried condition

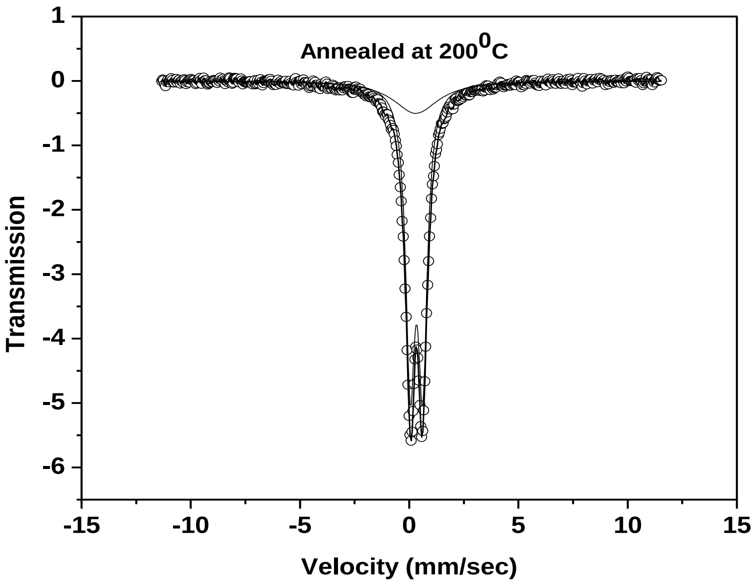

Figure 4.9 (b): Mössbauer spectra of $Co_{0.5}Zn_{0.5}Fe_2O_4$ annealed at 200^0C

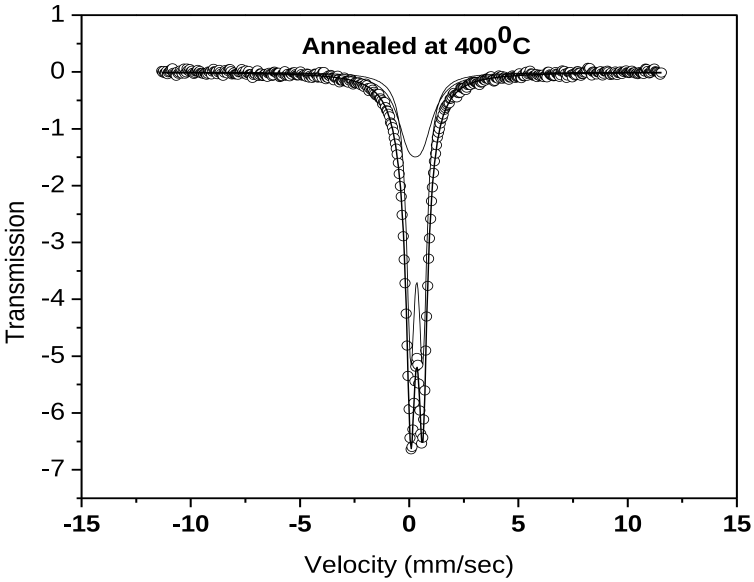

Figure 4.9 (c): Mössbauer spectra of $Co_{0.5}Zn_{0.5}Fe_2O_4$ annealed at 400^0C

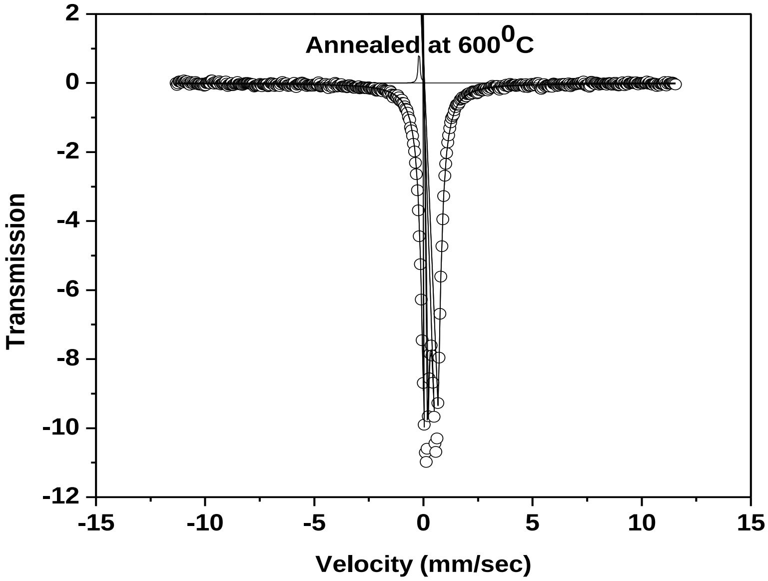

Figure 4.9 (d): Mössbauer spectra of $Co_{0.5}Zn_{0.5}Fe_2O_4$ annealed at 600^{0}C

Table: 4.3 Numerical values of Isomer shift (IS), Quadrupole Splitting (ΔE_q), Position of Fe3$^+$, Hyperfine field (H_{hf}) of $Co_{0.5}Zn_{0.5}Fe_2O_4$ nano particles annealed at different temperatures

$Co_{0.5}Zn_{0.5}Fe_2O_4$	**Sub site**	**Position of Fe^{3+}**	**Isomer Shift (IS) mm/sec**	**Quadrupole splitting (ΔE_q) mm/sec**	**Hyperfine field (H_{hf}) KG**	**Area %**
As-dried	1	B	0.345	0.586	0	0.800
	2	A	0.200	0.000	0	0.200
200^{0}C	1	B	0.333	0.569	0	0.813
	2	A	0.304	0.016	0	0.187
400^{0}C	1	A	0.278	0.357	0	0.357
	2	B	0.345	0.635	0	0.643
600^{0}C	1	A	0.342	0.508	0	0.954
	2	B	0.200	0.000	0	0.046

The various electronic and magnetic parameters such as Isomer shift, Quadruple splitting, Hyperfine field and relative area determine from the Mössbauer spectra are listed in the table 4.3. From the table 4.3, we observed that all sample have zero hyperfine field, which is a strong evident that all sample are in superparamegntic state. The cation distribution at tetrahedral (A) and octahedral (B) sites are presented on the table, which was calculated based on the relative area of the each species. The isomer shifts in the table is quoted relative to metallic iron at room temperature. The quadruple splitting in the superparamagnetic component indicates distorted co-ordination away from the perfect tetrahedral or octahedral symmetry. The quadruple splitting for Fe^{2+} is larger than that for Fe^{3+}; hence the Fe^{2+} does not exist in the composition. Also because the quadruple splitting in the low spin is lower than 0.8mm/s, Fe^{3+} in composition appears low spins. The central doublet may be attributed to the Fe^{3+} ions, which magnetically isolated and do participated in the long range number of nearest non-magnetic neighbor. For diamagnetically substituted ferrites, the existence of the central doublet superimposed on the well-resolved magnetic sextets. In the present system, the central doublet arise due to the magnetically isolated Fe^{2+} ions located at the tetrahedral sites rather than any secondary phase.

From the table 4.3 we can observe that up to the 600^0C there is no hyperfine field i.e the samples are in superparamagnetic state. Magnetic materials can generate heat in an alternating field. In superparamagnetic materials, the relaxation losses in single domain MNPs fall in to two modes A-sites and B-sites. Heat dissipation from the MNPs is caused by the delay in the relaxation of the magnetic vector through either the rotation within the particle that is called Neel relaxation or through the movement of the particles, which is called Brownian relaxation. When the particle are exposed to a magnetic field, the magnetic field reversal time shorter than the magnetic relaxation time of particles. Those from the above Mössbauer spectra it can be conclude that $Cu_{0.5}Zn_{0.5}Fe_2O_4$ nanoparticles annealed up to 600^0C would be most suitable for applications in magnetic particles hyperthermia.

4.4 Measurement of Hydrodynamic Diameter by Dynamic Light Scattering

Particle size analysis and aqueous dispersion stability of magnetic nanoparticles is an important factor for their utilization in various nano-bio applications. In order to investigate the hydrodynamic diameter of the chitosan coated $Co_{0.5}Zn_{0.5}Fe_2O_4$ magnetic nanoparticles a dynamic LASER scattering (DLS) system is used. It is worth to mention that the value of the particle diameter obtained from XRD means the particle core size, whereas the size detected using DLS system refers to a hydrodynamic diameter of particles, this diameter to obtain from comparing a sphere to translational diffusion coefficient actually measured. The hydrodynamic size, calculated from the diffusional properties of the particles is an indicative of the apparent size of the dynamic hydride particles [4.12]. For biomedical application the hydrodynamic diameter of should be the size less than 250 nm [4.13]

The DLS experiment was conducted at a constant temperature of 37^0C, which is the temperature of the body fluid. Figure 4.10 (a), 4.10 (b), 4.10 (c) and 4.10 (d)shows the size distribution of the chitosan bound $Co_{0.5}Zn_{0.5}Fe_2O_4$ nanoparticles at 1mg/ml, 2mg/ml, 4mg/ml and 6mg/ml particle concentration in 1% chitosan solution and each of those concentration was made by as-dried, 200^0C, 400^0C and 600^0C annealed nanoparticle. The shape of the curve clearly indicates that the particle size distribution is gradually rising with the increasing of annealing temperature of the nanoparticle. In the case of 1mg/ml concentration the diameter of the as-dried sample is found 171.3nm, which is 224.7nm for 600^0C annealed nanoparticle. The highest hydrodynamic diameter was found 233 nm for 6mg/ml sample annealed at 600^0C. This increasing diameter for the nanoparticle is due to the crystallite grain growth with the annealing temperature [4.14].

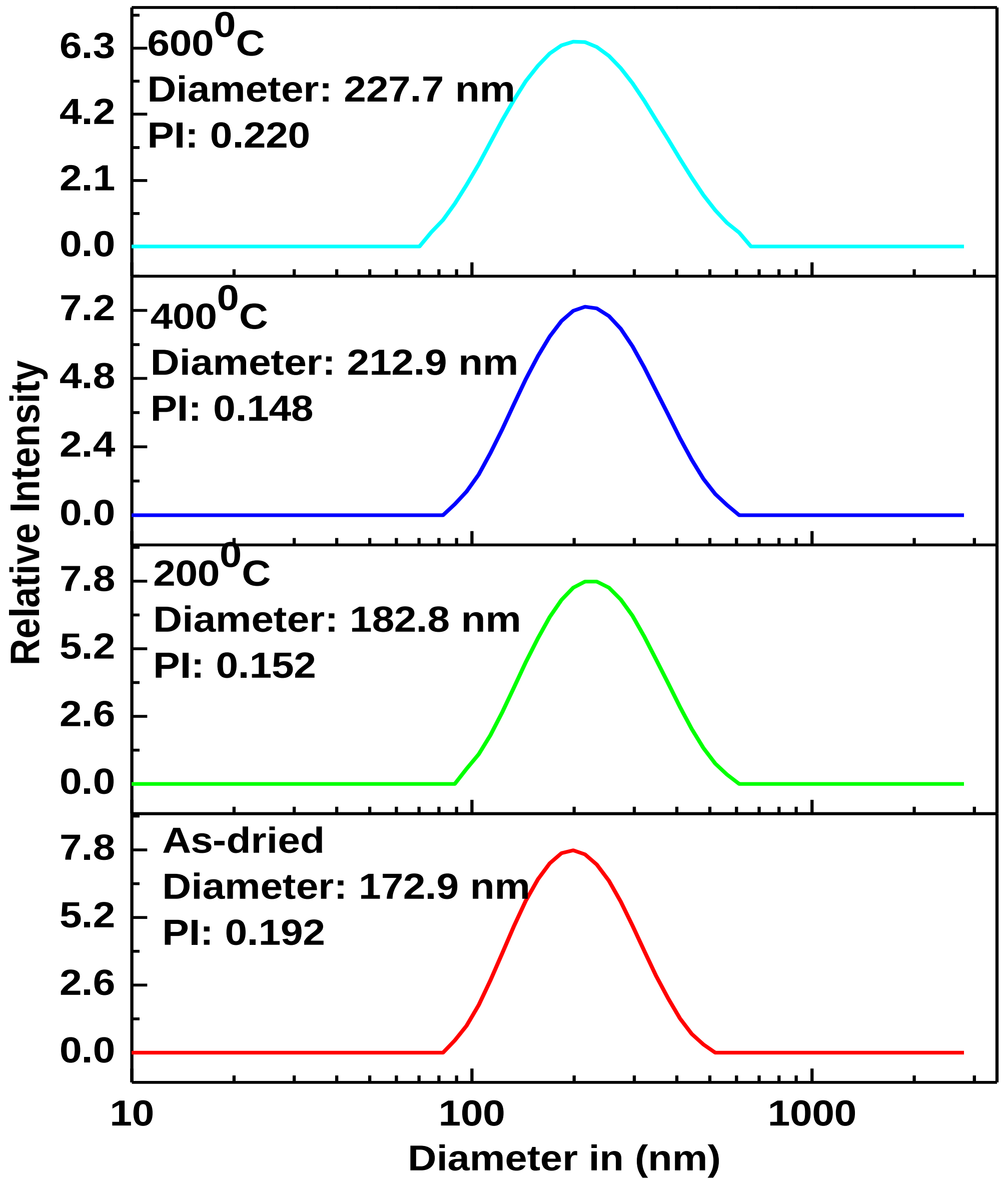

Figure 4.10 (a): Variation of the hydrodynamic diameter with annealing temperature of 6mg/mL chitosan coated nanoparticles

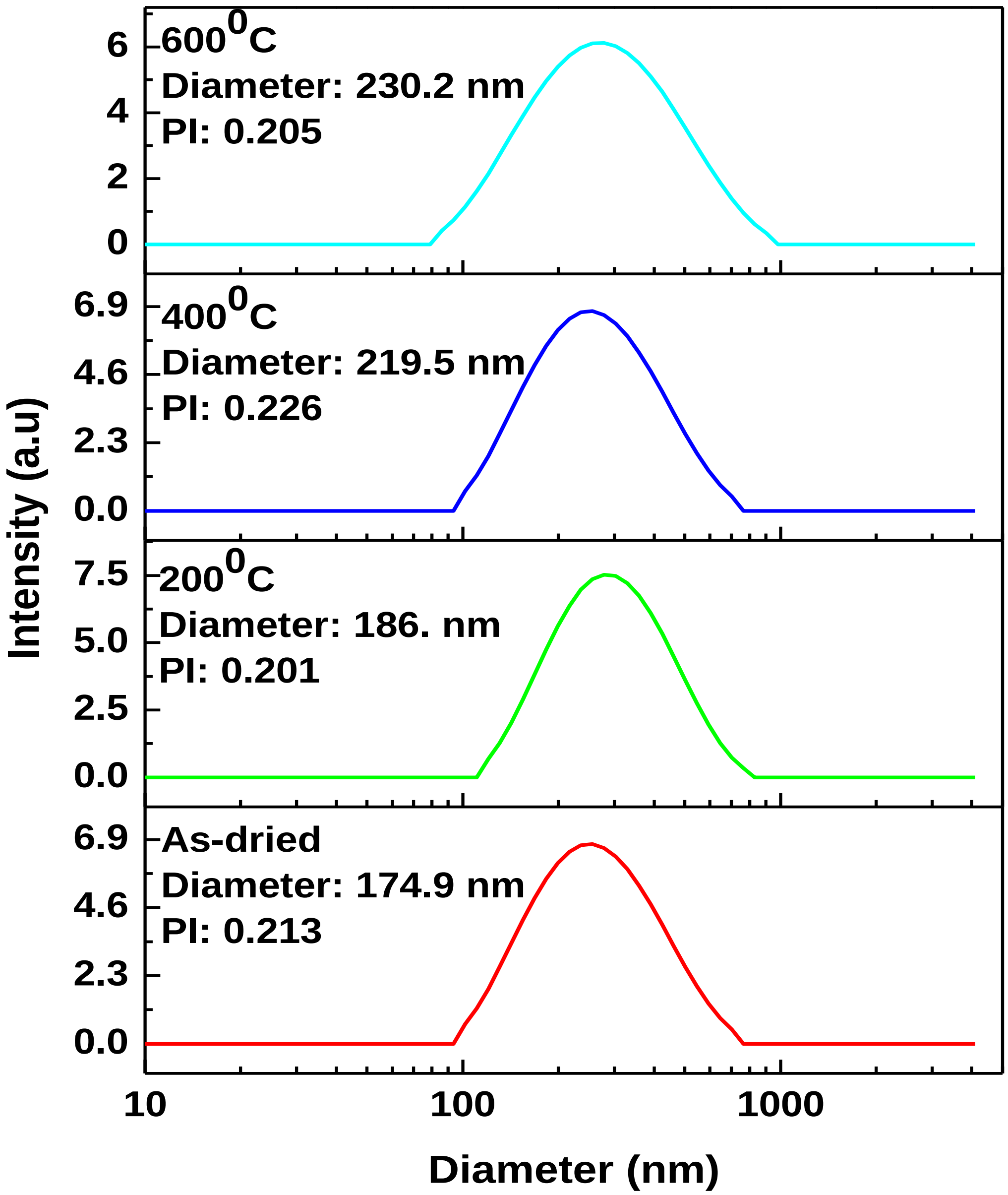

Figure 4.10 (b): Variation of hydrodynamic diameter with annealing temperature of 4mg/mL chitosan coated nanoparticles

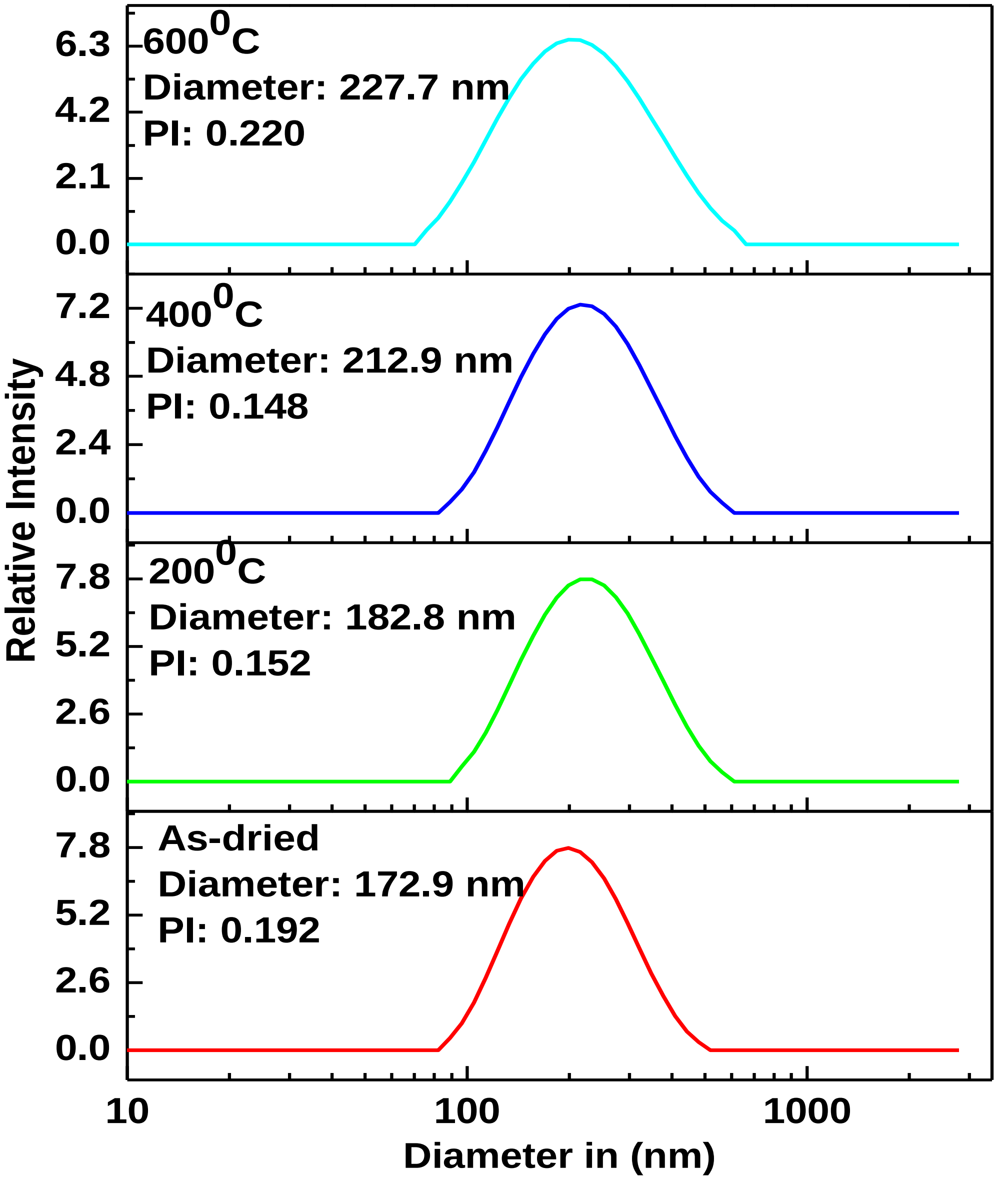

Figure 4.10 (c): Variation of the hydrodynamic diameter with annealing temperature of 2mg/mL chitosan coated nanoparticles

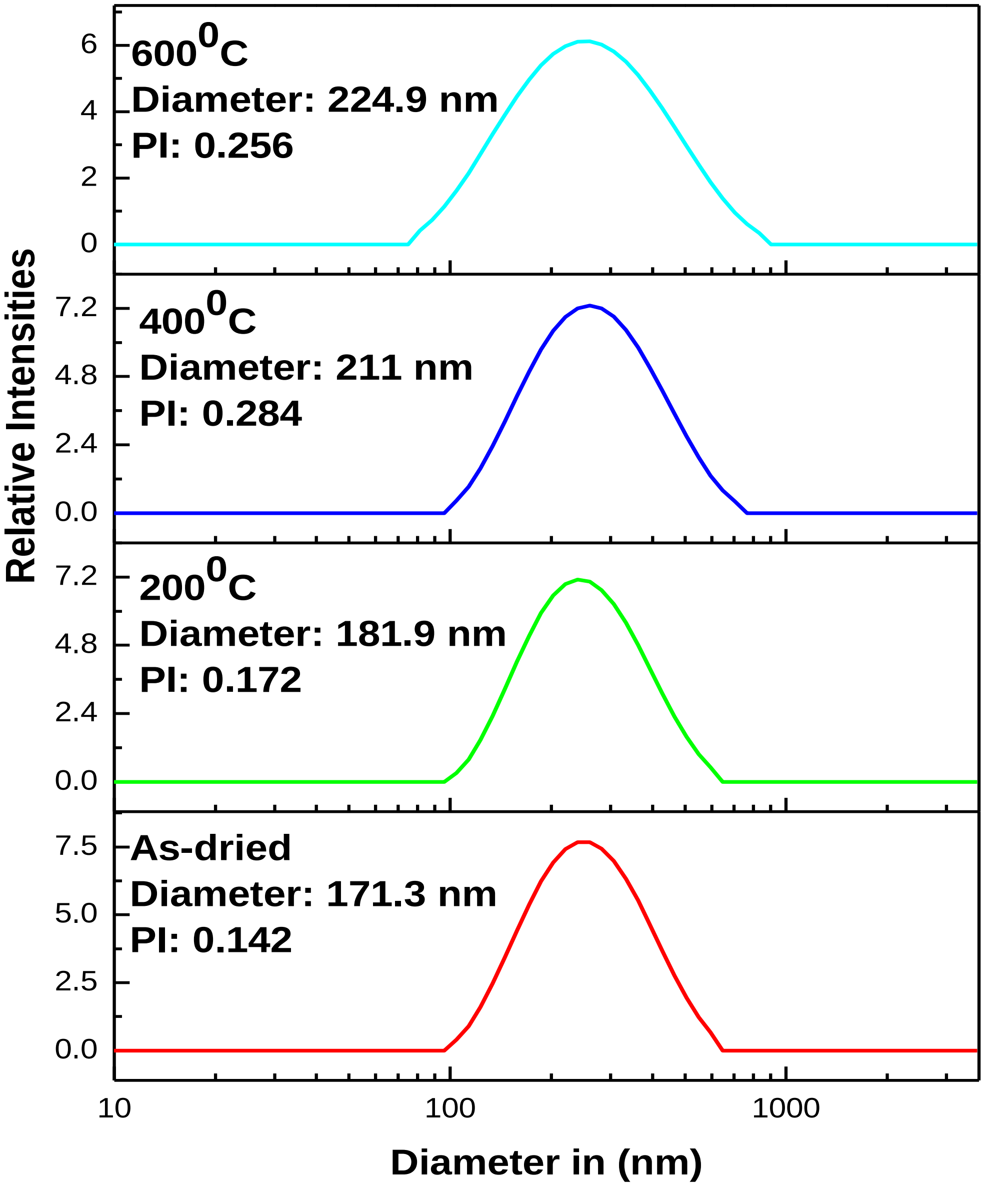

Figure 4.10 (d): Variation of the hydrodynamic diameter with annealing temperature of 1mg/mL chitosan coated nanoparticles

It is also to be noted that when the particle concentration increased the hydrodynamic diameter of the nanoparticle increased slightly. This result suggest that a strong dipole -dipole interaction of nanoparticles are getting self-agglomerated and showing a larger hydrodynamic diameter as compared to nanoparticles in lower concentration. [4.15]

In table 4.4, 4.5, 4.6 and 4.7 represent the numerical diameter and PI index for 1mg/ml, 2mg/ml, 4mg/ml and 6mg/ml nanoparticle concentration. And in table 4.8 enlisted the comparison of the diameter among the different particle concentration and their different annealing temperature. It is seen from the table PI values is almost constant and less than 0.3 which remark that the diameter of the nanoparticle are nearly homogenous. [4.16-4.17]

Table 4.4: Variation of diameter with annealing temperature for concentration 1mg/mL

Annealing Temperature (^{0}C)	DLS Particle diameter(nm)	PI
As-dried	171.3	0.142
200	181.9	0.172
400	211	0.284
600	224.9	0.256

Table 4.5: Variation of diameter with annealing temperature for concentration 2mg/mL

Annealing Temperature (^{0}C)	DLS Particle diameter(nm)	PI
As-dried	172.9	0.192
200	182.8	0.152
400	212.9	0.148
600	227.7	0.220

Table 4.6: Variation of diameter with annealing temperature for concentration 4mg/mL

Annealing Temperature (^{0}C)	DLS Particle diameter(nm)	PI
As-dried	174.9	0.213
200	186.5	0.201
400	219.5	0.226
600	230.2	0.205

Table 4.7: Variation of diameter with annealing temperature for concentration 6mg/mL

Annealing Temperature (^{0}C)	DLS Particle diameter(nm)	PI
As-dried	177	0.226
200	193.4	0.219
400	222.7	0.269
600	233.1	0.226

The table 4.8 summarized the effects on annealing temperature on different sample concentration of particle and on the particle diameter in nanometer.

Table 4.8: Comparison of the diameter of different particle concentrations

Sample Concentration	Hydrodynamic diameter in (nm)			
	600^{0}C	**400^{0}C**	**200^{0}C**	**As-dried**
1mg/ml	224.9	211	181.9	171.3
2mg/ml	227.7	212.9	182.8	172.9
4mg/ml	230.2	219.5	186.5	174.9
6mg/ml	233.1	222.7	193.4	177

It is found that the increasing annealing temperature is proportional to the increasing of the particles size and PI values are almost constant. The result showed all these annealed parameter could influenced on the DLS particle diameter of the nanoparticles. Due to the good biocompatibility of chitosan, these MNPs may be used to magnetic field assisted drug delivery, enzyme or cell immobilization, magnetic hyperthermia and many other industrial application.

4.5 Hyperthermia Study

The measurements of the temperature changes versus time for the chitosan coated $Co_{0.5}Zn_{0.5}Fe_2O_4$ nanoparticles were done in a magnetic field B=0.0006 T which oscillated at a frequency of f = 342 KHz. So the (H.f) of the system is 1.83×10^8 A/m.s which is less than the critical value 4.85×10^8 A/m.s that's indicate it can be apply in human body without any damage of living cell [1.18]. Figure 4.11 (a), 4.11 (b), 4.11 (c) and 4.11 (d) represent rf induction heating as a function of time for chitosan coated $Co_{0.5}Zn_{0.5}Fe_2O_4$ nanoparticles annealed at 600^{0}C, 400^{0}C, 200^{0}C and as dried sample and their four different concentrations.

As it can be seen from figure 4.11 (a), the sample with particle concentration 6mg/mL gave the highest temperature change with time. In the process of induction heating, for the concentrations of 6mg/mL and 4mg/mL rose quickly within the first five minutes, reached 46.2 and 42.1^{0}C, then the curves stabilized. But in the case of 2mg/mL and 1mg/mL samples, 20 min was needed to reach it stabilized temperature, which was noted 43.9^{0}C and 42.1^{0}C respectively. It can be seen that the heating efficiency increases with increases of the particle concentration [4.19- 4.20]. It can also be observed that the rise in temperature of the solution of 6mg/mL and 4ml/mL is in the range of proper hyperthermia temperature range 42-45^{0}C [4.21]. Though the concentration of 2mg/mL and 1mg/mL sample reached 43^{0}C, it takes approximately 20 and 50 minuet, it is too long time for reach this temperature for hyperthermia treatment.

Now in figure 4.11(b), shown the heating curve of nanoparticles were annealed at a temperature 400^{0}C and its different concentrations. It is found that the heating effects of 6mg/mL seemed better than the other concentrations. Take 42-45^{0}C for standard temperature for hyperthermia treatment, sample of concentration 6mg/mL needed 8 minuet to achieve this temperature, while the time needed for the concentration 4mg/mL and 2mg/mL was 15 minutes and 20 minutes respectively. On the other hand the maximum temperature reached by the sample of concentration 1mg/ml was 42.2^{0}C at 50 minutes.

Figure 4.11(c) represent the temperature vs time curve of the nanoparticle annealed at 200^{0}C. From here it can be seen the sample of concentration 2mg/mL and 1 mg/mL, the rise in temperature were about 39.5^{0}C and 38.5^{0}C respectively. Which is considerate as a small temperature for hyperthermia treatment. But in the case of concentrations 6mg/mL and 4mg/mL, it was found that the temperature rise moderately and reached its platonic value approximately 42^{0}C and 41^{0}C after 15 minutes.

Finally figure 4.11 (d) represent the induction heating curve of different concentrations of as-dried sample. From here it has been found that none of the concentrations able to rise temperature more than 40^{0}C, which is bit low temperature for use in hyperthermia applications.

Finally the rise in temperature of the Co-Zn ferrite nanoparticles caused by induction heating depends upon several factors. The temperature induced by induction heating is moderate for $Cu_{0.5}Zn_{0.5}Fe_2O_4$ and their heating properties studied result by varying their concentration as shown in the figure 4.11(a) to figure 4.11(d). It can also be observed that the samples annealed at 600^0C and 400^0C of concentration 6mg/mL and 4mg/mL showed a prominent result for application in magnetic hyperthermia. Under the condition cancerous cells are killed described above, samples 6mg/mL and 4mg/mL annealed at 600^0C and 400^0C attain the desired time and temperature.

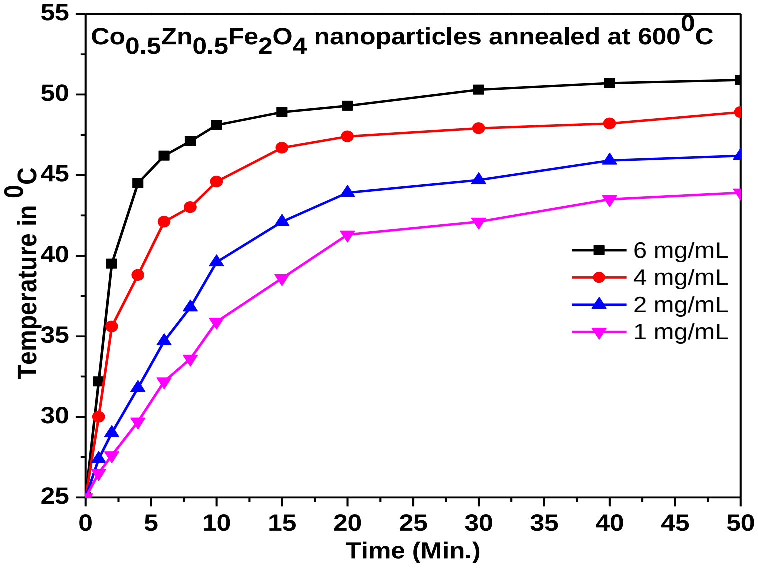

Figure 4.11(a): Temperature kinetic curve of 600^0C annealed chitosan coated $Co_{0.5}Zn_{0.5}Fe_2O_4$ MNPs at different concentrations

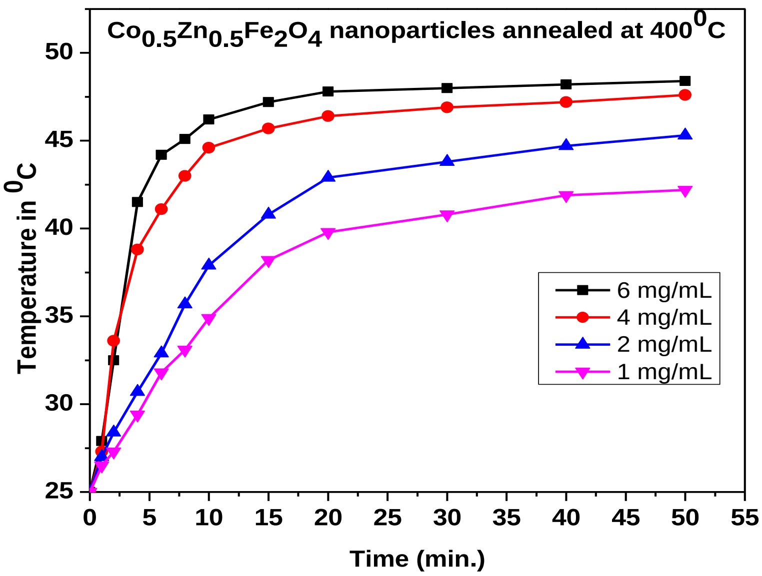

Figure 4.11(b): Temperature kinetic curve of 400^0C annealed chitosan coated $Co_{0.5}Zn_{0.5}Fe_2O_4$ MNPs at different concentrations

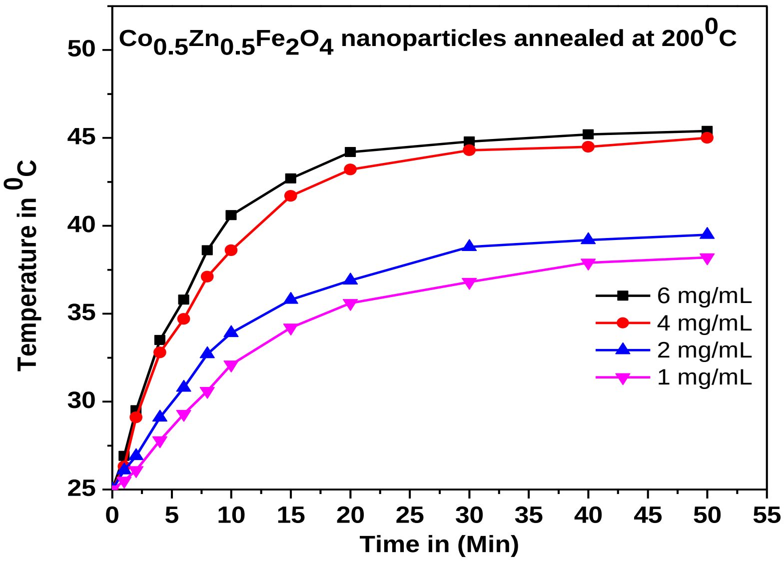

Figure 4.11(c): Temperature kinetic curve of 200^0C annealed chitosan coated $Co_{0.5}Zn_{0.5}Fe_2O_4$ MNPs at different concentrations

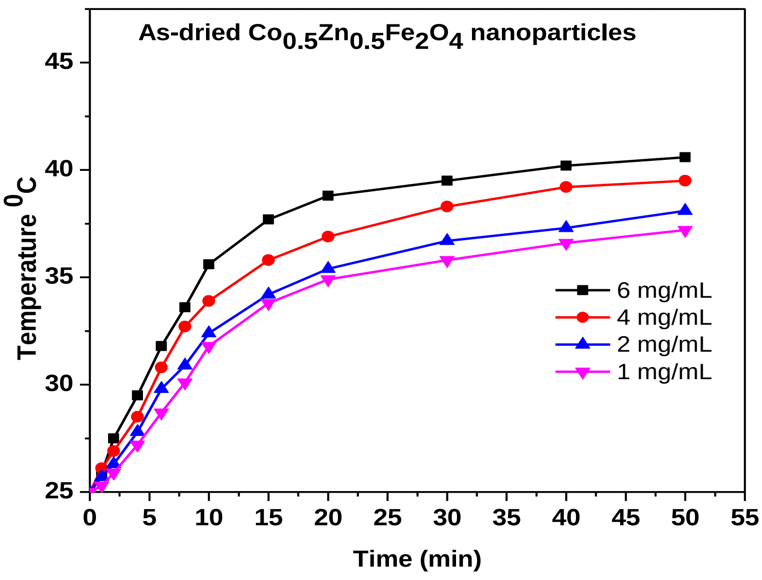

Figure 4.11(b): Temperature kinetic curve of as-dried chitosan coated $Co_{0.5}Zn_{0.5}Fe_2O_4$ MNPs at different concentrations

It is noted that from the above four curves in this section, with rising the annealing temperature, the induction temperature of each sample also rise. Which might be due to the rise of particle size of the sample [4.22-4.24].

CONCLUSION AND OUTLOOK

5.1 Conclusions

Nano-sized ferrite with composition $Co_{0.5}Zn_{0.5}Fe_2O_4$ nanoparticles have been successfully synthesized by a low temperature, high purity and easily reproducible chemical co-precipitation route. The samples were annealed at 200^0C, 400^0C, 600^0C, 800^0C and 1000^0C temperature and coated with 1% chitosan solution. The as-prepared and annealed samples have been detailed investigated by various experimental technique such as XRD, VSM, Mossbauer Spectroscopy, and DLS. Finally, fluid hyperthermia effect of chitosan coated nanoparticle have been studied.

Through the structural analysis, performed by XRD, it has been confirmed that, as-prepared and annealed MNPs have single phase polycrystallinity with clear diffraction patterns. It has been observed that the width of the diffraction peaks shrank as the annealing temperature increases, which might be increase in grain size of ferrite. It was also found that the crystal size of the nanoparticles increased from approximately 7nm to 25nm with the increases of annealing temperature.

The hysteresis loops obtained from magnetic measurements using VSM showed that soft paramagnetic nature of the as-prepared and annealed samples. The maximum magnetization of the Co-Zn ferrite nanoparticles was strongly size dependent and varied from 29 emu/gm to 56 emu/gm when the grain size was increased from 7nm to 25nm respectively. The coercivity of the MNPs was also studied as a function of particle size. Coercivity of the samples in nanolevel is nearly small, which is suggestive of superparamagnetic behavior at room temperature. The behavior of $\frac{M_r}{M_s}$ indicates that at room temperature a considerable amount nanoparticles are still superparamagnetic in the absence of external applied magnetic field. The pattern of the magnetization showed as change of the annealing temperature particle size of the nanoparticle changes and surface area to volume ratio also changes, henceforth the magnetization changes. The magnetic properties were also studied by Mossbauer spectroscopy. The central doublet patterns were observed up to annealing temperature 600^0C and there is no hyperfine field confirmed the superparamagnetic nature of nanoparticles. Mossbauer spectroscopy it can be concluded that $Co_{0.5}Zn_{0.5}Fe_2O_4$ nanoparticles annealed up to 600^0C could be most suitable for application in magnetic particle hyperthermia.

The DLS technique has been reviled that the hydrodynamic diameter of the chitosan coated nanoparticles vary from 171nm to 233nm and PI index was less than 0.3. The diameter of the coated particles were found to be increased with the annealing temperature and the particle concentrations. It would be worthy to note that all samples annealed less than 600^0C have hydrodynamic diameter less than 300nm and PI index is less than 0.3. Which might be suitable of in vivo biomedical applications.

The main aim of this thesis was to investigate hyperthermia effects of $Co_{0.5}Zn_{0.5}Fe_2O_4$ nanoparticle. It has been seen that the samples with particle concentrations 6mg/ml and 4 mg/ml (annealed at 600 and 400^0C) shows best result. When placed in an induction coil those sample gives a temperature rise approximately 42^0C to 46^0C from the room temperature within 5 minutes. So those sample can be used as a hyperthermia application on cancer therapy. However, the heat power generated by the other sample would not be satisfactory for a given amount to rise a human body temperature by $5\text{-}6^0C$ ($42\text{-}44^0C$), which is necessary to destroy cancer cells.

5.1 Future Work

This thesis has attempted to cover the synthesis, characterization of $Co_{0.5}Zn_{0.5}Fe_2O_4$ nanoparticles and its application on magnetic hyperthermia therapy, however there are still many different areas which could be further developed.

Further research could be used to demonstrate the application of magnetic nanoparticles in other area such as magnetic drug delivery, MRI and data storage device. A full study focusing more specifically on hyperthermia measurements could look into a wider range of zinc doped samples in order to quantify effect with respect to the anisotropy changes. Another potential problem for use of cobalt is the toxicity nature of cobalt. If the materials was to be used I human trials, it would be imperative that no leaching of toxic cation into the body. It is possible through the use of coating agent. So much research is needed to improve the capping agent for nanoparticles. Despite the advantages of hyperthermia as a cancer therapy much research is needed to be use it in human body.

REFERANCES

CHAPTER I

[1.1] Weiss, P. S., 2012, "New Tools Lead to New Science". ACS Nano, Vol. 6, pp.1877–1879.

[1.2] Einstein A, 1956, "Investigation on the theory of Brownian movement". New York Dover Publication Inc., ISBN 0486603040.

[1.3] Huxford R. C, Della R. J, and Lin W., 2010, "Metal-organic frameworks as potential drug carriers". Current Objnon Chemical Biology, Vol. 14, pp. 262-268.

[1.4] Ethiraj A. S., Hebalkar N., Kharraz S., Urban J., Sainker S., and Kulkarni S., 2005, "Photolumincescent core-shell particles of organic dye in silice". Journal of Luminescence, Vol. 114, pp. 115-23.

[1.5] Bakuzis A., Pereira A., Santos J., and Morais P., 2006, "Superexchange coupling on oleysarcogine-cobalt magnetic nanoparticles". Journal of applied physics, Vol. 99, pp. 08C301-08C301-3.

[1.6] Bocanegra D. A., Mohallem N. D. S., Novak M. A., and Sinisterra R. D., 2004, "Preparation of ferrofluid from cyclodextrin and magnetite". Journal of Magnetism and Magnetic Materials, Vol. 272, pp. 2395-2397.

[1.7] Gilmore K., Idzerda Y. U., Klem M. T., Allen M., Douglas T. and Young M., 2005, "Surface contribution to the anisotropy energy of spherical magnetic particle". Journal of applied physics, Vol. 10, pp. 301-3.

[1.8] Burry C. C., Wells S. Chares S., Curtis D. S, 2003, "Dextran and albumin derivatised ironoxide nanoparticle: influence on fabrication in vitro". Biomaterials, Vol. 22, pp. 4551-4557.

[1.9] Mahmoudi M., Simchi A., Imani M., Slokrgozar A. M., Milani A. S., Hatle U. O., 2010, "A new approach for the invitro identification of the cytoxicity of superparamagnetic iron oxide nanoparticles". Colloids surt B Biointerfuces, Vol. 75, pp. 300-309.

[1.10] De M., chosh P. S., Rotello V. M., 2008, Advanced Materials, Vol. 20, pp. 1-4.

[1.11] Pankhurst Q. A., Connolly J., Jones S. K. and Dobson J. 2003 "Applications of magnetic nanoparticles in biomedicine", J. Phys. D: Appl. Phys. Vol. 36, pp.167-181.

[1.12] Akbarzadesh A., Samici M., Davarna S., 2012, "Magnetic nanoparticles: preparation, physical properties and applications in biomedicine" Nanoscale Research latter, Vol.144, pp.1-13.

[1.13] Vaidyanathan G, Sendhilnathan S. 2008, "Characterization of $Cd_{1-x}Zn_xFe_2O_4$ nanoparticales synthesized by co-precipitation method". Phys B Condens Matter Vol.403, pp.2157-67.

[1.14] Wilson M. W., Kerlan R. K. Jr., Fidelman N. A., Venook A. P., Laberge J. M., Koda J., and Gordon R. L., 2004, "Hepatocellular Carcinoma: Regional therapy with a magnetic targated carrier bound to doxorubicin in a dual MR imaging/ conventional angiography suite: Initial experience with four patients". Radiology, Vol. 230, pp. 287-293.

[1.15] Pankhurst Q. A., Connolly J., Jones S. K. and Dobson J. 2003, "Applications of magnetic nanoparticles in biomedicine". J. Phys. D: Appl. Phys. Vol.36, pp.167-181.

[1.16] Liberti P A, Rao C G, and Terstappen. 2001, "Optimization of ferrofluids and protocols for the enrichment of breast tumor cells in blood". J. Magn. Magn. Mater.Vol. 225, pp. 301–307.

[1.17] Paul F, Melville D, Roath S and Warhurst D. 1981, "A bench top magnetic separator for malarial parasite concentration". IEEE Trans. Magn. MAG-17 2822–4.

[1.18] Seesod N, Nopparat P, Hedrum A, Holder A, Thaithong S, Uhlen M and Lundeberg J. 1997, "An integrated system using immunomagnetic separation, polymerase chain reaction, and colorimetric detection for diagnosis of Plasmodium Falciparum". Am. J. Tropical Med. Hygiene, Vol. 56, pp. 322–8.

[1.19] Hofmann W. K, Vos S, Komor M, Hoelzer D, Wachsman W and Koeffler H. P. 2002, "Characterization of gene expression of CD34+ cells from normal and myelodys plastic bone marrow blood". Vol. 100, pp. 3553–3560.

[1.20] Delgratta C., Dellapenna S., Battista P., Didonato L., Vitullo P., Romani G. and Diluzio S, 1995, " Detection and counting of specific cell populations by means of magnetic markers linked to monoclonal antibodies". Phys. Med. Biol. Vol. 40 pp.671–681.

[1.21] Edelstein R L, Tamanaha C R, Sheehan P E, Miller M M, Baselt D R, Whitman L J and Colton R J. 2000, "The BARC biosensor applied to the detection of biological warfare agents". Biosensors Bioelectron. Vol.14, pp. 805–13.

[1.22] Alexiou C, Arnold W, Klein R J, Parak F G, Hulin P, Bergemann C, Erhardt W, Wagenpfeil S and Lubbe A S, 2000, “ Locoregional cancer treatment with magnetic drug targeting”. Cancer Res. Vol. 60, pp. 6641–8.

[1.23] Hans M L and Lowman A M. 2002, “Biodegradable nanoparticles for drug delivery and targeting Curr. Opin.”. Solid State Mater. Sci. Vol. 6, pp. 319–327.

[1.24] Lubbe A S, Bergemann C, Brock J and McClure D G. 1999, “Physiological aspects in magnetic drug-targeting”. J. Magn. Magn. Mater. Vol. 194 pp.149–155.

[1.25] Hafeli U O and Pauer G J, 1999, “In vitro and in vivo toxicity of magnetic microspheres”. J. Magn. Magn. Mater. Vol. 194 pp.76–82.

[1.26] Hrushikesh M., Yen P. L, Mohammed A, Prasad P. V., Elise A. Schultz S., Robert E, Thomas M, and Vinayak P. Dravid, J. 2009, Phys. Chem., Vol.113, pp.17761-17767.

[1.27] Hoque S. M., Tariq M., Liba S., Salehin F., Mahmood Z. H., Khan M. N. I., Chattopadhayay K., Islam R., Akter S. 2016, “Thermo-therapeutic application of chitosan and PEG coated $NiFe_2O_4$ nanoparticles”. Nanotechnology, Vol.27, 285702(10pp).

[1.28] Ghasemian Z., Gahrouei S. D., Manouchehri S., 2015, “Cobalt Zinc Ferrite nanoparticles as a potential magnetic resonance imaging agent: An in vitro study”. Avicenna J Med Biotech, Vol. 7, pp. 64-68.

[1.29] Koo Y. E., Reddy G. R., Bhojani M., Schneider R., Philbert M. A., Recbembulta A., Ross B. D., Kopelman R., 2006, Adv. Drug Del. Rev., Vol. 58, pp. 1556.

[1.30] Sun C., Reisch O., Gunn J., Fang C., Hansen S., Lee D., Sze R., Ellenborge R. G., Olson J., Zhang M., 2008, Small 4, pp. 372.

[1.31] Hrushikesh M., Yen P. L, Mohammed A, Prasad P. V., Elise A. Schultz S., Robert E, Thomas M, and Vinayak P. Dravid, 2009, J. Phys. Chem., Vol.113, pp.17761-17767.

[1.32] Hoque S. M., Tariq M., Liba S., Salehin F., Mahmood Z. H., Khan M. N. I., Chattopadhayay K., Islam R., Akter S. 2016, “Thermo-therapeutic application of chitosan and PEG coated $NiFe_2O_4$ nanoparticles”. Nanotechnology, Vol.27, 285702(10pp).

[1.33] Habib A. H., Ondeck C. L, Chaudhary P. Bockstaller R. M, McHenry E. M. 2008, “Evaluation of iron-cobalt/ferrite core-shell nanoparticles for cancer thermotherapy”. J. Phys. D: Appl. Phys.; Vol. 103, pp.07A307.

[1.34] Li X., Wang L., Fan Y., Feng D., and Cui F. Z., 2012 “Biocompatibility and Toxicity of nanoparticles and nanotubes”. Journal of Nanomaterials, pp. 1-9

[1.35] Shokrollahi H., Shokrollahi K. 2007, “Influence of additives on the magnetic proper ties, microstructure and densification of Mn–Zn soft ferrites”. Materials Science and Engineering: B Vol. 141, pp. 91–107.

[1.36] Shokrollahi H. 2008, “Magnetic properties and densification of Manganese–zinc soft ferrites ($Mn_{1-x}Zn_xFe_2O_4$) doped with low melting point oxides”. Journal of Magnetism and Magnetic Materials, Vol. 320, pp. 463–474.

[1.37] Saafan S.A., Assar S.T., Moharram B.M., El Nimr M.K. 2010, “Comparison study of some structural and magnetic properties of nano-structured and bulk Li–Ni–Zn ferrite samples”. Journal of Magnetism and Magnetic Materials, Vol. 322, pp.628–632.

[1.38] X. Lu, G. Liang, Q. Sun, C. Yang, 2011, “High-frequency magnetic properties of Ni–Zn ferrite nanoparticles synthesized by a low temperature chemical method Materials Letters”. Vol. 65, pp. 674–676.

[1.39] Zhou B., Liu Z. Wang X., Sui Y, Huang Z.L., W.Su. 2010, “EffectofSiO2coating on the magnetic properties of Ni–Zn ferrite”. Physica B: Condensed Matter, Vol. 405, pp. 374–378.

[1.40] Rohilla S., Kumar S., Aghamkar P., Sunder S., Agarwal A., 2011 “Investigations on structural and magnetic properties of cobalt ferrite/silica nanocomposites prepared by the coprecipitation method”. Journal of Magnetism and Magnetic Materials, Vol. 323, pp. 897–902.

[1.41] Hork, D. Rittich B., Spanov A., D.Hora k, Spanova A. 2007, “Carboxyl-functionalized magnetic microparticle carrier for isolation and identification of DNA in dairy products”. Journal of Magnetism and Magnetic Materials, Vol. 311, pp. 249–254.

[1.42] Tomitaka A., Koshi T., Hatsugai S., Yamada T., Takemura Y. 2011, “Magnetic characterization of surface-coated magnetic nanoparticles for biomedical application”. Journal of Magnetism and Magnetic Materials, Voll. 323, pp. 1398–1403.

[1.43] Pollert E., Veverka P., Veverka M., Kaman O., Zveta K., Vasseur S., Epherre R., Goglio G., Duguet E., Zaveta K. 2009, “Search of new core materials for magnetic fluid hyperthermia: preliminary chemical and physical issues". Progress in Solid State Chemistry, Vol. 37, pp. 1–14.

[1.44] Vaidyanathan G., Sendhilnathan S. 2008, "Characterization of Co_{1-x} Zn_x Fe_2O_4 nano-particles synthesized by co-precipitation method". Physica B: Condensed Matter, Vol. 403, pp. 2157–2167.

[1.45] Sharifi I., Shokrollahi H., Amiri S. 2012 "Ferrite-based magnetic nanofluids used in hyperthermia applications". Journal of Magnetism and Magnetic Materials, Vol. 324, pp. 903–915.

[1.46] Pankhurst Q. A., Connolly J., Jones S. K. and Dobson J. 2003, "Applications of magnetic nanoparticles in biomedicine", J. Phys. D: Appl. Phys. Vol.36, pp.167-181.

[1.47] Akbarzadesh A., Samici M., Davarna S. 2012, "Magnetic nanoparticles: preparation, physical properties and applications in biomedicine" Nanoscale Research latter, Vol.144, pp.1-13.

[1.48] Vaidyanathan G., Sendnilnath S., 2008, "Characterization of $Cd_{1-x}Zn_xFe_2O_4$ annoparticles synthesized by co-precipitation method". Phys. B. condens. Matter, Vol. 403, pp. 2157-67.

[1.49] Nouri A., Zamanian A., Kazemzadeh A., Bahrevar M.A., Ali-Ramaji Sh, Sohrabi Z., 2014, "Synthesis and characterization of cobalt zinc ferrite-chitosan core-shell nanoparticles". International Materials Physics Journal, Vol. 2(4), pp. 16-20.

[1.50] Abdulsamee F. Abdulaziz, Khalaf I. Khaleel1, Nabeel A. Bakr. 2011, "Magnetic and magnetostrictive properties of $Co_{1-x}Zn_xFe_2O_4$ nanoparticles produced by co-precipitation method". Tikrit Journal of Pure Science, Vol. 16(4), pp. 216-222.

[1.51] Vinuthna Ch., Ravinder D., Madhusudan Raju R. 2013, "Characterization of $Co_{1-x}Zn_xFe_2O_4$ Nano Spinal Ferrites Prepared by Citrate Precursor Method". Int. Journal of Engineering Research and Applications, Vol. 3(6), pp. 654-660.

[1.52] Daryoush S. G., Zeinab G., Mohammad A., Sohrab M., Shaghayegh J. and Nasim D. 2013, "In vitro Evaluation of Cobalt-Zinc Ferrite Nanoparticles Coated with DMSA on Human Prostate Cancer Cells". J Mol Biomark Diagn., Vol. 5, doi:10.4172/2155-9929.1000154.

[1.53] Ibrahim S., Shokrollahi H. 2012, "Nanostructural, magnetic and Mossbauer studies of nanosized $Co_{1-x}Zn_xFe_2O_4$ synthesized by co-precipitation". Journal of Magnetism and Magnetic Materials, Vol. 324, pp. 2397–2403.

[1.54] Hochepied J. F. and Pileni M. P. 2000, “Magnetic properties of mixed cobalt–zinc ferrite nanoparticles”. J. Appl. Phys., Vol. 87, pp. 2472-2478.

[1.55] J. Lopeza, L.F. Gonzalez-Bahamonb, J. Prado,, J.C. Caicedo, G. Zambrano, M.E. Gomeza, J. Esteve, P. Prieto. 2012, “Study of magnetic and structural properties of ferrofluids based on cobalt–zinc ferrite nanoparticles”. Journal of Magnetism and Magnetic Materials, Vol. 324, pp. 394–402.

[1.56] Mamani J.B., Costa-Filho A.J., Cornejo D.R., Vieira E.D., Gamarra L.F., 2013, “Synthesis and characterization of magnetite nanoparticles coated with lauric acid”. Materials Characterization, Vol. 81, PP. 28–36.

[1.57] Nadeem K., Shahid M., Mumtaz M. 2014, “Competing crystallite size and zinc concentration in silica coated cobalt ferrite nanoparticles”. Progress in Natural Science: Materials International, http://dx.doi.org/10.1016/j.pnsc.2014.05.011

[1.58] M. Veverkaa, P. Veverka, Z. Jira ́k, O. Kaman, K. Knızek, M. Marysko, E. Pollert ,K.Zaveta, 2010, “Synthesis and magnetic properties of $Co_{1-x}Zn_xFe_2O_4$ gnanoparticles as materials for magnetic fluid hyperthermia”. Journal of Magnetism and Magnetic Materials, Vol. 322, pp. 2386–2389.

[1.59] Akmal M., Mushtaq M, Iqbal M and Zahra R. 2013, “Synthesis of spiral and reverse spiral Co-ferrite by co-precipitation method and XRD Characterization”. IJCBS, Vol. 4, pp. 66-71.

[1.60] Raghvendra S Y, Jaromir H, Miroslav H, Pavol Š. 2015, “Magnetic properties of $Co_{1-x}Zn_xFe_2O_4$ spinel ferrite nanoparticles synthesized by starch-assisted sol–gel autocombustion method and its ball milling”. Journal of Magnetism and Magnetic Materials, Vol. 378, pp.190–199.

[1.61] Ritu R, Sangeeta T and Singh M. 2011, “Processing and Characterization of Cobalt-Zinc Nano Ferrite”. AIP Conf. Proc. Vol.1349, pp.287-288.

[1.62] Sohrab M, Zeinab G, Daryoush S-G, Mohammad A, 2013, “Synthesis and characterization of cobalt-zinc ferrite nanoparticles coated with DMSA”. ChemXpress, Vol. 2(3), pp. 147-152.

[1.63] Singhal S, Namgyal T, Bansal S, Chandra K. 2010, “Effect of Zn Substitution on the Magnetic Properties of Cobalt Ferrite Nano Particles Prepared Via Sol-Gel Route”. J. Electromagnetic Analysis & Applications, Vol. 2, pp. 376-381.

[1.64] Sundararajan M., John Kennedy L., and Judith Vijaya J. 2015, “Synthesis and Characterization of Cobalt Substituted Zinc Ferrite Nanoparticles by Microwave Combustion Method”. J. Nano sci. Nanotechnol. Vol. 15, pp. 6719-6729.

[1.65] Zui Ding, WeiWang, SizhuWu, and J. Ping Liu, 2015, “Synthesis and Characterization of Co–Zn Ferrite Nanoparticles by Hydrothermal Method: A Comparative Study”. IEEE TRANSACTIONS ON MAGNETICS, Vol. 51, pp.11.

CHAPTER II

[2.1] Milde P., Kohler D., Seidel J., L.M. Eng, Bauer A., Chason A, , Kindervater J., S., Muhlbauer C. Pfleiderer, Buhrandt S., Schutte C., and Rosch A., 2013, “Unwinding of a Skyrmion Lattice by Magnetic Monopoles”. Science, Vol.340, pp. 6136.

[2.2] Getzlaff M., 2008, “Fundamentals of Magnetism, Springer-Verlag, Berlin-Heidelberg”.

[2.3] Gerber R., 1994, “Magnetic separation seperation Applied Magnetism ed G. Asti (Dordrecht: Kluwer), pp. 165-220.

[2.4] Zborowsk M., 1997, “Physics of magnetic cell sorting scientific and clinical application of magnetic carriers”. New York plenum, pp. 205-31.

[2.5] Hatch G. P., and Stelter R. E., 2001, “Magnetic design considerations for devices and particles used for biomedical high-gradient magnetic separation (HGMS) systems”. J. Magn. Mag. Matter., Vol. 225, pp. 262-76.

[2.6] Maggi, R. Bigi, F. Carloni, S. Mazzacani, A. Sartori, G., 2001, Green chemistry, Vol.3, pp.173-174.

[2.7] Cornell, R. M. Schwertmann, U., 2003, ‘The Iron Oxides: Structure, Properties, Reactions, Occurrences and Uses”. Second Edition, Wiley-VCH, Weinheim.

[2.8] Morrish A. H., 2001, “The physical properties of magnetism”. New York: IEEE Press.

[2.9] Berry C. C. and Adam S G, 2003, J. Phys. D. Appl. Phys. Vol.36, pp. R198.

[2.10] Weiss P., J. de Phys. Rad. Vol. 6, pp. 661, 1907.

[2.11] Handley R. C. O, 2000, “Modern Magnetic Materials: Principles and applications”. John Wiley & Sons.

[2.12] Chikazumi S., 1999, “Physics of Ferromagnetism, Oxford University Press”. New York.

[2.13] Néel L., Ann. 1949, Geophys.Vol. 5, pp.99.

[2.14] Brown W. F., 1963, Jr., Phys. Rev. Vol. 130, pp.1677.

[2.15] Laurent S., Forge D., Port M., Roch A., Robic C., Elst L. V., Muller R. N., 2008, Chem. Rev., Vol. 108, pp. 2064.

[2.16] Johansson, C. 1993, “Magnetic studies of magnetic liquids – Doctoral thesis”. Chalmers University of Technology and University of Göteborg.

[2.17] Prieto-Astalan, Brownian A. 2007, “Relaxation Measurements of Magnetic Nano-particles: Towards the Development of a Novel Biosensor System – Licentiate thesis”. Chalmers University of Technology, Göteborg.

[2.18] Fannin P. C., Scaife B. K. P., Charles S. W. 1987, J. Magn. Magn. Mater. Vol. 65, pp. 279.

[2.19] Daliya S. Mathew, Ruey-Shin Juang, 2007, Chem. Engin . J, Vol. 129, pp. 51.

[2.20] LaMer V. K, R. Dinegar H., 1950, J. Am. Chem. Soc. Vol. 72, pp. 4847–4854.

[2.21] LaMer V. K, R. Dinegar H., 1950, J. Am. Chem. Soc. Vol. 72, pp. 4847–4854.

[2.22] Kwon S. G., Piao Y., Park J., Angappane S., Y. Jo, Hwang N.-M., Park J.-G., T., Hyeon, 2007, J. Am. Chem. Soc., Vol. 129, pp. 12571–12584.

[2.23] Madros G., McCoy B. J., 2002, J. Chem. Phy., Vol. 117, pp. 8042.

[2.24] Sugimoto T., 1987, Adv. Colloid Interface Sci., Vol. 28, pp. 65.

[2.25] Beattie J. K., 1989, Pure and Appl. Chem., Vol. 61(5), pp. 937.

[2.26] Van Embden J., Sader J. E., Davidson M., Mulvaney P., 2009, J. Phys. Chem. C, Vol. 113, pp. 16342–16355.

[2.27] Granqvist, Buhrman, 1976, “Ultrafine metal particles”. Journal of Applied Physics, Vol. 47, pp. 2200-2219.

[2.28] Birringer R, Gleiter H, Klein S P and Marquardt, 1984 P;, Phys. Lett. Vol. 365, pp. A102.

[2.29] Kear,B.H. and Strutt P. R ,1995, Nanostruct. Matter, 6, 227

[2.30] Oda K, Misumi Y, Ikehara Y, Stephen O, Brennan, Hatsuzawn K, Nakayama K, 1992, Biochemical and Biophysical research communications, Vol. 189, pp 1353-1361

[2.31] Saburo I, Kenji H and Tetsuya A. 1982 “Ultrafine powders of TiN and Mn produced by a reactive gas evaporation”. Journal of Crystal Growth, Vol. 56, pp. 265-269.

[2.32] Gunther B, Kumpmann A, Kunze D. H, 1992, “Secondary recrystallization effects in nanostructured elemental metals”. Scripta Metallurgica et materialia, Vol. 27, pp 833-838.

[2.33] Hahn H. and Averback R. S.; The production of nanocrystalline powders by magnetron sputtering. J. Appl. Phys. Vol. 67 (2), pp. 1113-115.

[2.34] Yamaguchi K., Matsumoto K, Fujii., 1990, J. appl. Phys., Vol. 67, pp. 4493.

[2.35] Lawaezeck R., Menzel M., Pietsch, H., 2004, Appl. Organomatic chem., Vol. 18, pp. 506.

[2.36] McMichael R. D., Bennett L. H., Walson R. F., 1992, J. Magn. Mater. Vol. 111, pp. 29.

[2.37] Kang Y. S., Risbuds, Rabolt J. F., Stroeve P., 1996, Chem. Mater. Vol. 8(9), pp. 2209.

[2.38] Raj K., MosKovitz B., Casciari R., 1995, J. Magn. Matter, Vol. 149, pp. 174.

[2.39] Robinson D. B, Persson H. H. J, Zing H., Li G., Pourmand N., Sun., Wang S. X., 2005, Langmuir, Vol. 21, pp. 3096.

[2.40] Grancharou S. G., Zeng H., Sun S., Wang S. X., O’Brien S., Murray C. B., Kirtley J. R. 2005, J. Phys. Chem., Vol. B109, pp. 13030.

[2.41] Gee S. H., Hong Y. K., Erickson D. W., Park M. H., Suo J. C., 2003, J. Appl. Phys., Vol. 93(10), pp. 7560.

[2.42] Grasset F., Labhsetwar N., Li D., Park D. C., Saito, N., Haneda H., Cador, O., Roisnel, T., Mornet, S., Duguet, E., Portier, J., Etourneau; J. Langmuir, 1990, Vol. 18(21), pp. 8209.

[2.43] Ryu B.-H., Chang H. J., Choi Y. M., Kong K. J., Lee J. O., Kim C. G., Jung H. K., Byun J. H. 2004, Phys. Stat. Sol. Vol. 201(8), pp. 1855.

[2.44] Hsu W.-C., Chen S. C., Kuo P. C., Lie C. T., Tsai W. S. 2004, Mat. Sci. Eng. B, Vol. 111, pp. 142.

[2.45] Bruce I. J., Taylor J., Todd M., Davies M. J., Borioni E., Sangregorio C., Sen T. 2004. J. Magn. Magn. Mater. Vol. 284, pp.145.

[2.46] Bumb A., Brechbiel M W., Choyke P L., Fugger L., Eggeman A., Prabhakaran D., Hutchinson J. and Dobson P J., 2008, "Synthesis and characterization of ultra-small superparamagnetic iron oxide nanoparticles thinly coated with silica". Nanotechnology, Vol. 19, pp.335601- 6.

[2.47] Wang L., Liu J., Li X., Shi J., Hu J., Cui R., Zhang Z., Pang D., and Chen Y., 2011, "Growth propagation of yeast in linear arrays of microfluidic chambers over many generations". Biomicrofluidics, Vol. 5, pp. 044118-9.

[2.48] Bhargava, R.N., Gallagher, D., Hong, X. and Nurmikko, A. 1994,"Optical properties of manganese-doped nanocrystals of ZnS" Physical Review Letters, vol.72, pp.416-419.

[2.49] Morita, M., Rau, D., Kajiyama, S., Sakurai, T., Baba, M. and Iwamura, M. 2004, "Luminescence properties of nano-phosphors: metal-ion doped sol-gel silica glasses". Materials Science-Poland, Vol.22 (1), pp5- 15.

[2.50] Hangxun Xu, Brad W. Zeiger and Kenneth S. Suslick, 2013, "Sonochemical synthesis of nanomaterials". Chem. Soc. Rev.,Vol. 42, pp. 2555—2567.

[2.51] H. X. Xu and Suslick K. S., 2010, ACS Nano, Vol. 4, pp. 3209.

[2.52] Gohil, S., Chandra, R., Chalke, B., Bose, S. & Ayyub, P. 2007, "Sputter deposition of self-organised nanoclusters through porous anodic alumina templates". J. Nanoscience Nanotech. Vol. 7, pp. 1792-1805.

[2.53] Konrad, A., Herr, U., Tidecks, R. And Samwer, F. 2001, "Luminescence of bulk and nanocrystalline cubic yttria", J. of Appl. Phys., Vol. 90(7) , pp.3516-3523.

[2.54] Sue K., Suzuki M., Arai K., Ohashi T., Ura H., Matsui K., Hakuta Y., Hayashi H., Watanabe M., Hiaki T, 2006, Green Chem. Vol.8, pp.634.

[2.55] Adschiri T., Hakuta Y., Arai K., 2000, Ind. Eng. Chem. Res. Vol. 39, pp. 4901.

[2.56] Riman R. E., Suchanek W. L., Lencka M. M., 2002, Ann. Chim. Paris, France, Vol. 27, pp. 15.

[2.57] Lencka M. M., Riman R. E. Riman, 1993, J. Am. Ceram. Soc. Vol. 76, pp. 2649.

[2.58] Shock E. L., Oelkers E. H., Johnson J. W., Sverjensky D. A., Helgeson H. C. 1992, "Calculation of the thermodynamic properties of aqueous species at high pressures and temperatures. Effective electrostatic radii, dissociation constants and standard partial molal properties to 1000 °C and 5 kbar". J. Chem. Soc. Faraday Trans. Vol.88, pp.803.

[2.59] Helgeson H. C., Kirkham D. H. 1974, Am. J. Sci. Vol. 274, pp.1089.

[2.60] Helgeson H. C., Kirkham D. H., Flowers G.C. 1981, Am. J. Sci. Vol. 281, pp. 1249.

[2.61] Sun, S., et al. 2004, Monodisperse MFe_2O_4 (M= Fe, Co, Mn) nanoparticles. Journal of the American Chemical Society, Vol. 126(1): pp. 273-279.

[2.62] Zhu H. P., Zhou Z.Y., Yang R.Y., A. B. Yu, 2007, "Discrete particle simulation of particulate systems: Theoretical developments. Chemical Engineering Science". Vol. 62 pp.3378 – 3396.

[2.63] Der-Ing Liao, James E. Thompson, Stephen F., Barbara V., and Douglas B. Jordan, 2001, "A Structural Account of Substrate and Inhibitor Specificity Differences between Two Naphthol Reductases". Biochemistry, Vol. 40, pp. 8696-8704.

[2.64] Zhu, Y., Hinds, W. C., Kim, S., Shen, S., and Sioutas, C. 2002, "Study of ultrafine particles near a major highway with heavy-duty diesel traffic". Atmospheric environment, Vol. 36(27), pp. 4323-4335.

[2.65] Milchev A, 2002, "Electrocrystallization Fundamentals of Nucleation and Growth Boston". Kluwer Academic Publishers.

[2.66] Gu, G. H., and Suh, J. S. 2010, "Silver nanorods used to promote SERS as a quantitative analytical tool". Journal of Raman Spectroscopy, Vol.41 (6), pp.624-627.

[2.67] Na, H. B., Song, I. C., and Hyeon, T. 2009, "Inorganic nanoparticles for MRI contrast agents". Advanced materials, Vol. 21(21), pp.2133-2148.

[2.68] Li, X., Wang, X., Zhang, L., Lee, S., and Dai, H. 2008, "Chemically derived, ultrasmooth graphene nanoribbon semiconductors". Science, Vol.319 (5867), pp.1229-1232.

[2.69] Ahmad A. M., P. Senapati, S. Mandal D. Khan M. I. Kumar, R. & Sastry, M., 2003, "Extracellular biosynthesis of silver nanoparticles using the fungus Fusarium oxysporum". Colloids and Surfaces B: Biointerfaces, Vol. 28: pp. 313-318.

[2.70] Ankamwar, B.D., C.; Ahmad, A. and Sastry, M., 2005, "Biosynthesis of gold and silver nanoparticles using Emblica officinalis fruit extract, their phase transfer and transmetallation in an organic solution". J Nanos Nanotechnol, Vol. 5: pp. 1665-1671.

[2.71] Korbekandi, H.I., S. and Abbasi, S., 2009, "Production of nanoparticles using organisms". Critical Reviews in Biotechnology, Vol. 29: pp. 279-306.

[2.72] Iravani, S., 2011, "Green synthesis of metal nanoparticles using plants". Green Chem, Vol. 13: pp. 2638-2650.

CHAPTER III

[3.1] Wan N. W. S., Teong L. C., Hanafiah M. A. K. M., 2011, " Absorption of dyes and heavy metal ions by chitosan composite: A review". Carbohydrate polym., Vol. 83, pp. 1446-1456.

[3.2] Rani K. M. N. V, 2000, "A review of chitin and chitosan applications". Reaet. Func. Polym., Vol. 46, pp. 1-27.

[3.3] Ghaeel A. Shariaty M., Barzin J., Ismail A. F., 2013, "Chitosan/Polyethersulfone composite nanofiltration membrane for industrial wastewater treatment". International J. Nanosci. Nanotechnology, pp. 213-220.

[3.4] Gupta, A. K., and Gupta, M. 2005, "Synthesis and surface engineering of iron oxide nanoparticles for biomedical applications". Biomaterials, Vol.26 (18), pp.3995-4021.

[3.5] Binnig G., Rohrer H., Gerber Ch., Weibel E. 1982, Phy. Rev. Lett. Vol. 49, pp.57.

[3.6] Hansma P. K., Tersoff J, 1987, J. Appl. Phys. Vol. 61, pp. R1.

[3.7] Magonov S. N., Whangbo M. H, 1996, "Surface Analysis with STM and AFM-Experimental and Theoretical Aspects of Image Analysis". VCH.

[3.8] Cullity B. D. 1959, "Elements of X-ray Diffraction". Addison-Wesley, Inc. USA.

[3.9] Vankar V. D., Das S. R., Nath P., Chopra K. L. 1978, Phys. Slat. Sol. Vol.45, pp. 665.

[3.10] Binnig G., Rohrer H., Gerber Ch., Weibel E. 1982, Phy. Rev. Lett. Vol. 49, pp.57.

[3.11] Binnig G., Quate C., Gerber Ch. 1986, Phy. Rev. Left. Vol.56, pp. 930.

[3.12] Nelson J. B., Riley D. P., 1945, “An experimental investigation of extrapolation methods in the derivation of accurate unit-cell dimension of crystals”. Proc. Phys. SoC, London, Vol. 57, pp. 160.

[3.13] Foner S. 1959, “Versatile and Sensitive Vibrating Sample Magnetometer”. Rev. Sci. Instrum, Vol.30, pp. 548.

[3.14] Smith D.O, 1956, “Development of Vibrating Coil Magnetometer”. Rev.Sci.Instrum. Vol. 27, pp. 261.

[3.15] Leupold O., Pollmann J., Gerdau E., Ruter H. D., Faigel G., Tegze M., Bortel G., R uffer R., Chumakov A. I. and A. Baron Q. R. 1996, Europhys. Lett., Vol.35, pp.671.

[3.16] Konjhodzic A., Adamczyk A, Vagizov F., Hasan Z., E. E. Alp, Sturhahn W., Jiyong Z and Carroll J. J. 2006, Hyperfine Int., Vol.170, pp.83.

[3.117] Gutlich P., Link R., Trautwein A., 1978, “Mossbauer Spectroscopy and Transition” Metal Chemistry, Springer, Heidelberg.

[3.18] Gutlich P. and Ensling J. 1999, “Inorganic Electronic Structure and Spectroscopy”. Edited by E. I. Solomon and A. B. P. Lever, Wiley, New York, 161.

[3.19] Gonser U. 1975, “Topics in applied physics, Mossbauer Spectroscopy”. Springer-Verlag New York, LLC, Vol. 5.

[3.20] Gunther K. Werthein; 1964, “Mössbauer Effect: Principle and Application”. Academic Press, New York.

[3.21] U. Goner, Ed. 1973, “Topics in Applied Physics”. Springerverlag, Berlin Heidelberg, New York.

[3.22] Gutlich P., Link R., Trautwein A. 1978, “Mossbauer Spectroscopy and Transition Metal Chemistry”. Springer, Heidelberg.

[3.23] Shenoy, G. K. and Wagner, F. E., Mossbauer Isomer Shifts, North Holland, Amsterdam, 1978.

[3.24] Shirley D. A. 1964, Rev. Mod. Phys., Vol.36, pp.339.

[3.25] Wertheim G. K. 1964, “Mossbauer Effect: Principles and Applications”. Academic Press, New York.

[3.26] Walker L. R., Wertheim G. K., Jaccarino V. 1961, Phys. Rev. Lett. Vol.6, pp. 98.

[3.27] Willium D. Callister, 2003, "The university of Utha: Materials science and Engineering 6th Ed. Wiley.

[3.28] Gunter K., Werthein, 1964, "Mossbauer effect: principle and application". Academic Pres, New York.

[3.29] Stemnheimer R. M., 1951, Phys Rev. Vol. 84, pp. 244.

[3.30] Werthim., 1964, "Mossbauer effect: principle and application". Academic press, New York.

[3.31] Anjali Krishna M., 1980, "Mossbauer study of electronic field gradients in natural mica and synthesis spinel system". Ph. D Thesis, University of Rajsthan, Jaipur.

[3.32] Fermi E., 1930, Z-physics, Vol. 60, pp. 320.

[3.33] Ferrel R. A, 1960, Aj, Vol. 28, pp. 484.

[3.34] Finsy, R. 1994, "Particle sizing by quasi-elastic light scattering". Adv. Colloid Interface Sci. Vol. 52, pp. 79–143.

[3.35] Müller, R. H.; Schuhmann, R.; Thode, K. 1996 "Teilchengrößenmessung in der Laborpraxis (Particle size analysis in laboratory practice)". Wissenschaftliche Verlagsgesellschaft mbH, Stuttgart.

[3.36] Berne B. J. and Pecora R. 1990, "Dynamic Light Scattering". Robert E. Krieger Publishing Company, Malabar, Florida.

[3.37] Routh A. F. and Zimmerman W. 2003, "The Diffusion Coefficient of a Swollen Microgel Particle". J. Colloid and Interface Sci., Vol.261, pp.547-5517.

[3.38] The ALV Manual of the version for ALV-5000/E for Windows, 1998, ALV-Gmbh, Germany.

[3.39] Brazel C. S., Pharmaceut Res. 2009, Vol.26, pp. 644.

[3.40] https://www.britannica.com/science/hysteresis#ref2692

[3.41] Hergt R., Dutz S. 2007, J. Magn. Magn. Mater. Vol. 311, pp.187.

CHAPTER IV

[4.1] Sattar A., El-sayed M., Agami R., Ghani A. 2007, "Magnetic properties and electrical resistivity of Zn^{4+} substituted Li-Zn ferriet", Vol.4 (2), pp. 89-93.

[4.2] Iqbal J., Rajpoot M., Jan T., Ahmad I. 2014, "Annealing induced enhancement in magnetic properties of $Co_{0.5}Zn_{0.5}Fe_2O_4$ nanoparticles". J Supercond Nov. Magn, DOI: 10.1007/s 10948-014-2505-4.

[4.3] Zhang M., Zi Z., Liu Q., zhang P., Tang X., Yang J., Zhu X., Sun Y., Dia J. 2013, "Size effect on magnetic properties of $Ni_{0.5}Zn_{0.5}Fe_2O_4$ prepared by sol-gel method". Advances in materials science and engineering, Vol. 10, pp.609819.

[4.4] Arief S., Rahmayeni, Zulhadjri, 2017, "Comparison of sol-gel and hydrothermal synthesis of Zinc ferrite nanoparticles". RJPBCS, Vol.8 (1), pp. 499-503.

[4.5] Koseoglu Y., Baykal A., Gozuak F., Kavas H. 2009, "Structural properties of $Co_xZn_{1-x}Fe_2O_4$ nanocrystals synthesized by microwave method". Polyhedron, Vol. 28, PP. 2887-2892.

[4.6] Pankhurst Q A, Connolly J., Jones S K., Dobson J. 2003, "Applications of magnetic nanoparticles in biomedicine". J. Phys. D: Appl. Phys., Vol. 36, pp. 167-181.

[4.7] Pei W., Kumada H., Natusme T., Saito H., Ishio S. 2007, "Study of magnetic nanoparticles synthesized by chemical method". Journal of Magnetism and Magnetic Materials, Vol. 310, pp. 2375-2377.

[4.8] Lopez J., Bahamon L. F., Prabo J., Caicedo C. J., Zambrano G., Gomez E. M., Esteve J. Prieto P. 2012, "Study of magnetic and structural properties of ferrofluids based on cobalt-zinc ferrite nanoparticles". Journal of Magnetism and Magnetic Materials, Vol. 320, pp. 394-402.

[4.9] Kumar V., Rana A., Yadav M.S. Pant R. P. 2008, "Size-induced effect on nano-crystalline $CoFe_2O_4$," Journal of Magnetism and Magnetic Materials, Vol. 320, pp. 1729-1734.

[4.10] Morup S., 1994, "Superparamagnetism and spin glan ordering in magnetic nanoparticles". Europhys. Tett., Vol. 28, pp. 671-676.

[4.11] Min Z., Zhenta Z., Qiangchun L., Peng Z., Yuping S. Tianming D.,2013, "Size effects on magnet i.e properties of $Ni_{0.5}Zn_{0.5}Fe_2O_4$ prepared by sol-gel method". Adv. Mater Sci. Eng. Doi: 10.1155/2013/609819.

[4.12] Zeinali S., Nasirimoghddam S., Sabbaghi S. 2016, "Investigation of the synthesis of chitosan coated iron oxide nanoparticles under different experimental conditions". International Journal of Nanoscience, Vol. 12(3), pp. 183-190.

[4.13] Roychoudhury P., Pal R. 2014, Journal of algal Biomass Uttn, Vol. 5, pp. 15-19.

[4.14] Eltabey M. M., Ali N. A. 2014, "Effect of annealing temperature on structural and magnetic properties of Co-Zn ferrite nanoparticles". Int. J. of Adv. Research, Vol. 2(6), pp. 184-192.

[4.15] Mazzarino L. Travelet C., Murillo S., Otsuka I., Paintrand I, Sennae E., Borsali R. 2012, "Elaboration of chitosan coated nanoparticles loaded with curcumin mucoadhesive applications". Journal of colloid and Interface Science, Vol. 370, pp. 58-66.

[4.16] Carpi F., Smela E. 2009, "Biomedical applications of electroactive polymer actuators". Chichester Wiley, P65.

[4.17] Johannsen M., Gneveckow U., Eckelt L, Feussner A., Waldofner N., Scholz R., Deger S., West P., Loening S. A., Jordan A. 2005, "Clinical hyperthermia of prostate cancer using magnetic nanoparticles: Presentation of a new interstitial technique". International Journal of Hyperthermia, Vol. 21(7), pp. 637-647.

[4.18] Hoque S. M., Tariq M., Liba S., Salehin F., Mahmood Z. H., Khan M. N. I., Chattopadhayay K., Islam R., Akter S. 2016, "Thermo-therapeutic application of chitosan and PEG coated $NiFe_2O_4$ nanoparticles". Nanotechnology, Vol. 27, pp. 285702-10.

[4.19] Wang L., An Y., Yuan C., Zhang H., Liang C., Ding F., Gao Q., Zhang D. 2015, "GEM-loaded magnetic albumin nanospheres modified with cetaximab for simultaneous targeting, magnetic resonance imaging, and double-targeted thermochemotherapy of pancreatic cancer cells". International Journal of Nanomedicine, Vol. 10, pp. 2507-2519.

[4.20] Andra W., Nowak H.; Magnetism in Medicine, Wiley-VCH Verlag GmbH & Co. KGaA, 2nd edition, chap.4

[4.21] Abenojar E., Wickramasinghe S., Concepcion J., Samia S. 2016, "Structural effects on the magnetic hyperthermia properties of iron oxide nanoparticles". Progress in Natural Science: Materials International, 26, 440-448.

[4.22] Heegt R., Duts S., Muller R., Zeisberger M. 2006, "Magnetic particle hyperthermia: nanoparticle magnetism and materials development for cancer therapy". Journal of Physics: Condens. Matter, Vol.18, pp. 2919-2934.

[4.23] Yamamoto Y., Horiuchi K., Takeuehi M., Tanaka N., Aihara R., Takeuch N., Fujlta S. 2014, "Size dependence study on magnetic heating properties of superparamegnetic iron oxide nanoparticles suspension”. Journal of Applied Physics, Vol. 116, pp. 123906.1-7.